UNIVERSITY OF OKLAHOMA

GRADUATE COLLEGE

OPTIMIZATION OF A HIGH-ENERGY X-RAY INLINE PHASE SENSITIVE IMAGING SYSTEM FOR DIAGNOSIS OF BREAST CANCER

A DISSERTATION

SUBMITTED TO THE GRADUATE FACULTY

in partial fulfillment of the requirements for the

Degree of

DOCTOR OF PHILOSOPHY

By

MUHAMMAD USMAN GHANI
Norman, Oklahoma
2018

OPTIMIZATION OF A HIGH-ENERGY X-RAY INLINE PHASE SENSITIVE IMAGING SYSTEM FOR DIAGNOSIS OF BREAST CANCER

A DISSERTATION APPROVED FOR THE
SCHOOL OF ELECTRICAL AND COMPUTER ENGINEERING

BY

_____
Dr. Hong Liu, Chair

_____
Dr. Ramadan Ahmed

_____
Dr. Bin Zheng

_____
Dr. Zhisheng Shi

_____
Dr. Joseph Havlicek

I offer my heartfelt love and appreciation to my wife Kayinat and my owl daughter Salsabeel who endured my many absences to focus on completing this degree and dissertation. I look forward to spending much more time with my family. I dedicate this dissertation to my parents. They have cheered my successes, reassured me after my failures, and are an unwavering source of love and support.

Acknowledgements

Dr. Hong Liu, I would like to thank you for your immense support in achieving academic, moral and ethical goals during my academic research journey. Under your guidance, it has been a terrific learning journey to conduct research in the highly innovative and knowledge rich environment of advanced medical imaging lab. As a fatherly figure, you have been an amazing mentor and a selfless supporter of my academic and professional development.

I would like to mention Dr. Xizeng Wu and Dr. Aimin Yan from University of Alabama at Birmingham, Dr. Kai Yang from Massachusetts General Hospital and Dr. Laurie Fajardo from University of Utah for their tremendous collaborations and teamwork. In addition, I would like to thank the current members of our research team; Dr. Yuhua Li, Dr. Molly Wong, Dr. Di Wu, Farid Omoumi and Guo Yuran along with the previous members and visiting scholar, Dr. Liqiang Ren, Dr. Zheng Li and Dr. Zhongxing Zhou for their help and energetic work environment.

Finally, I would like to express my gratitude to the members of my committee; Dr. Ramadan Ahmed, Dr. Joseph Havlicek, Dr. Zhisheng Shi and Dr. Bin Zheng for their unbelievable help and encouragement throughout my research and academics. I would like to especially thank Drs. Havlicek and Shi for their continued support and guidance through this degree, as well as my master's degree.

Table of Contents

List of Tables

List of Figures

Abstract

Breast cancer screening modalities have received constant research attention that are mainly focused on their abilities to detect cancer at an early stage while reducing the risks of harmful radiation dose delivered to the patient. As a result, numerous advancements have been made over the last two decades which include the introduction of digital mammography (DM) and digital breast tomosynthesis (DBT). Numerous clinical trials have demonstrated the decrease in mortality rates by employing these modalities. Significant research attention remains focused on investigating methods for further improving the detection capabilities and reducing the radiation dose. The conventional x-ray imaging technique relies on the attenuation characteristics of a tissue to produce imaging contrast. However, the similar attenuation characteristics of normal and malignant breast tissue present a challenge in differentiating between them using conventional x-ray imaging. The current technique for providing higher image quality involves the introduction of anti-scatter grids and operating the x-ray tubes at much lower x-ray energies as compared to the other radiography fields, both of which results in an increased radiation dose. The current method for providing higher image quality involves utilizing anti-scatter grids and operating at much lower x-ray energies than other radiography fields, both of which result in an increased radiation dose. Phase sensitive imaging is an emerging technique, which relies not only on attenuation coefficients but also the effects produced by x-ray phase shift coefficients. Within the diagnostic energy range, it has been estimated that the phase shift coefficients of a breast tissue are at least 2-3 orders of magnitude larger than their attenuation coefficients. Thus, this technique

holds the potential to increase the x-ray energy and remove the grid without compromising the image quality, which could potentially reduce the patient dose. The inline phase sensitive approach involves the simplest implementation—provided that the imaging system is spatially coherent — as it does not involve the introduction of any optical element between the object and detector. Preclinical studies with the inline phase sensitive imaging technique at the same energy as conventional imaging have indicated the ability to reduce the radiation dose without negatively impacting the diagnostic capabilities. However, there are some existing challenges that have prevented this technique in its clinical implementation. Responding to the challenges, an inline phase sensitive imaging prototype has been developed in the advanced biomedical imaging laboratory. The goal of the research presented in this dissertation comprises a thorough investigation in optimizing a high energy phase sensitive imaging prototype efficiently in terms of its geometric and operating parameters. Once optimized, the imaging performance of this phase sensitive x-ray imaging prototype is going to be compared with the commercial digital mammography and digital breast tomosynthesis (DBT) imaging systems using modular breast phantoms at similar and reduced mean glandular dose (D_g) dose levels.

This dissertation includes numerous original contributions, perhaps the most significant of which were the demonstration of the ability of inline phase sensitive imaging prototype to deliver higher image quality required for tumor detection and diagnosis at higher x-ray energies in comparison with low energy commercial imaging systems at similar or less radiation dose levels. These results clearly demonstrate the ability of the high energy

inline phase sensitive imaging system to maintain the image quality improvement that is necessary for diagnosis at high x-ray energies without an increase in the radiation dose.

Chapter 1. Introduction

1.1 Significance

Cancer is second leading cause of death in the U.S after the heart disease [1,2]. The number of cancer deaths have been climbing for decades, bringing the nation's top two killers closer than ever in the rankings for leading cause of death. For 2017, the American cancer society estimates about 252,710 new cases of invasive breast cancer are expected to be diagnosed in women with an estimate of 40,610 breast cancer deaths [3]. Breast cancer is a progressive disease and small tumors in general indicate an early stage, early detection of breast cancer is very important to drastically improved chances for survival. According to the American Cancer Society, women with stage 0 or stage I breast cancer have an almost 100% 5-year survival rate. If detected while still in stage II, the survival rate remains high at 93% [4-7]. However, when the cancer reaches stage III, 5-year survival drastically decreases to 72% and once it the cancer has metastasized or reached stage IV or above women only have about a 22% chance of surviving their diagnosis. Thus, early detection is key to improving breast cancer survival rates.

Mammography has been the most widely used diagnostic technique for breast cancer detection and clinical trials have proven its ability to decrease mortality rates [8-13]. Due to its potential for saving lives, mammography has received constant research focus since the development of dedicated mammography systems [14-15]. Early detection has been a constant goal throughout the development of mammography. In mammography, two-dimensional (2D) images of three dimensional (3-D) objects are acquired which does not able to combat the challenges presented by overlapping structures from dense tissue

superimposition. This inability potentially leads to missed cancers, as well as false-positive recalls and/or biopsies. Digital breast tomosynthesis (DBT) is an emerging quasi-three-dimensional (3D) x-ray imaging modality with demonstrated value in breast cancer screening [16-21]. In DBT, a set of low dose projection views are acquired over a limited angular range. A set of tomographic slices is reconstructed from the limited angle projection views to provide better visibility and discrimination of breast masses by reducing the structured noise caused by the overlapping breast tissues. Both diagnostic mammography and DBT solely rely on the attenuation contrast for the image formation. Attenuation contrast is based on the principle that x-rays are absorbed in varying amounts according to the biological composition of structures within an object, which generate differences in contrast on the x-ray image [22-24]. For example, the difference in biological composition between bones and soft tissue produces very high attenuation contrast between them on an x-ray image. However, due to the extremely similar composition of normal and malignant breast tissue, the results are in low attenuation contrast which presents a significant challenge for cancer detection in the field of mammography and DBT [24]. As a result, there is always a need for much higher image quality in breast imaging to highlight the differences between normal and malignant tissue. To fulfill that requirement in the attenuation-based imaging, improving the image quality can be accomplished by lowering the x-ray beam energy so that to increase the amount of attenuation experienced by a tissue and to improve the signal to noise ratio [22]. Other way to improve the signal to noise ratio is to employ an anti-scatter grid which reduces the contribution of the scattered x-rays to the image. Both techniques have

significance on the radiation dose delivered to the patient which in turn is potentially harmful.

In the last two decades, a new x-ray imaging technology has emerged called phase sensitive x-ray imaging which has the potential to improve this difficult balance between image quality and radiation dose. Phase sensitive imaging is based on the principle of x-rays being part of the electromagnetic waves spectrum, undergoes phase shits as it transverses the objects [25-30]. The phase shift coefficients are also dependent on biological properties of the structures within an object. Phase induced contrast is generated from the interference among parts of the emerging wave fronts that have experienced different phase shifts. Contrast in the image is produced according to differences in phase shift coefficients between structures [28,30]. It has been reported that for breast elements such as soft tissue, phase shift coefficients are at least 2-3 orders of magnitude larger than their attenuation coefficients for the diagnostic energy range [27,31,32]. Therefore, the variations in soft tissue density give rise to much stronger phase shift induced contrast compared to the attenuation-based contrast. If proper operating conditions are utilized, this phase shift induced contrast is superimposed onto the attenuation contrast on the image and helps to improve the visibility of the borders of structures and other fine details. Therefore, phase sensitive imaging has received extensive research focus, and numerous studies have indicated the potential of the new technology to benefit the fields of radiography, especially breast imaging applications. The in-line phase sensitive approach involves the simplest implementation of all the other approaches — provided that the imaging system is spatially coherent—as it does not involve the introduction of any optical element between the object and detector [33-36].

This approach utilizes a similar system configuration as of traditional radiography with typically a micro focus source generating a partially coherent x-ray beam which traverses an object, and an object-to-detector distance is introduced for the development of interference patterns to be detected on the imaging plane. The improvement in image quality with this approach has been consistently reported [37-46]. The ability to maintain the image quality improvement with reduced radiation dose has been thoroughly investigated [47-60], which is of critical importance in breast imaging.

The typical x-ray energies for diagnostic radiography range from 15 to 150 kilovolts (kV). Due to the restrictions imposed by attenuation-based imaging as detailed above, mammography and DBT currently operates at the lower end of the range. However, the distance that is introduced between the object and the detector in this approach results in fewer x-ray photons to be detected by the detector, as compared to the traditional contact mode detection under the same conditions of exposure parameters, radiation dose delivery and the capability of detectors. Thus, an in-line phase sensitive imaging system can hardly provide similar imaging ability as mammography and DBT systems, due to the massive loss of attenuation-based contrast. The topic of higher x-ray energies for reduced dose has been thoroughly investigated by other radiography fields, such as chest radiography, which generally operates between 120 and 150 kV. To solve this problem, high-energy x-rays, which are already employed in chest radiography, can be employed to compensate for that loss of x-ray photons during a long-distance propagation, thus preserving most of the attenuation contrast.

For a breast tissue, the phase shift coefficients decrease much slowly than attenuation coefficients as the x-ray energy increases, the use of inline phase sensitive imaging can sustain the image quality improvements at higher x-ray energies as compared to the attenuation-based imaging. Due to the high penetrability and low absorption of high-energy x-ray photons at higher energies, the radiation dose received by patients can also be potentially reduced. To the best of my knowledge, the potential of utilizing x-ray energy ranges such as those in chest radiography for mammography and DBT has not been reported by other research groups.

In the past five years, the dedicated members at our lab developed a high energy inline phase sensitive imaging prototype. The focus of the research presented in this dissertation comprises a thorough investigation of characterizing and optimizing the high energy inline phase sensitive prototype in terms of its operating parameters for both mammography and DBT applications. Once optimized, phantom studies are going to be conducted in mammography and DBT imaging modes and their imaging performances will be compared with the two-commercial attenuation-based systems at similar or less radiation dose levels. The two-commercial attenuation-based systems are routinely used in the clinical world in the U.S for breast cancer screening. Thus, this investigation holds a great potential of applying higher x-ray energies using inline phase sensitive imaging technique to the field of mammography and DBT for breast cancer screening. In addition to the dose benefits of increasing the x-ray energy, the dissertation research also has the potential to overcome an existing challenge in the inline phase sensitive imaging involving the number of output quanta generated with the x-ray source, which will be discussed in more detail in the following chapters.

1.2 Organization of Dissertation

The organization of this dissertation is as follows. Chapter 2 details the research background, including the principles and theory of the x-ray in-line phase sensitive imaging and phase retrieval techniques. Chapter 3 presents the development and optimization of a high-energy x-ray in-line phase sensitive prototype utilized in this dissertation. Chapter 4 provides a very detailed characterization of a hybrid micro focus x-ray tube which is a core component of the prototype. Chapter 5 presents a detailed comparison of the high energy inline phase sensitive prototype and commercial clinical mammography systems in imaging phantoms with varying glandular ratios. Chapter 6 further details the comparison of the prototype and a commercial mammography system in imaging a dense breast phantom with heterogenous backgrounds. Chapter 7 explains the feasibility of employing a digital tomosynthesis system in overcoming the challenges associated with digital mammography. Chapter 8 details a comparison of phase sensitive digital tomosynthesis prototype and a commercial digital breast tomosynthesis system in imaging heterogenous phantoms with simulated tumors. microbubbles as an x-ray phase contrast agent with a projection mode imaging system and provides a criterion in microbubble shell material selection. Finally, a research summary and a discussion of future research direction are presented in Chapter 8.

Chapter 2. Review of the Current Research

2.1 Background

Diagnostic x-rays are an electromagnetic (EM) radiation having the wavelength shorter than the ultraviolet rays with photon energies in the range from about 10 keV to 150 keV. Three parameters are commonly used to characterize the EM; frequency (ν), wavelength (λ) and energy and they all are related to each other by Eq. (2.1) [22]

$$E = h\,\nu = \frac{hc}{\lambda} \tag{2.1}$$

where h = 6.626 × 10^{-34} J.s = 4.136 × 10^{-18} keV.s is the Plank's constant. When E is expressed in kilo-electron-volts and λ in nanometers (nm), we have

$$E\,(keV) = \frac{1.24}{\lambda\,(nm)} \tag{2.2}$$

Diagnostic x-rays occupy a distinguishable range in wavelength from 0.1 to 0.008 nm, making them suitable to investigate small objects and various structures in different media. When x-rays interact with the electrons of a sample, there is electronic excitations which give rise to various forms of x-ray scattering. These scattered x-rays carry information about electronic states and structures encountered during their travel to the detector. Considering an x-ray wave of amplitude, $A_0(\mathbf{r}) = E_0(\mathbf{r}) \exp(-i2\pi ft)$, that interact with a sample with thickness *l* and refractive index *n*. The refractive index of a medium is defined as follows: [27-29]

$$n = 1 - \delta + i\beta \tag{2.3}$$

The incident wave makes the electron of the sample oscillate in the direction of the electric field, and as an accelerated charge the electron radiates with frequency *f* of the incident wave. The resulting wave after the transmission through the medium can be written as [32, 33]

$$A_1(\mathbf{r}) = E_0(\mathbf{r}) \exp(-i2\pi fnt) \tag{2.4}$$

$$A_1(\mathbf{r}) = E_0(\mathbf{r}) \exp\left(-i2\pi \frac{c}{\lambda}(1-\delta+i\beta)\frac{l}{c}\right) \tag{2.5}$$

$$A_1(\mathbf{r}) = A_0(\mathbf{r}) \exp\left(\frac{2\pi i\delta l}{\lambda}\right) \exp\left(\frac{-2\pi i\beta l}{\lambda}\right) \tag{2.6}$$

In Eq. (2.6), the first exponential term accounts for the phase change, and the second for the decrease in the amplitude. The linear attenuation coefficient (μ) and phase shift coefficient (φ) for a given tissue are given as

$$\mu = \frac{4\pi\beta}{\lambda} = \frac{2\omega\beta}{c} = 2N\lambda r_e f_l^I \tag{2.7}$$

$$\varphi = \frac{2\pi\delta}{\lambda} = \delta K = N\lambda r_e f_l^r \tag{2.8}$$

where r_e is the classic electron radius, N is the number of electrons per unit volume (density), f_l^i – the imaginary part of the anomalous scattering factor and f_l^r is the real part of the anomalous scattering factor [33].

It has been noted that the real and imaginary parts of the refractive index (*n*) changes differently with respect to the energy (*E*) of the incident x-ray photon [31,34,61]. For light element in human body such as hydrogen, carbon, nitrogen and oxygen, φ is proportional

to 1/E, while μ is approximately proportional to $1/E^3$. This means that that for light elements, the attenuation coefficients decrease at a much faster rate than the phase shift coefficients. Furthermore, for those light elements within the diagnostic energy range, φ is two-three orders of magnitude larger than μ. Therefore, with the variations in soft tissue density, a much stronger phase-shift induced contrast will be produced in comparison to the attenuation contrast [25,28,29]. This creates an opportunity of utilizing higher energy x-rays for potential phase contrast soft tissue imaging which may potentially reduce the radiation dose delivered to the patient.

Four major techniques have been developed to exploit the phase-contrast in the x-ray regime which are: (a) in-line based imaging [25], (b) analyzer-based imaging (*ABI*) [62], (c) crystal interferometry methods based on the use of crystals [63-64] and (d) grating interferometric methods [65]. All of the PCI techniques are different in their experimental set-up and requirements in terms of the x-ray beam spatial coherence. The final image contrast in each technique depends on several factors, including the spatial resolution of the x-ray detector, the specific image formation mechanism, x-ray energy and the beam divergence.

2.2 In-line Phase Contrast X-ray Imaging

With in-line phase-contrast imaging method, a partially coherent wave-front traverses the sample and the variations in thicknesses (*l*) and refractive index (*n*) of a sample causes the wave front to distort in terms of both amplitude and phase. When the detector is directly placed behind the sample, an attenuation-based image is formed while as the distorted wave-front propagates sufficiently far, the small differences in phase shifts of

the wave front causes interference patterns and variations of intensity are observed in the image plane. These interference patterns cause edge enhancements at interfaces between components with varying phase shift coefficients. This edge enhancement has its own significance, for instance, with malignant breast tumors, the edges are heterogenous in comparison to a benign tumor and a phase contrast image could potentially identify the intra tissue heterogeneity for accurate diagnostic evaluation. Under generalized conditions, the lateral Laplacian of phase is directly proportional to the longitudinal gradient of intensity. Therefore, the contrast that is arising from the lateral Laplacian of phase emphasizes the internal and external contours where the phase shift coefficients are changing.

The schematics of the setup for the inline phase contrast imaging is shown in Figure 2.1. In this figure, R_1 denotes the source-sample distance, R_2 is the sample to detector distance. To visualize the phase contrast effects, the x-ray beam generated from an x-ray source with focal spot size (s) needs to have sufficient spatial coherence lengths which is defined as [28]

$$L_{coh} = \frac{\lambda R_1}{s} \tag{2.9}$$

It can be noticed that by operating at lower photon energy (E) i-e higher wavelengths over a longer R_1 distance utilizing x-ray tubes with finite focal spot size (s) can give the best phase contrast image. Furthermore, the R_2 distance also plays an important in the phase contrast imaging formation. It has been proposed that in addition to the sufficient L_{coh}, phase-space shearing length (L_{shear}) also plays a crucial role in phase contrast visibility, which is defined as [34]

$$L_{shear} = \frac{\lambda R_2 u}{M} \tag{2.10}$$

where *u* is the spatial frequency of the structural component of the sample and M is the geometric magnification. According to Wu and Liu analyses [34], if the ratio of L_{shear}/L_{coh} >>1, the wave front is incoherent over the shearing length, and the phase contrast that is associated with the structural component is invisible. If L_{shear}/L_{coh} <<1, the wavefield is fully coherent and the phase contrast associated with the structural component is fully visible. For intermediate cases with L_{shear}/L_{coh} <1, the wavefield is partially coherent and the phase contrast visibility increases with decreasing L_{shear}. An important system parameter, R_2 that is associated with L_{shear}, needs to be optimized.

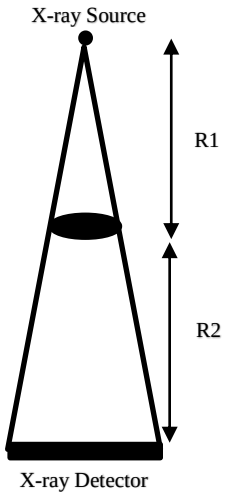

Figure.2.1. The in-line phase contrast imaging implementation system with a micro focus x-ray source and a detector.

2.3 Theory of in-line Phase Contrast X-ray Imaging

To quantitatively analyze the in-line phase contrast imaging modality, it is of critical importance to have a theoretical formalism. We will discuss two models for the formalism of the in-line phase contrast imaging.

2.3.1 Pogany, Gao Wilkins (PGW) Model:

In 1997, Pogany, Gao and Wilkins presented a theory referred as PGW model to establish a theoretical formalism for the in-line phase contrast imaging [25,28]. The PGW model block diagram is given in Figure 2.2.

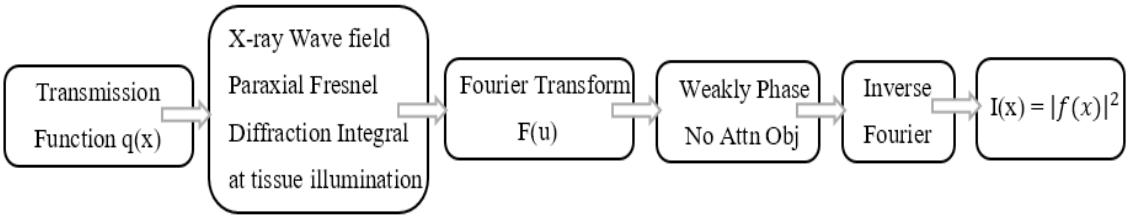

Figure.2.2. Block diagram of PGW model for the quantification of the inline phase contrast imaging.

They modeled the phase shift and attenuation effects of a piece of a tissue as a transmission function *q(x)* which was defined in only x dimension and assumed that both components of *q(x)* are small such that

$$q(x) = exp\,[\, i\,\phi(x) - \mu(x)] \approx 1 + i\,\phi(x) - \mu(x) \qquad (2.11)$$

The x-ray beam illuminates the tissue at z=0 and the x-ray detector is at z. The incident x-ray will be in general refracted and diffracted by the tissue. PGW modeled the diffracted x-ray wave field according to the paraxial Fresnel diffraction theory as

$$f(x; z) = \left\{\frac{i}{\lambda z}\right\}^{1/2} exp(-ikz) \int q(X) * exp\left(\frac{-ik(x-X)^2}{2z}\right) dX \qquad (2.12)$$

where k is the wave number, λ is the x-ray wavelength. The calculation of Fresnel integral is very complicated, and PGW were only able to handle the cases of weakly attenuating and weak phase objects such that its $|\varphi(x)| << 1$ and $\mu(x) << 1$. Under those approximations, it was eventually found that the Fourier transform (FT) of the detected intensity at *z* is

$$I(u, z) = \delta(u) - cos(\pi\lambda z u^2)\, M(u) + \phi(u)\, sin(\pi\lambda z u^2) \qquad (2.13)$$

where $I(u, z)$, $\Phi(u)$ and $M(u)$ are the FT's of image intensity at *z*, the object's projected phase and projected attenuation, respectively. From Eq. (7), PGW found that the phase contrast is proportional to $\nabla^2\varphi$ in low spatial resolution cases. The results of PGW are valid only for phase imaging of weakly attenuating and weak phase objects (very thin tissue samples). These results are going to be totally violated for body parts encountered in clinical imaging applications where a phase change of 2π can be resulted from just few tens micron thickness of breast tissue for x-rays in mammography.

2.3.2 Wu and Liu Model

A new theoretical formalism was presented in 2003 to overcome all the clinical limitation of the PGW model before one tries to analyze and study the phase contrast imaging [66-69]. The so called "Wu-Liu Model" is derived for spherical waves and it recovers the PGW model as its special case. The complete block diagram is given in Figure 2.3.

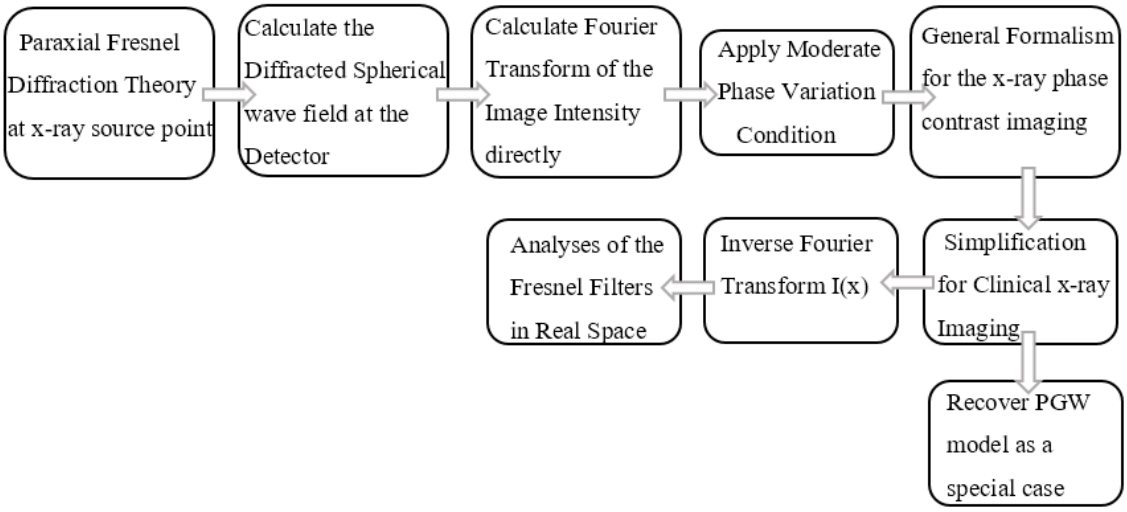

Figure.2.3. Block diagram of Wu & Liu model for the quantification of the inline phase sensitive imaging.

Their strategy was to model the Fresnel diffraction process and relate the object transmission function to image intensity. Considering a monochromatic x-ray point source at a location $(x_0 = 0, y_0 = 0, z_0 = 0)$ with a wavelength of λ, I_0 be the x-ray intensity incident at R_1, they applied the paraxial Fresnel diffraction wave theory to the x-ray point source geometry and calculated the Fresnel–Kirchhoff integral of the diffracted spherical wave field arriving at a location (x, y) on the detector plane as

$$E(x,y) = \frac{\sqrt{R_1 I_0}}{\sqrt{i\lambda} R_2 (R_1+R_2)} exp\left(i\pi \frac{2(R_1+R_2)^2 + y^2}{\lambda(R_1+R_2)}\right)$$

$$\int_{-\infty}^{\infty} exp\left[i\frac{\pi}{\lambda}\left(\frac{\eta^2}{R_1} + \frac{(\eta - X)^2}{R_1}\right)\right] T(\eta)\, d\eta \qquad (2.14)$$

In Equation 2.14, integrating over the variable η convolves T(x) with the Fresnel-diffraction propagator. Instead of calculating the Fourier transform (FT) of the wave amplitude as done in the PGW model, their theory was based on the direct FT of the x-ray diffraction intensity. They derived the x-ray intensity image I(x) at the detector plane, in a symmetric form as

$$I(x,y) = |E(x,y)|^2$$

$$= \frac{I_0}{\lambda M R_2} \iint_{-\infty}^{\infty} exp\left(i\pi M \frac{\left(\eta_1 - {}^{X}/_{M}\right)^2 - \left(\eta_2 - {}^{X}/_{M}\right)^2}{\lambda R_2}\right) T(\eta_1) T^*(\eta_2)\, d\eta_1 d\eta_2 \qquad (2.15)$$

where $I_0 = E_0^2$ is the incident intensity at the object plane, T^* is the complex conjugate of the transmission function. As the integral is difficult to carry out analytically, they attempted to conduct the frequency analysis of I(x) to see how the spatial frequency information of object attenuation and phase are transferred to the detector plane. They substituted Equation 2.15 into the Fourier transform (FT) of the intensity with respect to the object coordinates as

$$\check{I}(u) = \int_{-\infty}^{\infty} exp\left(2\pi i \left({}^{X}/_{M}\, u\right) I(x) d\left({}^{X}/_{M}\right)\right) \qquad (2.16)$$

Image intensity is always known at the detector plane and formulating the image transmission function, imaging geometry and the wave front information from the image intensity make their theoretical formalism more convenient and applicable. Unlike PGW, they assumed that the phase variation across the object is moderate in a small distance $\frac{\lambda R_2 u}{M}$ as $\left|\varphi(x) - \varphi\left(x - \frac{\lambda R_2 u}{M}\right)\right| << 1$. This moderate variation of phase can be easily satisfied in x-ray imaging, especially in the clinical applications where x-ray wavelengths are very short. After tedious calculations and applying the moderate phase conditions and taking into the account of small wavelengths, limited spatial resolution, and finite detector sampling aperture, they found that the FT of the detected image intensity reduces to

$$I(u) = \frac{I_{in}}{M^2}\left\{cos\left(\frac{\pi\lambda R_2 u^2}{M}\right)\ FT(A_0^2) + \ 2\ sin\left(\frac{\pi\lambda R_2 u^2}{M}\right)\ FT(A_0^2\phi)\right\} \qquad (2.17)$$

where

$$FT\,(A_0^2) = \int_{-\infty}^{\infty} A_0^2(\eta) e^{I\ 2\pi\eta u}\ d\eta$$

$$FT\,(A_0^2\phi) = \int_{-\infty}^{\infty} A_0^2\phi(\eta) e^{I\ 2\pi\eta u}\ d\eta$$

Taking the Fourier transform both sides of Eq. (2.17) and using mapping between the differential operators in real-space and polynomials in Fourier space, one obtains the projection intensity arriving at the detector plane I ($\vec{r}_D$) by the x-ray transport equation as

$$I\ (\vec{r}_D) = \frac{I_{in}}{M^2}\left\{cos\left(\frac{\lambda R_2}{4\pi M}\nabla^2\right)\left[A^2(\vec{r}) - \frac{\lambda R_2}{2\pi M}\left(\nabla.\left(\phi(\vec{r})\nabla A^2(\vec{r})\right)\right)\right] - \right.$$
$$\left. 2\ sin\left(\frac{\lambda R_2}{4\pi M}\nabla^2\right)[A^2(\vec{r})\phi(\vec{r})]\right\} \qquad (2.18)$$

where λ is the x-ray wavelength, I_{in} is the entrance intensity at the object plane, R_2 is the object-detector distance, M is the geometric magnification factor, $A^2(\vec{r})$ and $\phi(\vec{r})$ are the attenuation map and phase shift map of the object, respectively. Furthermore, $cos\left(\frac{\lambda R_2}{4\pi M}\nabla^2\right)$ and $cos\left(\frac{\lambda R_2}{4\pi M}\nabla^2\right)$ are the 2D pseudodifferential operators in which ∇^2 is the Laplacian operator. In the clinical applications where the object–detector distance (R_2) should not be larger than 1 meter (m), and the maximum spatial resolution needed should be about 20 lp/mm, the term $\frac{\lambda R_2 \nabla^2}{4\pi M} << 1$, $cos\left(\frac{\lambda R_2 \nabla^2}{4\pi M}\right) \approx 1$ and $sin\left(\frac{\lambda R_2 \nabla^2}{4\pi M}\right) = \frac{\lambda R_2 \nabla^2}{4\pi M}$, thus Equation 2.18 was reduced to

$$I(\vec{r}_D) = \frac{I_{in}}{M^2}\left\{A^2(\vec{r}) - \frac{\lambda R_2}{2\pi M}\left(\nabla.\left(A^2(\vec{r})\nabla\phi(\vec{r})\right)\right)\right\} \qquad (2.19)$$

Equation 2.19 is the simplified Transport of Intensity Equation (TIE) and hence Wu and Liu theory recovers the TIE as a special case of their theory. From this equation, it was shown that the image contrast was proportional to the Laplacian of the object's projected phase φ, which is in turn related to the tissue's refraction index decrement δ.

It is clear that the attenuation and phase maps are differentially encoded with each other in the projection intensity $I(\vec{r}_D)$. Hence, the task of retrieving the phase map of an object, one should decode the phase information from the projections views by using the above equations.

2.4 Phase Retrieval Process

With the theory and guidelines established for the inline phase sensitive imaging, it is natural to ask whether we may retrieve the quantitative information from the phase contrast images. This problem of calculating the x-ray phase from phase contrast image is known as phase retrieval. The need for retrieving the x-ray phase shifts generated in a projection of a sample, arises from the efforts to provide quantitative tissue characterization in medical imaging applications. In the attenuation-based imaging, the projected linear attenuation coefficient (μ) is straight forward and may be retrieved directly from the intensity measurements. In this section, we present a method of retrieving the phase information from a single-phase contrast image.

2.4.1 Phase Attenuation Duality (PAD) Algorithm

Common phase retrieval methods in the literature require multiple projections (at least two projections) acquired with varying object-detector distances for retrieval of the phase-shift map of a subject [70-72]. However, this requirement of multiple image acquisitions for phase retrieval is cumbersome in implementation, and multiple exposures multiply the radiation dose. In searching for a better phase retrieval method, it has been noted that when a subject made of elements with atomic numbers $Z < 10$ is imaged with high energy x-rays of approximately 60-500 keV, the x-ray-matter interactions are dominated by the x-ray Compton scattering from atomic electrons since the x-ray photoelectric absorption and coherent scattering are diminished. In this case, both the attenuation and phase shift are all determined by subject's electron density (ρ) distributions, thereby both A^2 and ϕ are fully correlated and this full-correlation is

known as phase-attenuation duality [73-78]. Fortunately, the breast tissue is mainly composed of elements such as hydrogen (H), carbon (C), nitrogen (N) and oxygen (O) and they have atomic number Z< 10. It has been reported that the sum of weight fractions of other heavy elements in breast tissue is only 1.4%. Hence, for breast tissue, there is a strong correlation between the attenuation and phase when imaged at E > 60 keV. This duality greatly simplifies the phase retrieval to an extent that the phase map φ ($\vec{r}$) can be obtained with only a single-phase contrast projection image I ($\vec{r}_d$) by using the duality transform.

Rewriting, the Equation 2.19 in terms of position vector $\vec{r}_D$ at the detector plane, we get

$$I(\vec{r}_D) = \frac{I_0}{M^2}\left\{A^2(\vec{r}) - \frac{\lambda R_2}{2\pi M}(\nabla.(A^2(\vec{r})\nabla\phi(\vec{r})))\right\} \tag{2.20}$$

PAD method utilizes the idea of splitting the x-ray attenuation into two factors as

$$A^2(\vec{r}) = A^2_{KN}(\vec{r}).A^2_{pe,coh}(\vec{r}) \tag{2.21}$$

where A^2_{KN} denotes the attenuation generated by the Compton scattering, $A^2_{pe,coh}$ is the attenuation generated by the photoelectric absorption and coherent scattering. Imaging soft tissues at high energy x-rays i-e E > 60 keV, Compton scattering dominates the amount of attenuation generated by the soft tissue and both A^2_{KN} and φ ($\vec{r}$) are determined by the tissue's electron density (ρ) as

$$A^2_{KN} = exp\,(-\sigma_{KN}\rho_{e,p}(\overrightarrow{r})), \qquad \varphi(\vec{r}) = -\lambda r_e \rho_{e,p}(\overrightarrow{r}) \tag{2.22}$$

where $\rho_{e,p}(\overrightarrow{r})=\int \rho_e(\overrightarrow{r},z)\,dz$ is the projected electron density along the ray path, η = E/511 keV and σ_{KN} denotes the Compton scattering cross-section, which is defined by the Klein-Nishina total cross-section as

$$\sigma_{kN}(E)= 2\pi r_e^2 \left\{\frac{1+\eta}{\eta^2}\left[\frac{2(1+\eta)}{1+2\eta}-\frac{1}{\eta}log(1+2\eta)\right]+\frac{1}{2\eta}log(1+2\eta)-\frac{1+3\eta}{(1+2\eta)^2}\right\} \quad (2.23)$$

Solving Equation 2.22 for the samples projected electron density (ρ)

$$ln\,(A_{KN}^2) = ln\,(exp\,(-\sigma_{KN}\rho_{e,p}(\overrightarrow{r})) \quad (2.24)$$

$$\rho_{e,p}(\overrightarrow{r}) = -\frac{\ln A_{KN}^2}{\sigma_{KN}} \quad (2.25)$$

Substituting Equation 2.25 into 2.22;

$$\varphi(\vec{r}) = \frac{\lambda r_e}{\sigma_{KN}} ln\, A_{KN}^2 \quad = \frac{\lambda r_e}{\sigma_{KN}}\, ln\, Ð\big(I(\vec{r}_d)\big) \quad (2.26)$$

Substituting Equation 2.26 into 2.20 and after some calculations, we get the

$$Ð(I(\vec{r}_d)) = (1-\left((\lambda^2 R_2 r_e/2\,\pi M\sigma_{KN})\nabla^2\right)^{-1}.\left(\frac{M^2 I(\vec{r}_d)}{I_1}\right) \quad (2.27)$$

The detailed flowchart of this phase retrieval method is provided in Figure.2.4.

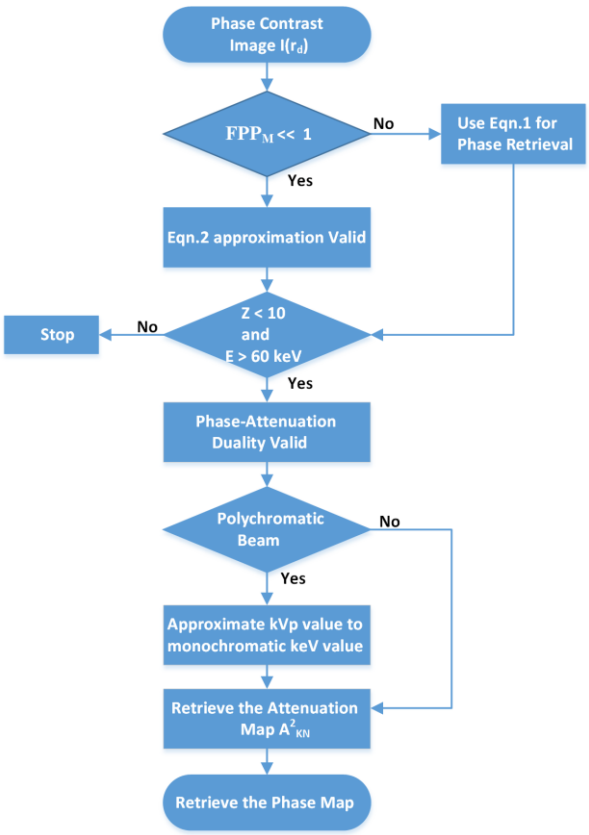

Fig.2.4. The detailed flowchart representing the process of phase retrieval using the PAD method.

2.5 Phase Sensitive Imaging vs Phase Retrieval

Phase sensitive imaging is a technique that utilizes the phase shift variations in the emerging beam from the object to enhance the image contrast. To obtain phase information, propagation is needed to allow for the interferences of the sub waves and hence a distance is introduced between the object and the detector. The overall image intensity contrast comes from both phase and attenuation. The contrast enhancement provides only qualitative information about the tissue structure. On the other hand, phase retrieval is a numerical method for retrieving the quantitative phase map φ (x,y) from the phase sensitive images. From φ (x,y), one can derive a map of the object's projected

electron densities. The electron density is an intrinsic attribute of the object, and hence the electron density map yields a quantitative image of the object's structure.

The application and usefulness of the phase retrieval has been reported in Figure 2.5, courtesy [79]. Two images of a breast cancer patient's lumpectomy specimen were acquired with a micro focus x-ray source at 40kVp. Figure 6(a) is the specimen's attenuation-based image only acquired with an SID = 66cm. Figure 6(b) is the specimen's phase contrast image acquired with SID=185cm and M=2.8. Compared to attenuation image, phase contrast image demonstrated the dark-bright fringes at enhanced tissue interfaces and boundaries. Figure 6(c) is the phase retrieved image where the retrieved phase-shift values are shown in the side gray-scale bar. Accordingly, the phase values for the specimen tissue ranges from -1400 to -1800 radians, which are consistent with the estimate based on the tissue composition, thickness profile and average x-ray energy. As the guided wire track in the specimen is a metal, so its phase values are around -3600 radians range. Outside the specimen, the retrieved phase-shifts are only -1 to -2 radians.

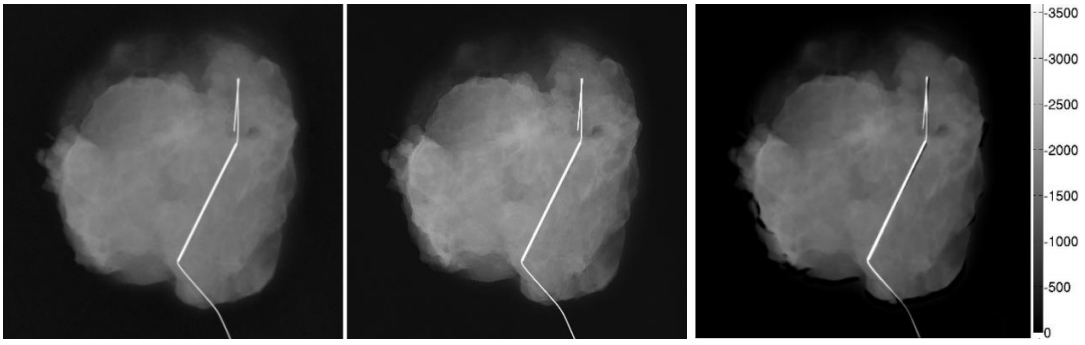

(a) **(b)** **(c)**

Figure.2.5. Comparison between the (a) conventional b) phase sensitive x ray images of the human breast lumpectomy tissue, courtesy [79]. The scale bar in each image represents a length of 1 cm. The retrieved phase map (projected phase values in radians) is shown in c.

It is worth to mention that for the phase contrast tomography, it is necessary to perform phase retrieval to reconstruct quantitative artifact-free tomograms. If phase retrieval is performed for each phase-sensitive projection image before the tomographic reconstruction, an accurate 3D distribution of electron density can be generated without the artifacts that arises from the edge enhancement at the interfaces of the two materials. It has been proposed that the phase-shift method can be employed to measure the breast density directly from the phase contrast tomography [80-83]. The volumetric breast density (VBD) can be determined from the retrieved breast phase map as [83]

$$VBD = \frac{\sum_{breast}(-\varphi(\vec{r})\lambda r_e - \rho_{e,ad}\, T_c)}{N_p T_c(\rho_{e,fg} - \rho_{e,ad})} \tag{2.28}$$

where $\varphi(\vec{r})$ denotes the breast map, T_c is the compressed breast thickness, λ is the average x-ray wavelength, $\rho_{e,fg} = 3.448\text{x}10^{23}/cm^3$ is the electron density of fibro glandular tissue, $\rho_{e,ad} = 3.108\text{x}10^{23}/cm^3$ is that of the adipose tissue.

In summary, phase-contrast imaging is the forward process of producing an image with phase enhancement, while phase retrieval is the inverse problem of deriving quantitative information about the object from the image data. The differences between the two modalities are summarized in Table 2-1 as [34].

Table 2.1: Differences between the phase-contrast image and the phase retrieved image of an object.

Notation	Phase-contrast Image I_{pc}	Phase Retrieved Image ϕ
Formation	Interference between waves of different phase shifts.	Could be retrieved from a single phase sensitive image using innovative algorithmz.
Property	The edge enhancement increases with the Laplacian and gradient of phase shift $\phi(x,y)$ and with increasing coherence degree of the x-ray.	$\phi(x,y)$ yields a map $\rho_{e,p}(x,y)$ of projected electron densities, which are the intrinsic attributes of the object
Detector configuration	One detector placed a distance downstream from the object to allow for wave diffraction; either screen/film detector or a digital detector.	With PAD algorithm, one detector is used and the same geometric setup is used for phase retrieval.
Images acquired	One exposure acquires a single phase-contrast image.	With the high energy acquisition, both the attenuation and phase shift coefficients are determined by the tissues' electron density over the ray path, and they have a full correlation. Hence, the phase contrast image is only used for the retrieval.
Clinical significance	I_{pc} provides an edge enhancement effect from tissue phase contrast, thereby improving the image data's diagnostic quality. This can potentially help in the intra tissue heterogeneity for the high precision diagnosis.	$\phi(x,y)$ provides a map of tissue projected electron densities, and therefore a quantitative tissue characterization. Combined with tomographic image data, the 3D map of the object's electron densities becomes available for tissue structural characterization and

2.6 Potential Advantages

In the last two decades, several studies have investigated the potential benefits provided by inline phase contrast imaging in comparison to attenuation-based x-ray imaging [37-50]. The enhanced image quality in the phase sensitive imaging can be attributed to a combination of several factors. First, as detailed previously, the edge enhancement effect occurs because of the superimposition of attenuation and phase shifts induced effects on the resultant image which improves the contrast of the image, most notably in areas where

both phase shifts and attenuation effects are produced, such as boundaries between materials with different properties. Thus, the edge effect has the potential to benefit breast imaging, since malignant tissue boundaries are more intricated and rough as compared to the smooth boundaries of benign breast tissue. Thus, phase sensitive imaging has the potential to detect those boundaries differences for accurate diagnosis that are difficult to distinguish based only on attenuation-based images. Second, the image quality enhancement in phase-sensitive imaging can also be attributed to the geometric magnification introduced by the air gap because of similar triangle geometry.

The magnification could potentially result in image blurring if the focal spot is not sufficiently small to minimize the geometric unsharpness that is caused by the finite focal spot size [22, 34]. On the other hand, magnification increases the sampling rate and thus the Nyquist frequency, which results in improved spatial resolution. With the employment of a micro focus x-ray source, the geometric unsharpness can be counteracted and enhance the image quality. The amount of phase shift effects detected on the imaging plane is directly related to the amount of magnification, and therefore, its selection is critical in designing the phase-sensitive imaging prototypes. Two factors must be considered when realizing magnification in phase-sensitive imaging. First, it must be large enough so that the phase shifts produced by different parts of tissue can interfere together to provide edge enhancement and image quality improvements. If it is too small, there will not be any phase induced contrast detected at the imaging plane as in attenuation-based imaging where the object is in contact with the detector. Second, if the magnification factor is too large, the spatial coherence can no longer be maintained and

the phase contrast effect spreads across the entire image instead of only enhancing the edges.

One of the benefits upon which this research is based is the ability to increase the x-ray energy using phase-sensitive imaging. It has been noted that the real and imaginary parts of the refractive index (n) changes differently with respect to the energy (E) of the incident x-ray photon [33]. For light element in human body such as hydrogen, carbon, nitrogen and oxygen, φ is proportional to 1/E, while μ is approximately proportional to $1/E^3$. This means that that for light elements, the attenuation coefficients decrease at a much faster rate than the phase shift coefficients. Furthermore, for those light elements within the diagnostic energy range, φ is two-three orders of magnitude larger than μ. Therefore, with the variations in soft tissue density, a much stronger phase-shift induced contrast will be produced in comparison to the attenuation contrast [21-24]. This creates an opportunity of utilizing higher energy x-rays for potential phase contrast soft tissue imaging. Due to the high penetrability and low absorption of high-energy x-ray photons, the radiation dose received by a tissue can also be potentially reduced.

Another key motivation to perform high energy phase sensitive breast imaging is to overcome an existing challenge in phase contrast imaging involving the number of output quanta generated with the micro focus sources due to the limited output power of the micro focus x-ray sources. The number of quanta N generated by an x-ray source is represented as

$$N \propto kV^2 . mAs \tag{2.29}$$

where *kV* represents the x-ray tube energy and *mAs* indicates a quantity representing the tube current in units of milliamperes (mA) multiplied by the exposure time in units of seconds (s). Micro-focus x-ray sources operating with large source-to-object distances can provide large transverse coherent lengths [34,52]; however, a very long exposure time is required for imaging due to the limited current of the micro-focus tubes. The distance that is introduced between the object and the detector in this approach results in fewer x-ray photons to be detected by the detector, as compared to the traditional contact mode detection under the same conditions of exposure parameters, radiation dose delivery and the capability of detectors. For example, consider a conventional x-ray source with a tube current of 10 mA and a micro focus x-ray source with a tube current of 0.4 mA, both operating at 25 kV. The reduction in tube current by a factor of 25 increases the exposure time from the standard clinical time of 1 second to 25 seconds, which hinders the clinical feasibility due to the requirement of patients to hold their breath during exposure. However, increasing the x-ray energy instead of the exposure time requires only increase by a factor of 5 from 25 kV to 125 kV, which is clinically feasible. Therefore, phase contrast imaging at high energies holds the potential to produce the same number of x-ray quanta at clinical exposure times, which is an indication of the clinical feasibility and corresponding ability to benefit the field of mammography by reducing the dose without negatively affecting the detection capability.

Chapter 3. High-energy In-line Phase Sensitive Projection Imaging Prototype and its Optimization

3.1 System Design

3.1.1 X-ray Source Specifications

A micro focus x-ray source (Model L8121-01, Hamamatsu Photonics, Japan) was used in the prototype system design as shown in Figure 3.1. The micro focus x-ray tube consists of tungsten (W) target and a Beryllium (Be) output window with a thickness of 200 μm. The source has varying focal spot sizes ranging from 5-50 μm depending on its output power (W). The distance from the focal spot to the output window is 17 mm while the x-ray beam angle is approximately 43 degrees. The source provides adjustable tube current ranging from 10-500 μA and adjustable tube voltage ranging from 40 to 150 kV, which is controlled precisely by a software application interfacing directly with the x-ray source.

Figure 3.1: X-ray Source (Model L8121-01, Hamamatsu Photonics) used in the prototype.

3.1.2 X-ray Imaging Detectors

Two imaging detectors were utilized for the optimization and image quality comparisons to provide a thorough investigation between images acquired on the prototype and commercial systems. Both the detectors have varying image formulation methods, dynamic ranges and limiting resolution values. The first detector, Figure 3.2 (a), applied the technology of computed radiography (CR), which utilizes imaging plates to absorb the incident x-rays and store the intensity information until the system performs a readout process. Computed radiography (CR) is a marketing term for photo stimulable phosphor detector (PSP) systems. When PSP absorbs x-rays, some light is also promptly emitted, but much of the absorbed x-ray energy is trapped in the PSP screen and can be read out later. The readout process formulates a digital image corresponding to the intensity values recorded at each pixel location. The CR system employed for this research (Regius 190, Konica Minolta Medical Imaging, Wayne, New Jersey, USA) provides mammography plate processing with a sampling frequency of 43.75 μm. The size of the plates inside the cassette is 24 cm × 30 cm. Typical imaging plates are composed of about 85% BaFBr (Barium Fluoro-Bromide) and 15% BaFI (Barium Fluoro-Iodide), activated with a small quantity of europium (Eu). After the acquisition, the image plate is moved into the reader unit which is scanned by a laser beam. The light released from the plate is collected by a fiber optic light guide and strikes a photomultiplier tube (PMT), where it produces an electronic signal. The electronic signal is digitized and stored.

The second detection system was an indirect flat panel CMOS detector (C7942SK-25, Hamamatsu Photonics, Japan) as shown in Figure 3.2(b). This detector is sensitive to

visible light and an x-ray intensifying screen made of Cesium Iodide (CSI) is used to convert the incident x-rays to visible light photons, which is then relayed to a large number of individual detector elements, each one capable of storing charge in response to the x-ray exposure. Each detector element has a light sensitive region, and a small corner of it contains the electronics for the read-out stage. This flat provides a pixel pitch of 50 μm with an active area of 12 cm × 12 cm with an active array of 2316 × 2316 pixels and 12-bit digital output. At 1 ×1 binning, the frame rate is 2 frames per second (fps), while at 2 × 2 binning, it is 4 fps. In this dissertation, 1× 1 detector binning has been utilized for the acquisition of images.

(a) (b)

Figure 3.2: X-ray imaging detectors used in the phase sensitive prototype: (a) CR Cassette (Regius 190, Konica Minolta) (b) Flat panel detector (C7942SK-25, Hamamatsu Photonics).

3.1.3 Geometry of the Imaging System

The prototype system allows operation in both attenuation and phase sensitive imaging modes through utilizing the corresponding configurations as depicted in Figure 3.3. The ability to employ the same system for both conventional and phase contrast images provides an extremely accurate comparison between the modes. As demonstrated in the figure, the conventional mode consists of the object in contact with the detector, while the phase contrast mode relies on the air gap between the object and the detector. As detailed in Section 2.3.2, the phase contrast effect is produced during the propagation of the x-rays towards the detector after exiting the object. The distance R_2 traveled by the x-rays before reaching the detector controls the amount of magnification, which represents a tradeoff between optimal phase contrast effect and image quality.

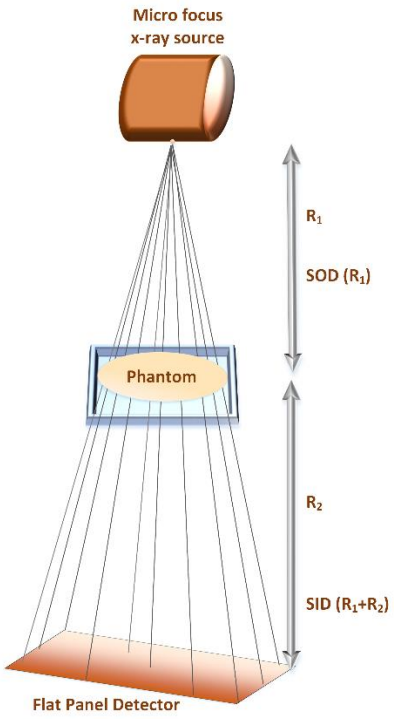

Figure 3.3: Schematics of the inline phase sensitive x-ray imaging prototype illustrating a micro-focus x-ray source, a flat panel detector and a phantom placed in a magnification geometry.

3.2 Investigation on Optimal Geometric Conditions and Design Parameters

3.2.1 Tube Energy and Geometric Magnification Selection

This study has been published and the details can be found in reference [84]. The investigation on the optimization of x-ray in-line phase-sensitive imaging prototype under different geometric and operating conditions at high x-ray energies for breast imaging application was performed. This investigation was necessary as it will provide optimal parameters for future comparisons with the clinical based breast imaging systems. The phase retrieval algorithm based on the phase-attenuation duality (PAD) was applied to the phase-sensitive images acquired by the prototype. Imaging performance was investigated at four geometric magnification (M) sets of 1.67, 2, 2.5 and 3 using an acrylic edge, and an American College of Radiology (ACR) Mammography phantom under three x-ray energies of 100, 120 and 140 kV. These three energy sets are within the diagnostic energy range. The source to image detector distance (R_1+ R_2) was fixed at 170 cm. Table 3.1 lists the geometric configurations used under various magnifications. The ACR phantom images were acquired at a constant mean glandular dose (D_g) of 1.29 mGy using the CR detector. Table 3.2 lists the milliampere second (mAs) values that were used under the four magnifications sets to acquire the ACR images under the same glandular dose.

Table 3.1: The geometric parameters used for the investigation of various geometric magnifications (M).

Magnification	**M=1.67**	**M=2**	**M=2.5**	**M=3**
Source to object R1 (cm)	102	85	68	57
Object to detector R2 (cm)	68	85	102	113.5

Table 3.2: The milliampere-second (mAs) values required for imaging at 100 kV, 120 kV and 140 kV for a constant dose of 1.29 mGy

X-ray Energy	**M=1.67**	**M=2**	**M=2.5**	**M=3**
100 kV	18.5	12	7.7	5.5
120 kV	12.12	7.88	5.06	3.65
140 kV	8.52	5.60	3.60	2.55

3.2.2 Computer Simulation on Phase Contrast Manifestation

Computer simulations are performed to compare their results with the experimental studies for the investigation of optimal geometric and operating parameters. In the computer simulations, the central parameter to calculate is the modulus of the relative phase-contrast factor *RPF* (*u*) which represents the qualitative measure of the coherence and the visibility of phase contrast at spatial frequency *u* [34, 67]. *RPF* (*u*) is given as

$$RPF(u) = c^2\, h^2 OTF_{det}\left(\frac{\boldsymbol{u}}{M}\right) \times \left[\int \frac{\pi R_2 \boldsymbol{u}^2}{ME^2} \times S_{Exit}(E)dE\right] \tag{3.1}$$

where h is Planck's constant, c is the speed of light, and $S_{Exit}(E)$ is the normalized spectrum of the average exiting beam. $OTF_{det}\left(\frac{\boldsymbol{u}}{M}\right)$ is the detector's spatial frequency response at u at the finite focal spot size. An optimal design for the phase sensitive imaging system operated at high x-ray energies should achieve a large *RPF* (*u*) value.

It is clear from Equation 3.1 that R_2 cannot be too small. If R_2 is very small, the phase-contrast information would be completely lost, as the diffracted x-ray wave needs to travel a sufficient lateral distance to disclose any phase change effects. With increasing R_2, value of M also increases. If a large M is employed, it will affect the *RPF* in terms of R_2/M ratio. That is the reason, we restricted the magnification factor such that it will exceed 3 in this investigation. Computer simulations were performed for a 5-cm thick breast with a density of 50% adipose and 50% glandular tissue, with a tungsten (W) tube target, focal spot size of 7 μm and with 2.5mm aluminum (Al) target filter. The phase-contrast visibility at a target spatial frequency of 15 lp/mm was simulated as a function of system design parameters. The computer simulations were performed with the average x-ray photon energies of 50, 60, 70 keVs to mimic the 100, 120 and 140 kV tube voltages.

3.2.3 Phantoms and Image Analysis

Two phantoms are utilized in this study to provide a comprehensive image quality evaluation and comparison of the systems. A laser cut edge of an acrylic plate of 1.42mm thickness is used as a first phantom to verify that the phase contrast effect takes place at high energy. The laser fabricated acrylic edge phantom provides a visual indication of the edge enhancement provided by phase sensitive imaging at the boundary of edge. Also, the edge profiles determined from the acrylic edge images can serve as a graphical indication of the phase contrast effect in the form of overshooting that occurs at the boundary of acrylic and the air. For the quantification of the edge, Edge Enhancement Index (EEI) is used which compares the degree of edge enhancement relative to the

absolute change in the pixel intensity for digital systems across the edge [38,47]. The EEI is defined as

$$EEI = \frac{\frac{P-T}{P+T}}{\frac{H-L}{H+L}} \tag{3.2}$$

where P and T are the peak and trough intensities at the edge, and H and L represents the intensities that would result at these locations if there were no edge enhancement at the high and low intensity regions next to the edge.

An ACR phantom (Mammo156 D, Gammex, WI, USA) of 4.4 cm thickness was used as a second phantom which contains a 7-mm wax insert inside that contains 12 sets of test objects with a 3.7 cm acrylic base as shown in Figure 3.4. With a total thickness of 4.4 cm, this phantom approximates a 4.2 cm thick compressed breast of 50 % glandular and 50 % adipose density. There are twelve simulated objects in the phantom with four fibers, four specks and four masses. The fiber like structure object thickness ranges from 0.40−0.93 mm. The micro calcification like specks object thickness is from 0.20−0.54 mm and the tumor like mass object thickness ranges from 0.25−1 mm respectively.

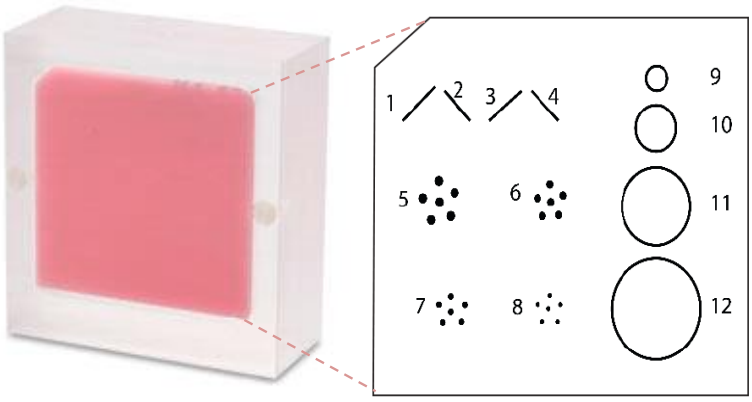

Figure 3.4. The ACR phantom used for the phase sensitive imaging acquisition.

3.2.4 Mean Glandular Dose Calculations

The purpose of this dissertation was to optimize the high energy inline phase sensitive imaging system and compare its performances with the clinical imaging systems at a specified mean glandular dose (D_g) values. It is important to mention that how D_g values are calculated throughout this study. The D_g values are calculated using the following equation

$$D_g = D_{gN}.X_{ESE} \tag{3.3}$$

where D_{gN} is an air kerma to average glandular dose conversion with units of mGy/R and X_{ESE} is the entrance skin exposure. D_{gN} is determined by experimental and computer simulation methods based on the following factors: radiation beam quality (x-ray energy or half value layer (HVL)), x-ray tube target material, filter material, breast thickness and breast tissue composition [32]. For the phase contrast images, D_{gN} was estimated based on the previously-described Monte Carlo method [85-89]. However, the previous studies only provide D_{gN} data for x-ray energies up to 35 keV. To facilitate D_{gN} calculation for higher energies, we extended the Monte Carlo simulation to 150 keV. For every x-ray energy beam utilized in this study, the D_{gN} values are computed from the x-ray spectral average of the Monte Carlo simulation-derived values for various photon energies. The x-ray spectrum is measured with an x-ray spectrometer having a 3×3×1 mm^3 Cadmium telluride (CdTe) detector (Amptek Incorporated, Bedford, Massachusetts), using a pair of tungsten collimators provided by the manufacturer. D_{gN} values decrease as the thickness of breast increase for constant beam quality and breast composition. This is because the glandular tissues farthest from the beam entrance receive much less dose in the thicker

breast as compared to thinner breasts. However, the lower D_{gN} coefficients for the thicker breast. That doesn't mean that larger breasts receive less dose. The lower D_{gN} values for a thicker breast are offset by the higher values of the entrance exposure which is necessary to achieve the desired SNR for diagnosis.

3.3 Results

3.3.1 Glandular Dose Calculation

The mean glandular dose (D_g) corresponding to the phase sensitive imaging acquisitions are calculated using Eqn.2.21 The entrance exposure (X_{ESE}) readings and the estimated normalized glandular dose (D_{gN}) values for D_g = 1.29 mGy are given in Table 3. The value of 1.29 mGy is considered as a low glandular dose when imaging a 5-cm thick compressed breast.

Table 3.3: The parameters necessary for the calculation of D_g measurements for tube voltages of 100 kV, 120 kV and 140 kV.

X-ray Energy	X_{ESE} (mR)	$D_{gN}\left(\frac{mGy}{mR}\right)$
100 kV	258	0.502
120 kV	240	0.540
140 kV	225	0.575

3.3.2 Computer Simulations and Acrylic Edge Phantom

The results of our computer simulations are summarized in Table 4 and plotted in figure 3.3. A lower kV results in higher *RPF* values. At 100 kV, all the $|RPF(u)|$ values are higher than 120kV and 140kV for a constant D_g values. The simulations reveal that $|RPF(u)|$ increases with the object to detector distance R_2 and the magnification M only up to a certain M, after which they decrease. This is because, while an increase of R_2 could increase the x-ray diffraction effects, it would reduce the x-ray spatial coherence by a higher magnification factor. Based on the results in Table 4, the optimal absolute *RPF* will be achieved around M = 2.5 for a 7 μm focal spot size of the x-ray tube. This result is valid for other focal spot sizes such as 25 μm and 50 μm.

Table 3.4: Computer simulations performed for 5cm, 50%-50% breast at a target frequency of 15 lp/mm, 7µm x-ray focal spot size and 2.5mm Al filter.

X-ray Energy	M=1.67	M=2	M=2.5	M=3
100 kV	1.013E-03	1.25E-03	1.37E-03	1.36E-03
120 kV	7.06E-04	8.72E-04	9.57E-04	9.51E-04
140 kV	5.20E-04	6.42E-04	7.05E-04	7E-04

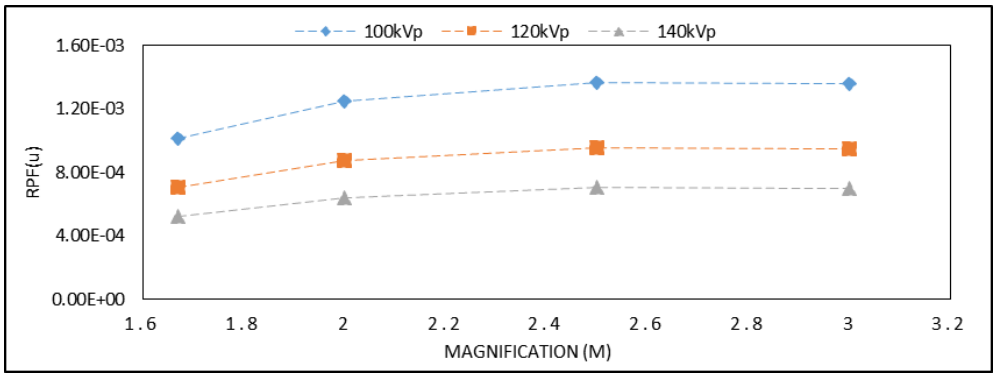

Figure. 3.5: The $|\mathrm{RPF}(u)|$ for phase contrast mammography system with a focal spot size of 0.007mm and detector pitch of 0.044 mm.

The phase contrast image of the acrylic edge acquired at 120 kV under M = 2.5 along with its edge profile are provided in figure.3.6. One can see that the edge is indicated by the white line highlighting the overshooting of the edge which demonstrates encouraging phase shift effects at this acquisition condition. This can be seen on its edge profile where there is a large overshooting at the boundary of air and acrylic. This overshooting is evident by seeing the corresponding peak (*P*) and trough (*T*) values on the graph. In the contact mode imaging, this overshooting does not exist due to the absence of any phase induced contrast. The edge line between air and acrylic is tilted; therefore, an average edge profile was generated for the calculations of EEI.

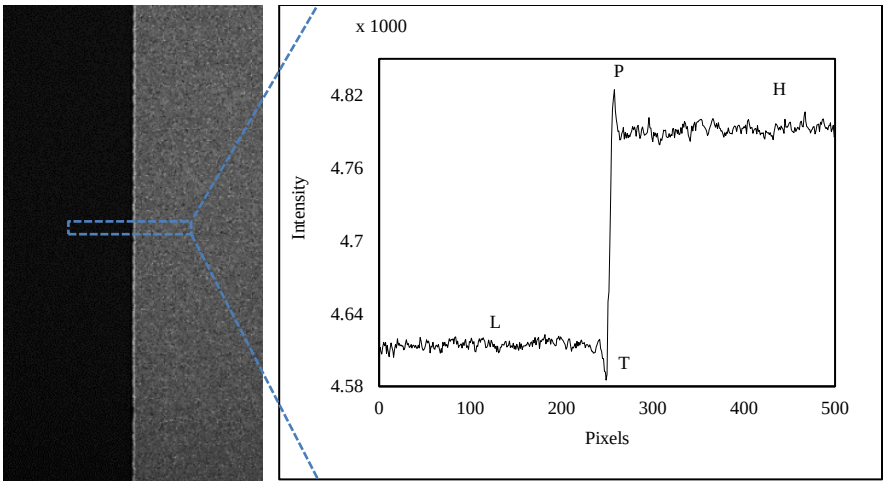

(a) (b)

Figure.3.6: Phase-sensitive image of the acrylic edge acquired at (a) 120 kV, 5.06 mAs with an x-ray focal spot size of 7 µm with the CR detector under M = 2.5 (b) The average edge profile generated for the ROI on the edge image for the calculations of the EEI values.

From the edge profiles, the EEI values were calculated for the three tube voltages under the different magnification sets. The EEI values are plotted in figure 3.6 and one can see that the highest EEI values are produced for M = 2.5. It is also evident that under all the magnifications, the EEI values for both the 100 kV and 120 kV are very close to each other. The highest EEI values were 1.5 and 1.46 at 100 kV and 120 kV under M = 2.5.

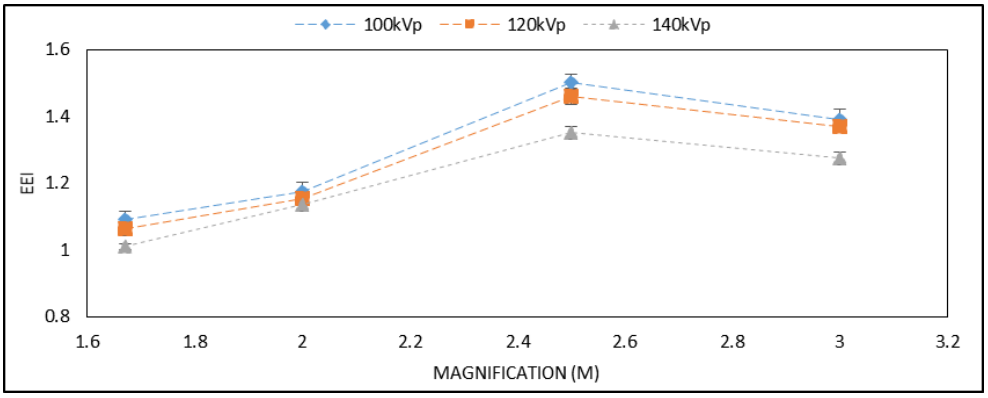

Figure. 3.7: Edge Enhancement Indicator (EEI) for the phase contrast acrylic edge phantom investigated for different x-ray energies under different magnification conditions.

As M increases from 1.67 to 2.5, the EEI increases substantially to its peak or saturation point. When M increases from 2.5 to 3, the EEI slightly decreases maintaining approximately the same values as of M = 2.5. Although the computer simulations reveal that the $|RPF(u)|$ for M = 2.5 and 3 are almost the same, the EEI values suggest that there are enough differences in those magnifications to accomplish that the phase contrast effect is greater at M = 2.5. All the EEI values of the edge phantom images validate the computer simulations yielding the highest values for100 kV that are slightly greater than 120 kV.

3.3.3. ACR Phantom Analysis

The ACR phantom phase contrast and phase retrieved images acquired at 120 kV under M=1.67 are given in Figure 3.8. The phase contrast and phase retrieved images acquired at 100 kV under M=2.5 are given in Figure 3.9 and the phase contrast and phase retrieved images acquired at 140 kV under M = 2 are shown in Figure 3.10. The visual perception

of the wax inserted objects with the phase retrieved image is better as more masses (m), speck groups (s) and fibers (f) insert are distinguishable.

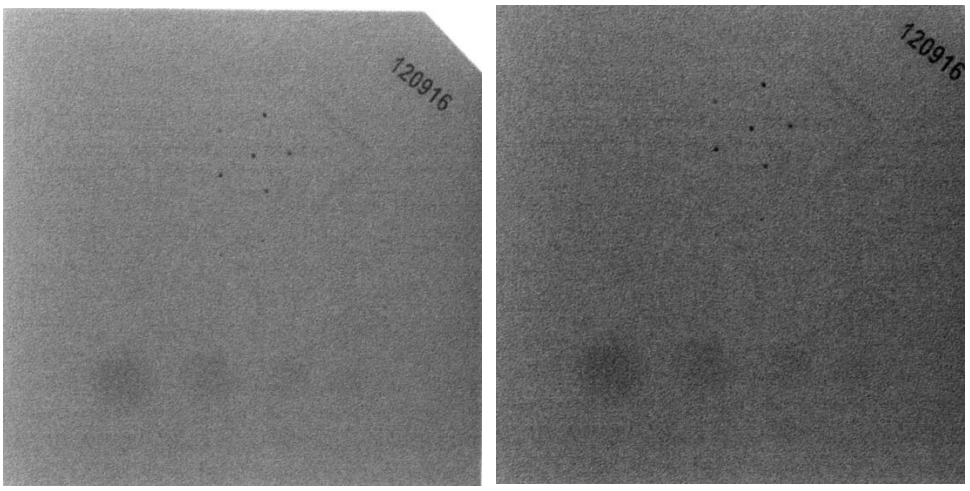

(a) (b)

Figure. 3.8: Comparison of ACR Phantom Images acquired at 120 kV under M=1.67 (a) Phase contrast image (b) Phase retrieved image with PAD.

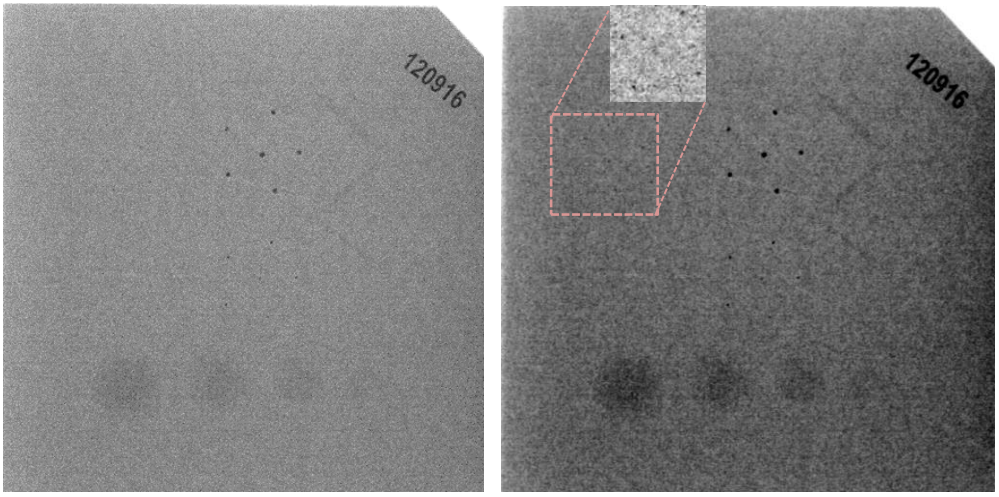

(a) (b)

Figure. 3.9: Comparison of ACR Phantom Images acquired at 100 kV under M=2.5 (a) Phase contrast image (b) Phase retrieved image with PAD.

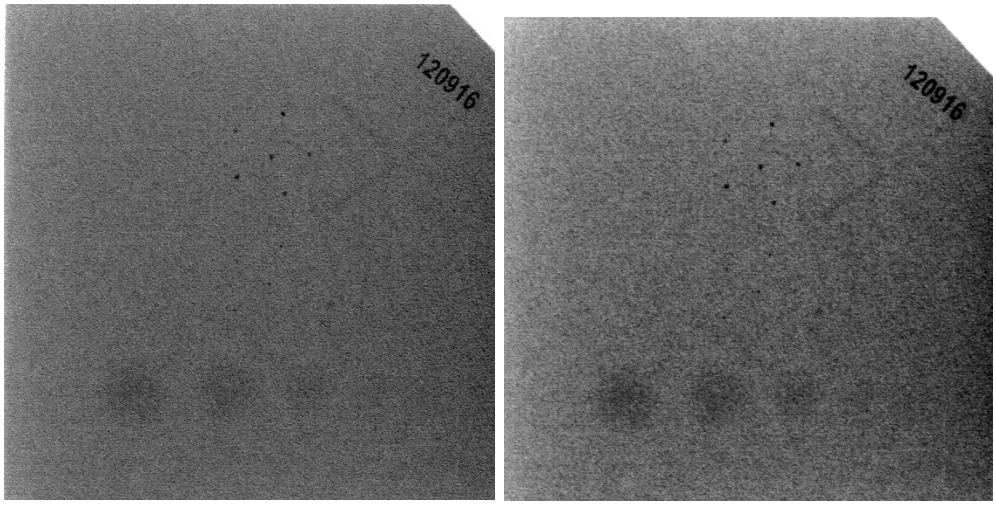

(a) (b)

Figure. 3.10: Comparison of ACR Phantom Images acquired at 140 kV under M=2 (a) Phase contrast image (b) Phase retrieved image with PAD.

The average observer scores for the investigated geometry and x-ray energies are given in Table. 3.5 and 3.6 respectively. The observers reported the lowest scores for M = 1.67 while they reported the highest scores for M = 2.5. Of the three sets of kVs investigated, the images acquired with 100 kV yielded the highest average observer scores. For example, the average observer scores for the phase contrast images at M = 2.5 under 100 kV, 120 kV and 140 kV were 8, 6.375 and 6. Furthermore, the phase retrieved images yielded higher scores than the phase contrast images. For example, with 120 kV under M = 2.5, the phase retrieved image had a score of 7.5 while the phase contrast image produced a score of 6.375. Although the ideal score for this ACR phantom will be 12, a score of 8.875 with phase retrieved image reported under M = 2.5 at 100 kV is encouraging and met the quality assurance criteria as defined by the ACR for this phantom, which indicates the feasibility of acquiring acceptable quality images with a substantially low dose.

Table 3.5: Average observer scores reported for the phase contrast images of the ACR phantom acquired with different range of x-ray energy/magnification factors.

	M=1.67			M=2			M=2.5			M=3		
	100kV	**120kV**	**140kV**	**100kV**	**120kV**	**140kV**	**100kV**	**120kV**	**140kV**	**100kV**	**120kV**	**140kV**
m	1.75	1.75	2	2	2	2.25	3	2.125	2.25	2.25	2	2
s	1.75	2	1.5	1.875	1.75	1.875	2.25	2	2	2.25	2	2
f	2	1.5	1	2	1.5	1.25	2.75	2.25	1.75	2	1.875	1.25
T	**5.5**	**5.25**	**4.5**	**5.875**	**5.25**	**5.375**	**8**	**6.375**	**6**	**6.5**	**5.875**	**5.25**

Table 3.6: Average observer scores reported for the phase retrieved image of the ACR phantom acquired with different range of x-ray energy/magnification factors.

	M=1.67			M=2			M=2.5			M=3		
	100kV	**120kV**	**140kV**	**100kV**	**120kV**	**140kV**	**100kV**	**120kV**	**140kV**	**100kV**	**120kV**	**140kV**
m	2	2	2	2.5	2.25	2.125	3.25	2.75	2.5	2.75	2.5	2.125
S	1.75	1.75	1.75	2	2	1.75	2.625	2.5	2.125	2.375	2.25	1.75
f	2.25	1.25	1.5	2	1.5	2.625	3	2.25	1.625	2.25	2	1.75
T	**6**	**5**	**5.25**	**6.5**	**5.75**	**6.5**	**8.875**	**7.5**	**6.25**	**7.375**	**6.75**	**5.625**

3.4. Discussion

The optimal in-line phase-sensitive geometry and high energy settings under the experimental conditions were investigated and compared with the computer simulations. We assessed the glandular dose levels for the absorbed dose to breast tissue, the stochastic health risk such as cancer of high energy x-ray photons can be further assessed by using the equivalent dose (H_T). It is defined by the International Commission on Radiological Protection (*ICRP*) as the product of the absorbed tissue dose (D_T) and a weighting factor (W_R) which is related to the radiation quality. For the photon radiation like x-rays and gamma rays, the weighting factor has the value 1 independent of the energy of the

radiation. Hence, the high-energy phase contrast technique does not present any higher stochastic health risk than conventional low-energy mammography technique, as compared on equal glandular dose basis.

The simulations show that Equation 3.1 indeed provided the design guidelines for clinical low dose x-ray phase sensitive imaging systems. As compared to the other geometric magnifications (*M*), the image quality and target discrimination are highest for M = 2.5 under the same glandular dose (D_g). The computer simulations based on $|RPF\ (u)|$ also validated the experimental results. Although simulations revealed that the $|RPF(u)|$ for M = 2.5 and 3 were almost the same, the experimental results established that there were enough differences in those magnifications to accomplish that the phase effects are greater at M = 2.5. The acrylic edge results indicated that encouraging phase induced contrast effects to occur at high x-ray energies in the form of overshooting at the boundary of air and acrylic. The magnification of 2.5 had the highest EEI of 1.5 for 100 kV and 1.46 for 120 kV. The observer study for the ACR phantom images established that the highest scores were reported for 100 kV in M = 2.5. Furthermore, the phase retrieved images have improved performance and detectability as compared to the phase contrast images. Both the tube voltages of 100 kV and 120 kV resulted in similar results and image performances in terms of the image contrast and observer scores. Due to the limited output power of the micro focus x-ray tubes, we aim to use 120 kV in the future studies for shorter exposure times to scan an object.

The results of this chapter have been published as reference 84.

Chapter 4. Characterization of Continuous and Pulsed Emission modes of a Hybrid Micro Focus X-ray Source for Medical Imaging Applications

4.1 Introduction

Traditionally micro focus x-ray sources have frequently been used in the micro-computed tomography (micro-CT) and specimen radiology for high resolution and high throughput imaging of small animals and specimens in the preclinical and clinical environments [90-96]. The small focal spot sizes of these sources allow to efficiently utilize the magnification geometry which is not possible with the conventional sources due to the blurring associated with their large focal spot sizes. As discussed in Chapter 3, in-line phase-sensitive x-ray imaging technique works well with micro focus x-ray tubes. When operated with sufficient source to object distances (SODs), this technique can provide relatively large transverse coherent length. The technological developments have encouraged the design of new in-line phase sensitive imaging setups which have permitted to extend the range of applications towards higher x-ray energies. The micro focus x-ray sources used in the mentioned modalities operate in a continuous mode that emits x-rays continually during its operation, and the x-ray detector records the spatially modulated wave emerging from an object/sample. Continuous emission sources utilize thermionic or field emission cathodes for the emission of electrons.

Pulsed x-ray diagnostics and inspection can reduce the radiation dose considerably. Generating x-rays as a sequence of short flashes instead of continuous radiation is a

distinguishing feature of the pulse x-ray sources. They are commonly used in diagnostic imaging such as breast and lung screening. They provide the advantage of removing the shutter utilized in breast tomosynthesis and cone beam breast CTs to block the x-rays during the source movement from one acquisition angle to the next, which avoids issues with image blur.

In this chapter, it is intended to characterize a micro focus x-ray source that can operate in both continuous and pulsed emission modes. For translating this hybrid micro focus x-ray source for advanced applications such as specimen radiography, tomosynthesis and cone beam breast CTs, it is vital to quantify its core performances in the projection imaging mode. To the best of my knowledge, this is the first detailed evaluation report of the continuous and pulsed emission modes of a hybrid micro focus x-ray source.

4.2 Hybrid Micro Focus X-ray Source

The micro focus x-ray source (Model L9181-06, Hamamatsu Photonics, Japan) is referred to as Hybrid since it operates in both continuous beam and pulsed emission modes. The continuous emission mode works with tube voltage and tube current ranging from 40-130 kV and 10-300 µA. The guaranteed x-ray tube voltage and current range in the pulsed emission mode is 80-130 kV and 50-300 µA. The target material (anode) of the source is tungsten (W) and the x-ray output window material is Beryllium (Be) with a thickness of 500 µm. The source has varying focal spot sizes ranging from 16-50 µm depending on its output power (W), which is the product of the source output voltage and current. The focal spot to output window distance (FOD) is 13 mm while the x-ray beam angle is approximately 100°, as shown in figure. 4.1. In the pulsed emission mode, the source self-

emits the x-ray beam at a frequency of 1.67 Hz, which corresponds to a pulse duration of 600 msec. The 50% duty cycle of the pulse ensures on and off times of 300 msec. During the OFF time, the current (μA) drops to zero while the tube voltage (kV) remains at the preset value. During the ON time, the current ramps up to the preset value allowing the x-ray emission to occur. The source can be synchronized to an external signal generator which allows to adjust the pulse width, duration and frequency in accordance to the 5V input square wave signal that the source would receive. The source has a full duplex serial interface communication method via RS-232 cable at 38400 bits per second data transfer speed.

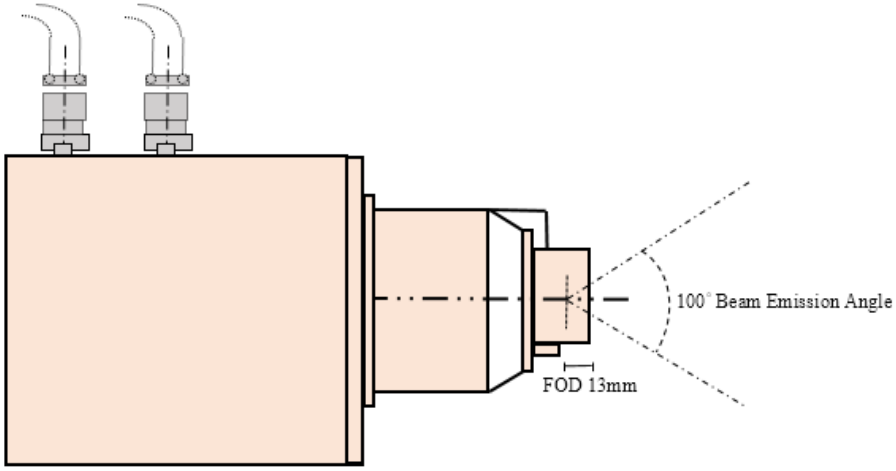

Figure 4.1. Schematics of L9181-06 x-ray source operating in continuous and pulsed emission modes.

After successfully installing the x-ray source on an optical rail, it is very important to characterize and monitor the source in both continuous and pulse emission modes on an ongoing basis to ensure reliable performance. Pulse emission mode was characterized with its self-running frequency (f) of 1.67 Hz. This ongoing and periodic evaluation will help to detect changes that may result in a clinically significant degradation in the image

quality or a significant increase in radiation exposure. The source output, beam quality, focal spot measurements, kV accuracy, spectrum analyses and spatial resolution were measured in this study.

4.3 Continuous Emission Mode Results

4.3.1 Source Output

We utilized an air-filled ionization chamber (Model 9095, Radcal Corporation, CA, USA) for the measurement of the source output for various tube voltage (kV) values. The source output was measured with the ionization chamber placed at 100 cm away from the x-ray focal spot as per the guidelines of the American Association of Physicists in Medicine (AAPM) [31-33]. The relationship between the current (μA) and exposure rate (mR/min) for various kV values are plotted in Figure 4.2. One can see that the exposure in the continuous emission mode linearly increases ($R_2 = 1$) as the current increases.

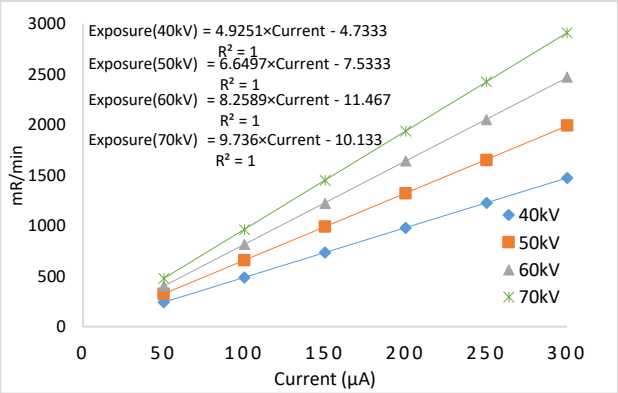

(a)

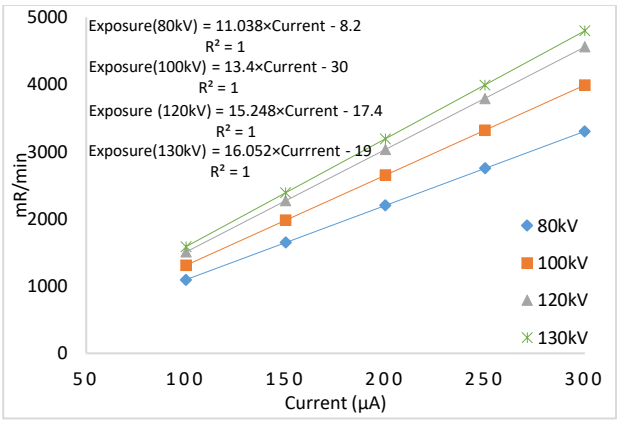

(b)

Figure.4.2. Relationship between the exposure rate (mR/min) and current (µA) in the continuous emission mode for (a) 40-70 kVp (b) 80-130 kVp.

The source output measured in the beamline with an ionization chamber placed at source to image distances (SIDs) of 50 cm, 100 cm and 150 cm under various kVs. The exposure values were fitted to $y = k.x^{-2}$, where y is the exposure rate, x is distance (cm) and k is a constant. From Figure 3(a), one can see that the output exposure values follow the inverse square law relationship with respect to the distance with high R^2 values. For an SID = 100 cm, lateral exposure values were measured to investigate the coverage of field of view (FOV). The ionization chamber was placed in two lateral distances, (a) 38 cm to left and right with respect to the central beam that corresponded to FOV of 76 cm (b) 76 cm to left and right that corresponded to FOV of 152 cm.

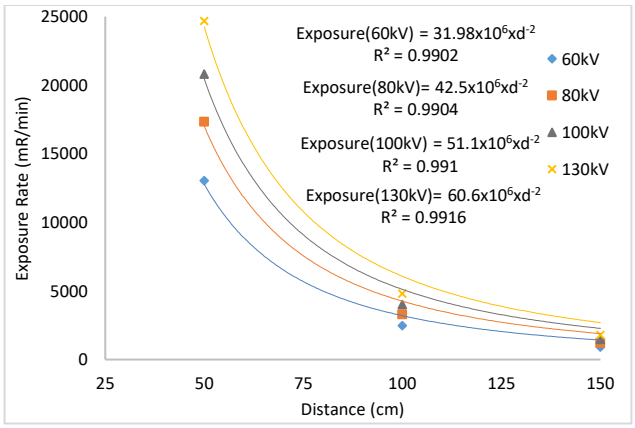

(a)

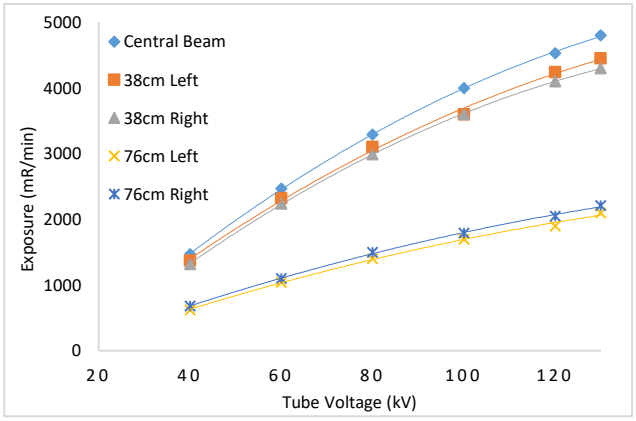

(b)

Figure.4.3. (a) Relationship between exposure rate and distance signifies the inverse square law relationship. (b) Exposure values measured at several lateral distances to investigate the coverage of field of view (FOV).

From Figure 4.3(b), one can see that lateral exposure values significantly drop as the ion chamber is laterally moved from 38 cm (FOV = 76cm) to 76 cm (FOV = 152 cm). This is because that the ion chamber placed laterally at 76 cm left or right is just outside the field of coverage which is defined by the source emission (cone) angle. For medical applications such as mammography and tomosynthesis, the FOV extends to the size of the detector which is usually about 30 cm in width. Therefore, necessary actions should be taken to narrow the FOV. X-ray collimators are routinely used for this very reason to make the size of FOV as to the desired medical application.

4.3.2 Beam Quality

Beam quality was measured using the half value layer (HVL) with aluminum (Al) filters, according to the AAPM recommendations [31, 34]. During the measurements, it was observed that even with a small thickness of 0.05 mm Al, the x-ray beam intensity drops to 27-28 % as compared to the unfiltered beam. This clearly indicates that the unfiltered x-ray beam contains many low energy photons, which do not contribute in the image formation. In fact, the majority will be absorbed by the tissue, resulting in an additional radiation dose. From the measured data, the (HVL) for different kVs are given in Table 4.1. One can see from the table that these HVL values will help in imaging tissues at reduced radiation dose levels.

Table 4.1: Half value layer (HVL) in millimeters (mm) computed for different kVs with respect to different filtration at the input.

kV	*no filter*	*1 mm Al filter*	*1.5 mm Al filter*	*2 mm Al filter*
60	*0.1172*	*1.24*	*1.62*	*1.93*
80	*0.1212*	*1.50*	*2.0*	*2.41*
100	*0.1244*	*1.85*	*2.41*	*2.97*
120	*0.1296*	*2.19*	*2.92*	*3.6*
130	*0.1317*	*2.38*	*3.16*	*3.86*

As mentioned above, the unfiltered x-ray beam has a clear majority of low energy photons that are readily blocked by Al filters with small thicknesses, hence the HVL values for the kV values are small, as shown in Figure 4.4 (a). With 1mm Al filtration at the exit window of the x-ray tube as an initial input, the x-ray beam is hardened and the low energy photons are blocked and hence the exposure output reduces as shown in Figure 4(b). HVL values can be measured from these graphs. For example, with 1 mm Al filter

at the input end for 120 kV, the exposure rate is 712 mR/min with no added filtration. The exposure rate values decrease and becomes 356 mR/min at approximately 2.19 mm of added Al filtration.

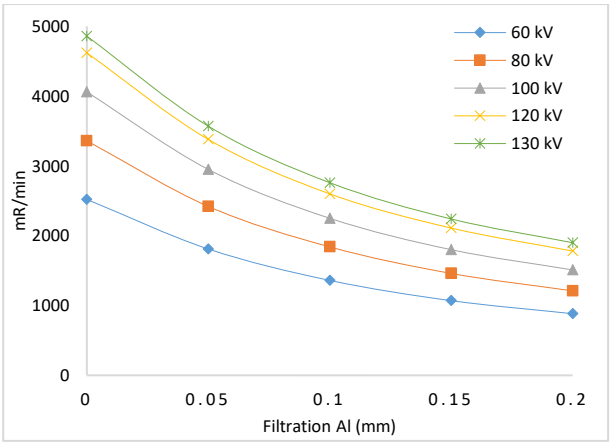

(a)

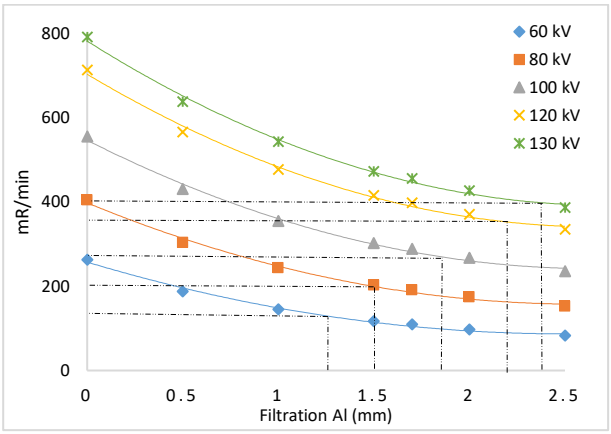

(b)

Figure.4.4. Half value layer (HVL) computed for several kVs with respect to (a) no filter at the input (b) 1mm Al filter at the input.

4.3.3 Focal Spot Size Measurements

The manufacturer's specifications for the x-ray source indicate varying focal spot sizes according to the output power rating, and it is therefore important to measure the focal spot sizes for comparing it with the specified sizes. A slit camera (IIE GmbH, Aachen, Germany) was placed at SOD = 30.5 cm and SID = 183 cm, yielding a geometric magnification factor of M = 6. A CCD x-ray detector (Image Star 9000, Photonic Science, UK) with a pixel pitch of 21.7 μm was utilized to measure the focal spot sizes according to the technical procedure specified in the literature [35, 36]. The slit camera was carefully positioned so that it was either parallel (for measuring the width of the focal spot dimension) or perpendicular (for measuring the length of the focal spot dimension) to the anode–cathode direction. Multiple transverse profiles from the center section of the slit image were averaged, and the results were used for the determination of the full width at the half maximum (FWHM) of the focal spot images. The background signal was subtracted from each profile to ensure consistent results. Complete description of the method can be found in [36]. With the FWHM determined for each slit profile, the corresponding focal spot size was calculated as

$$FS\ (\mu m) = \frac{FWHM - 10 \times M}{M - 1} \tag{5.1}$$

where FS represents focal spot size; M is the geometric magnification; and the factor 10 is the physical slit width in microns (μm). Figure 4.5 shows the slit images (448×336) acquired under three output powers of 39W, 20W and 5W representing the horizontal dimension of the focal spot with respect to the anode-cathode direction. From these images, one can visually see that (a) the slit has good alignment to ensure a more accurate

representation of an across-slit digital profile, (b) the width of the slit increases with the operating power of the x-ray tube. Thus, the width of the slit is largest for 39W and smallest for 5W.

(a) (b) (c)

Figure.4.5. Slit camera images acquired using a CCD detector: (a) 39 W (130 kV, 300µA), (b) 20 W (100kV, 200µA), (c) 5 W (100 kV, 50µA).

The focal spot sizes were measured in the two dimensions and plotted against the output power (W) and were compared to the manufacturer-provided specifications in Figure 4.6. The focal spot sizes were linearly fitted with respect to the input tube power (W). As compared to a small focal spot, a large focal spot produces a greater blur in the output images of the system, which results in a wider FWHM. For example, the 39 W horizontal slit image produces a FWHM value of 470 µm (21.7 µm × 21 pixel) as compared to a FWHM value of 315 µm (21.7 µm × 14 pixel) produced by the 20 W image. In addition, the focal spot sizes in the vertical direction are smaller than that of the horizontal direction.

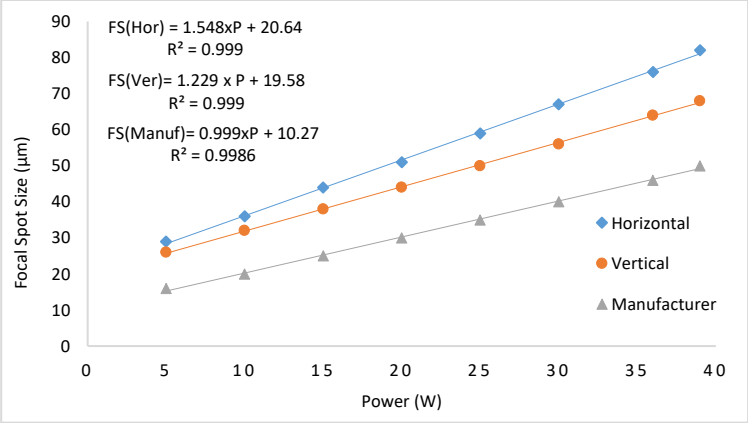

Figure.4.6. Focal spot sizes in the two planes plotted against the output power (W).

4.3.4 kV Accuracy

Accuracy of the kilo voltage was evaluated with a noninvasive kV meter (Radcal Corporation, CA, USA). As shown in Table 4.2, the output voltage was within ±1V for input voltages between 40 and 80kV, while the output voltage was within ±3V for 90-130kV.

Table 4.2: Measured output voltages of the x-ray tube.

Input kV	***Output kV (300µA)***
40	*39.4*
50	*49.7*
60	*59.5*
70	*70.5*
80	*80.7*
90	*92.6*
100	*102.7*
110	*112.7*
120	*122.5*
130	*132.7*

4.3.5 Spectra Measurements

The quality of the x-ray beam is affected predominantly by kilo-voltage peak (kVp) selection; thus it is very important to know the waveform of the x-ray beams at different energies and at different filtration levels. For the determination of the waveform, we used a compact integrated spectrometer system (X-123CdTe, Amptek Inc., Bedford, USA) which includes a cadmium telluride (CdTe) x-ray detector, a preamplifier, a digital pulse processor and a multichannel analyzer (MCA). For the 40-70 kV waveforms, we did not employ any external filtration. However, for the waveforms between 80-130 kV, we employed a 2.5 mm thick aluminum (Al) filter to remove the low energy photons and allow viewing the K edges of the target material (tungsten) prominently. The input rates for the acquired spectrum measurements were below 2500 counts/sec. The spectrum measurements in the continuous emission of the x-ray source are given in Figure 4.7. One can see the L series peaks of the tungsten (W) material for 40-70kV, while the K series peaks can be seen for the 80-130kV range.

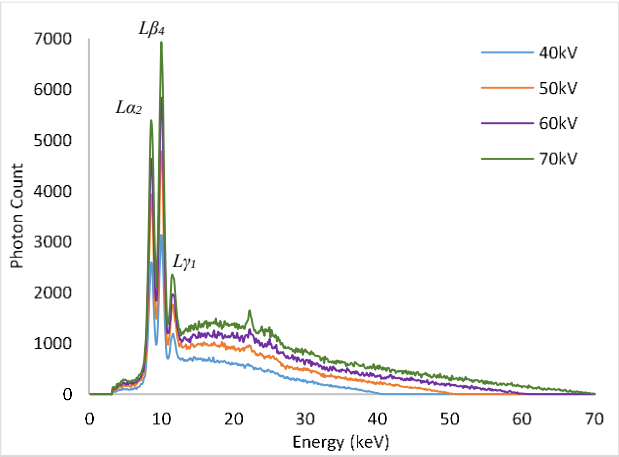

(a)

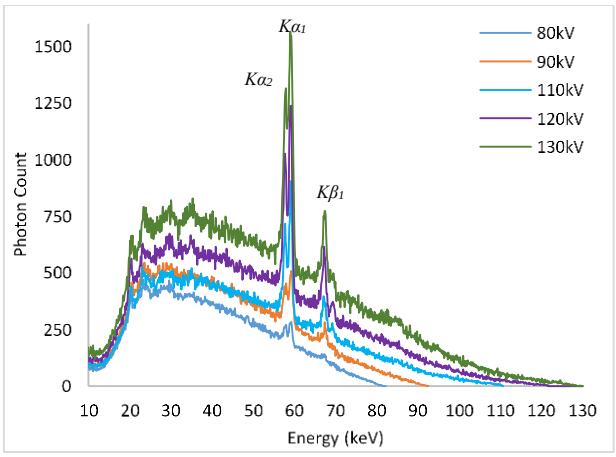

(b)

Figure.4.7. Output spectrum measurements for the tube in continuous emission mode for (a) 40-70 kV (b) 80-130kV.

4.3.6 Spatial Resolution Measurements

It is expected that the focal spot size variation with respect to output power (W) will have an impact on the spatial resolution. The same slit camera was employed for the measurement of modulation transfer function (MTF) from an oversampled line spread function (LSF) [37-39]. The slit camera was slightly tilted (2°~ 4°) and placed at a SOD of 68 cm. A CMOS flat panel detector (Hamamatsu, C7942SK-25) with a pixel pitch of 50µm was used to image the slit. The SID was 170 cm, resulting in a magnification (M) factor of 2.5. Figure 4.8(a) represents the MTF curves in the two scanning directions for a 30 W output power. As compared to the horizontal scan, the vertical scan produces higher MTF values. The cutoff frequencies (10% MTF) are 11.75 lp/mm and 10.93 lp/mm in the two scanning directions. Similar observations can be found in previous studies. The remaining assessment of the spatial resolution was performed in the vertical direction. The MTF curves for four different output powers in the continuous emission mode are

given in Figure 4.8(b). As expected, the focal spot size variation with respect to output power (W) has a direct impact on the spatial resolution. The slit images were all acquired at 100 kV except for 39 W, where 130 kV was used. The cutoff frequencies (10% MTF) for 10W, 20W, 30W and 39W correspond to 13.4 lp/mm, 12.61 lp/mm, 11.75 lp/mm and 11 lp/mm, respectively.

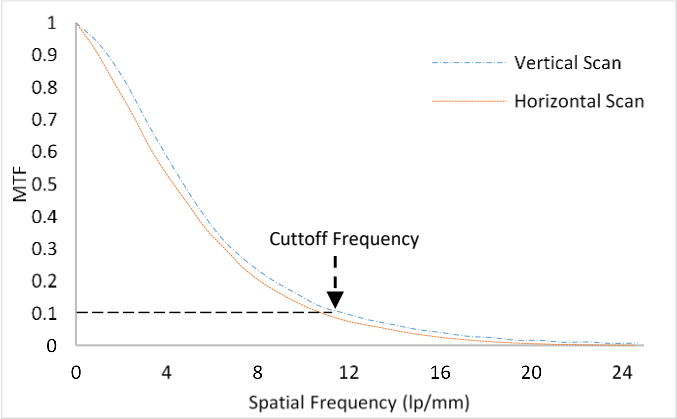

(a)

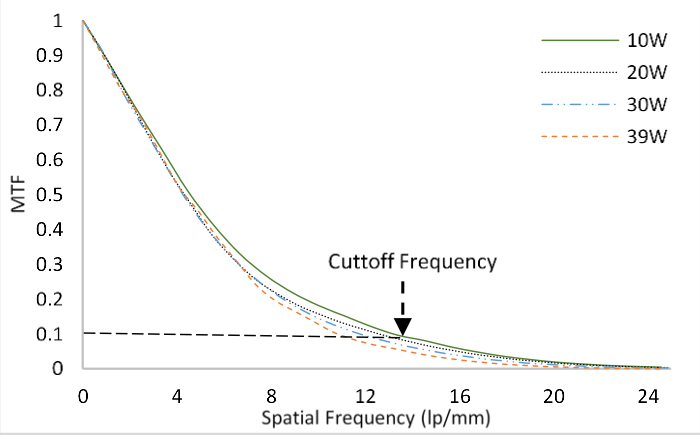

(b)

Figure.4.8. (a) MTF curves in the two scanning directions for 30W output power (W) (b) MTF curves for different output powers of the source ranging from 10-39W.

For the qualitative assessment of the spatial resolution, an ultra-high contrast resolution bar chip phantom (016B, CIRS, Virginia, USA) was utilized. The phantom has a 17.5 µm thick gold-nickel (Au-Ni) alloy bar pattern with 18 segments ranging from 5-28 lp/mm. At 10W, the 13 lp/mm bar lines are differentiated from each other, while the 11 lp/mm bar lines are differentiated at 39 W, as shown in Figure 4.9.

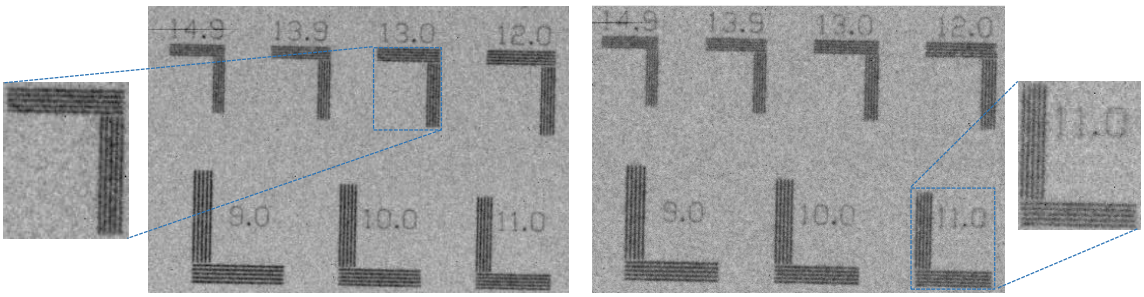

(a) (b)

Figure.4.9. The bar chip phantom images represent the qualitative assessment of the spatial resolution in (a) 10W, 100kV, 100µA (b) 39W, 130kV, 300µA.

4.4 Pulsed Emission Mode Results

4.4.1 Source Output

The source output measured for the guaranteed voltage range (80-130 kV) in the beamline at several distances was measured and the relationship between the exposure rate (mR /min) and distance (R) is plotted in Figure 4.10. One can see that the pulse output is about half that of the continuous beam output, since the pulse beam operates with a 50% duty cycle. This means that for a one-minute exposure, the on and off times are 30 seconds each for the pulse beam, as compared to a full one minute on time for the continuous beam. For example, at 100 cm for 100 kV, the source output in pulse and continuous emission mode is 2.07 R/min and 4 R/min.

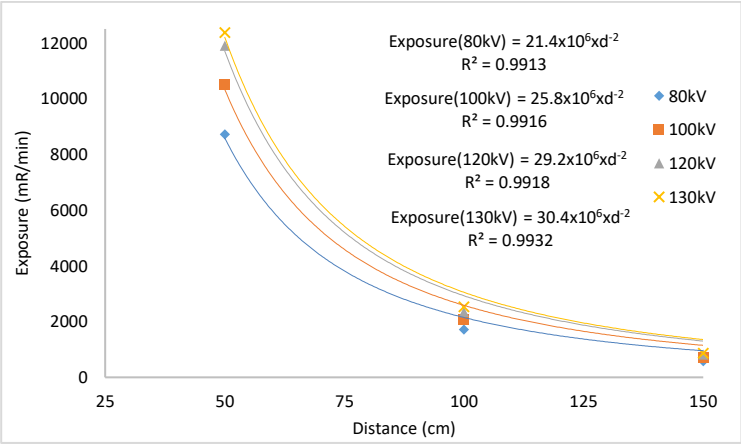

Figure.4.10. Exposure output plotted against distance shows the inverse square law relationship.

4 4.2 Beam Quality

Table 4.3 provides the recorded exposure rates using various thicknesses of Al under the guaranteed kVs in the pulsed mode. Again, with a small thickness of 0.05 mm Al, the x-ray beam intensity drops to 30-31 %. This clearly demonstrates that the unfiltered x-ray

beam contains a large number of low energy photons in the pulsed mode emission, which do not contribute to the image formation and instead result in an additional radiation dose absorbed by the tissue.

Table 4.3: Exposure readings with several thicknesses (0 to 1.5 mm) of Aluminum filters under different kVs.

Condition	*No Filter*	*0.05 mm*	*0.1 mm*	*0.2 mm*	*1 mm*	*1.5 mm*	*2 mm*
80kV, 300µA	*1.72 R/min*	*1.19 R/min*	*913 mR/min*	*593 mR/min*	*200 mR/min*	*150 mR/min*	*118 mR/min*
100kV, 300µA	*2.07 R/min*	*1.43 R/min*	*1.11 R/min*	*740 mR/min*	*276 mR/min*	*213 mR/min*	*172 mR/min*
120kV, 300µA	*2.35 R/min*	*1.65 R/min*	*1.28 R/min*	*870 mR/min*	*352 mR/min*	*281 mR/min*	*232 mR/min*
130kV, 300µA	*2.54 R/min*	*1.76 R/min*	*1.34 R/min*	*924 mR/min*	*390 mR/min*	*316 mR/min*	*262 mR/min*

The half value layer (HVL) values for 80-130 kV are given in Table 4.4. As with the unfiltered x-ray beam in continuous emission mode, the vast majority of low energy photons that are readily blocked by Al filters with very small thicknesses result in small HVL values. With 1mm Al input filtration at the exit window of the x-ray tube, the x-ray beam becomes harder and one can see from the table that these HVL values will help in imaging tissues at reduced radiation dose levels. HVL values in both emission modes are similar to each other. For example, with 1.5 mm Al at the output window of the source at 100 kV, the resultant HVL values are 2.34 mm and 2.4 mm of Al in both pulse and continuous emission modes, respectively.

Table 4.4: HVL computed for different kVs with respect to different input filtration.

kV	*HVL, no filter*	*HVL, 1 mm Al filter*	*HVL, 1.5 mm Al filter*
80	*0.1139*	*1.45*	*1.95*
100	*0.1172*	*1.85*	*2.34*
120	*0.1194*	*2.19*	*2.81*
130	*0.1206*	*2.38*	*3.0*

The HVL and kV values are linearly related for any fixed filter thickness at the output window of the x-ray tube as shown in Figure 4.11. For example, with a 1.5 mm Al filter, the HVL increases from 1.95 to 3 mm as the tube voltage increases from 80 kV to 130 kV.

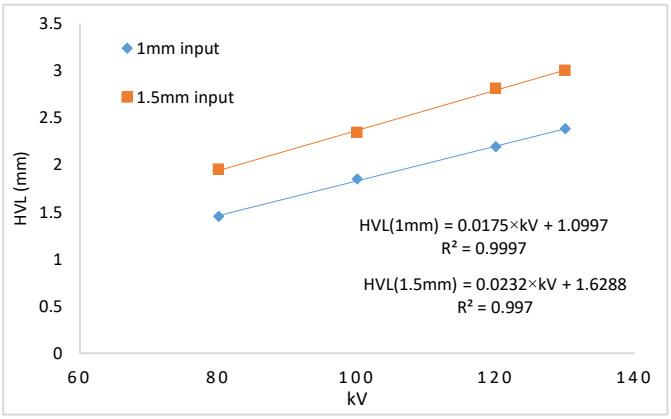

Figure.4.11. Half value layer (HVL) and tube potential (kV) relationship plotted for 1 mm and 1.5 mm Al filters at the tube output window.

4 4.3 Spectra Measurements

The kV waveforms in the pulsed emission mode of the x-ray source are given in Figure 4.12. Similarly, to the continuous emission mode, a 2.5 mm thick aluminum (Al) filter was employed to block the low energy photons for the spectrum measurements. The shapes in continuous and pulsed emission are the same, and the only evident difference is the input photon rate received by the spectrometer in the pulsed emission mode was one half that of the continuous mode. Thus, we used approximately twice the length of time to reach the same output photon count levels in the pulsed mode. The k-edge peaks are prominent and could be easily differentiated from the rest of the spectrum.

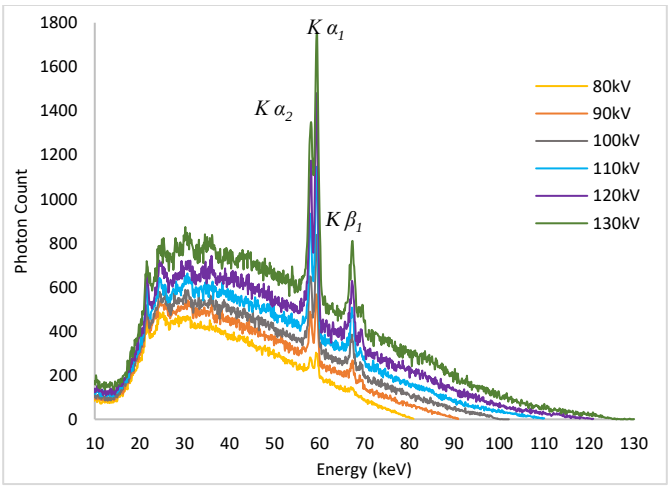

Figure.4.12: Output spectrum measurements for the tube in pulsed emission mode for 80 kV-130 kV in 10 kV steps.

4 4.4 Spatial Resolution

The MTF curves for 10 W, 20 W and 39 W output powers are given in Figure 4.13. The cutoff frequencies (10% MTF) for 10W, 20W and 39W correspond to 13.6 lp/mm, 11.95 lp/mm, and 11.27 lp/mm, respectively. This corresponds to an improvement of 20% in the spatial resolution when the output is decreased from 39W to 10W.

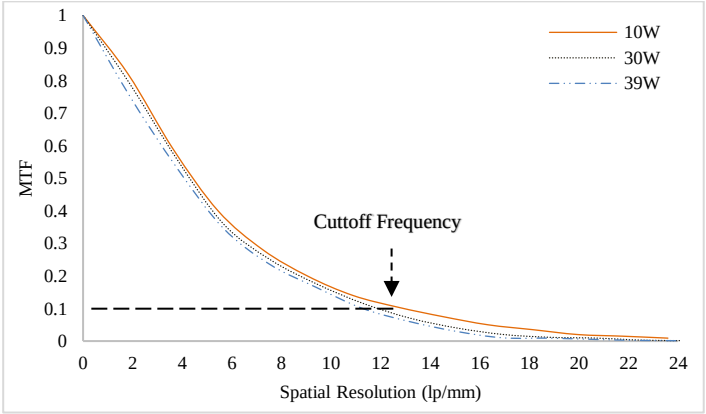

Figure 4.13: The measured MTF curves for different output powers of the tube ranging from 10W to 39W.

The qualitative assessment of the spatial resolution using the bar chip phantom validates the quantitative measurements, as shown in Figure 4.14. One can see that the 12 lp/mm bar lines are clearly differentiated at 39 W.

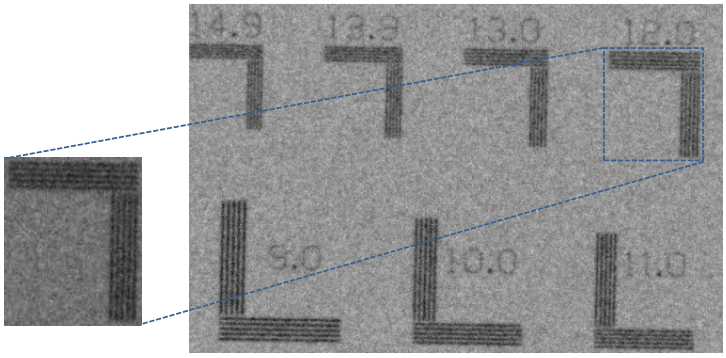

Figure 4.14: The bar chip phantom image acquired at 39W with 130kV, 300µA in pulsed emission mode.

4.5 Discussion

For the development and refinement of advanced imaging systems using the newly designed hybrid micro focus x-ray source, the first step was to characterize the performance of continuous and pulsed emission modes in projection imaging. As expected, the x-ray exposure output changes with an inverse square relationship to the distance, and linearly changes with respect to the current values. The unfiltered x-ray beam in both emission modes contains a large amount of low energy photons which are readily blocked by an aluminum (Al) filter of small thickness. This implies that these low energy photons do not contribute to the image formation and will instead be readily absorbed by the tissue/organ, adding unnecessary radiation dose. Therefore, for all the kV values, it is recommended to use a certain amount of filtration to block those unwanted low energy photons. For any fixed filter thickness at the output window of the x-ray tube, the HVL and kVs are linearly related. The wider emission angle of the x-ray beam results

in high exposure output readings at the side of the central beam. There was substantial exposure output even 38 cm to the side. Lead (Pb) collimation of the field is recommended to make the field of coverage correspond to the imaging object size. The deviation of output kVs from the preset input values was smaller for lower kVs (40-80kV) than for higher kV values (90-130kV).

The measured focal spot sizes vary linearly with respect to the output power and match the manufacturer provided data. The focal spot sizes in the vertical direction were smaller than the horizontal direction, which was visible when comparing the spatial resolution of the MTF curves. A substantial difference in the resolution can be seen at lower frequencies when comparing the spatial resolution for the two scanning directions. We can infer that the small focal spot size in the vertical direction will have a favorable impact on the spatial resolution in the z-plane of the cone beam CTs as observed in previous studies [40, 41]. Our analysis suggests that the performance of the two emission modes was similar in terms of spatial resolution. The resolution on the bar pattern are slightly different than the one predicted by the MTF curves, since 10% of the MTF value may not be an absolute baseline limit for the cutoff frequency estimation. Several studies have used a baseline limit of 5% for the estimation of the cutoff frequency, but we selected 10% for consistency with the majority of previous studies. Furthermore, the curve fitting algorithm used to generate the smooth LSF in the MTF calculation has a slight impact on the cutoff frequency range.

For both the continuous emission and pulsed emission modes, the characteristic peaks of the anode target in the spectrum were easily differentiated. For low input kVp's, $L\alpha_2$, $L\beta_4$ and $L\gamma_1$ were easily differentiated, while $K\alpha_2$,$K\alpha_1$ *and* $K\beta_1$ were differentiated for higher

kVp values (80-130 kVp). Pulsed x-ray sources have shown a valuable spatial resolution improvement in breast imaging with cone beam CTs [42]. We can expect that the pulsed emission mode, when synchronized with the digital detectors in cone beam CTs and digital tomosynthesis imaging modalities, will likely improve the spatial resolution, reduce the scattering, and reduce the radiation dose levels. With valuable results drawn from this characterization, we aim to translate this hybrid x-ray source to perform advanced imaging applications like cone beam CT, digital or phase sensitive tomosynthesis soon.

This study has been published and the details can be found in reference 97.

Chapter 5. Detectability Comparison between a High Energy X-ray Phase Sensitive and Mammography systems in imaging Phantoms with varying Glandular-Adipose ratios

5.1 Introduction

After identifying the optimal geometric and operating conditions for the high energy inline phase sensitive imaging prototype in Chapter 3, its comparison with the clinical imaging units was the next step. The aim of this investigation was to demonstrate the potential benefits of using a high energy phase sensitive imaging of breast tissues with varying glandular-adipose ratios in comparison with the commercial mammography imaging systems. Many risk factors for breast cancer have been established, which include personal and family history. High mammographic breast density has been identified as an independent risk factor for developing breast cancer, with estimates of relative lifetime risk ranging from two to six-fold as compared to non-dense breasts [98-103]. The Breast Imaging-Reporting and Data System (BI-RADS), a quality assurance tool, identifies four classes of breast densities, in order of increasing risk [104]: Class a predominantly fatty; Class b, scattered areas of fibro-glandular density; Class c, heterogeneously dense with 50-75% of fibro-glandular tissues; and Class s, extremely dense. The sensitivity of mammography for the detection of breast cancer in non-dense breasts has been reported to be 85 % [105], which is a reassuring number. However, the sensitivity drops as low as 48% in women with extremely dense breasts, i.e. Class d (greater than 75% fibro-glandular tissue) [106,107]. It has been estimated that about 28 – 30 % of breast cancers are associated with breast density, in comparison to 5 – 10&

attributed to mutations in the BRCA1 or BRCA22 gene (13). Screening modalities that are effective for this large population of women are crucial for optimal early diagnosis of breast cancers. Additional screening with magnetic resonance (MR) imaging or automated breast ultrasonography (AB US) after screening mammography increases the rate of early detection of breast cancer in women with dense breasts [107-110]. For example, a recent study showed that out of 112 breast cancer cases diagnosed in a population of 15318 intermediate risk women with dense breasts; 82 cases were detected using screening mammography, and an additional 30 cases using the automated breast (AB) ultrasonography (US) that were not detected by screening mammography [111]. The addition of AB US to screening mammography yielded an additional 1.9 detected cancers per 1000 women screened. The rates of additional cancers identified by using handheld US range between 1.9 and 5.3 additional cancers per 1000 women screened compared with mammography alone [111-115]. These studies show that there is room for improving the screening mammography in dense breast imaging.

Conventional mammography is sensitive to the attenuation coefficients of tissues. Unfortunately, dense breast tissue makes mammograms more difficult to interpret by masking potential tumor, since tumor and dense breast tissue both appear white on a mammogram. Phase-sensitive mammography is an innovative and emerging x-ray imaging technique that could potentially increase the sensitivity of the mammography. This investigation compares the detectability the low energy clinical mammography systems and the high energy in-line phase sensitive prototype using a contrast detail (CD) test pattern embedded in modular breast-simulating phantoms of varying glandular and adipose tissue compositions. To the best of my knowledge, a comparison of relative

detectability of these two modalities in imaging phantoms with varying glandular compositions has not been previously presented. This study has been published whose details can be found in reference [116].

5.2 Methods and Materials

5.2.1 Modular Breast Simulating Phantoms

Two modular breast-simulating phantoms were used in this study. The phantoms consist of multiple homogeneous slabs that mimic the adipose (A) and glandular (G) tissue composition of a human breast. The slabs are made of epoxy resins with x-ray attenuation properties corresponding to different density levels of adipose and glandular densities of the breast tissue. The slabs come in 50G-50A and 70G-30A percentages of the glandular and adipose densities. The adipose and glandular equivalent materials were uniformly blended to make the homogenous background. Three slabs of similar densities were sandwiched together to create a 5-cm thick phantom with the middle slab having a thickness of 1 cm and the outer slabs having a thickness of 2 cm respectively. As shown in Figure 5.1, the middle slab of each phantom was machined to include a contrast detail (CD) test pattern. This pattern consists of 6×6 matrix of cylindrical holes with diameters of 0.25, 0.5, 1, 2, 3 and 4.25 mm and depths of 0.1, 0.2, 0.4, 0.6, 0.8 and 1 mm.

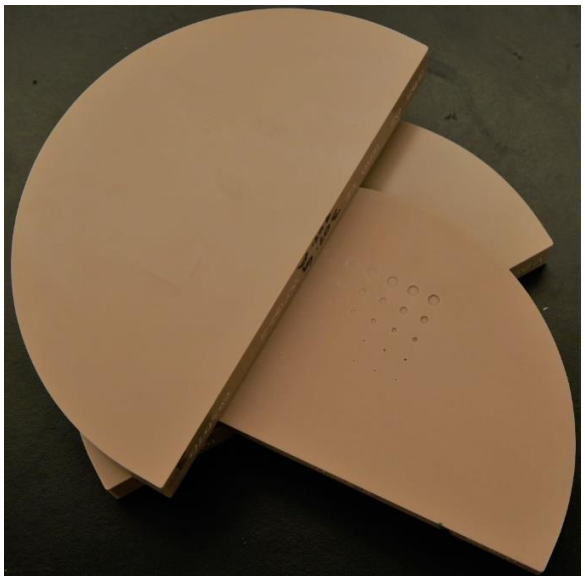

Figure 5.1. The modular breast phantom mimicking the 70G-30A percentage density with a CD test pattern machined in the middle slab.

5.2.2 Phase Sensitive Imaging Prototype

The benchtop in-line phase-sensitive x-ray imaging prototype that was characterized in Chapter 3 was used in this investigation. The prototype incorporates a micro focus x-ray source (Model L8121-03, Hamamatsu Photonics, Japan) and a 12 cm × 12 cm CMOS flat panel sensor system (C7942SK-25, Hamamatsu Photonics) with a pixel pitch of 50 μm. The geometric magnification (M) used in this study was 2.5, with a SOD = 68 cm and SID = 170 cm. The phase-sensitive images were acquired using a tube voltage of 120 kVp, a tube current of 500 μA, and an exposure time of 9 sec (4.5 mAs). A 2.5 mm Al filter was utilized to harden the beam and block the low energy photons. These specific acquisition parameters and geometry are considered as optimal for imaging soft tissues according to the investigation in Chapter 3.

5.2.3 Clinical X-ray Imaging Systems

Two conventional mammography systems were utilized in this investigation for comparison purpose with the phase sensitive imaging unit. The first system was the Senographe DS (GE Medical, United States) as shown in Figure 5.2 (a). The Senographe DS utilizes an x-ray tube with dual anode targets of molybdenum (Mo) and rhodium (Rh), and a choice of Mo, Rh, and aluminum (Al) filtration. It has an indirect conversion flat panel detector that is coupled with a scintillator of cesium iodide (CsI) doped with thallium (CSI: TI). The detector has a pixel pitch of 100 μm with a pixel array of 2294×1914 that provides a field of view of 23 cm × 19.2 cm.

The second system used was Selenia Dimensions (Hologic, Bedford, MA, USA) as shown in Figure 5.2 (b). Selenia system utilizes a tungsten (W) anode target and a choice of rhodium (Rh), silver (Ag) and aluminum (Al) filtration. It has an amorphous selenium (a-Se) flat-panel detector that performs a direct conversion of the incident x-ray photons into electric charge that migrate under the influence of the applied electric field and are collected on the detector elements. The detector elements have a pixel pitch of 70 μm with a pixel array of 4096 × 3328 that provides a field of view of 28.6 cm × 23.3 cm. The source to image-detector distance (SID) for the Senographe is 66 cm, while the Selenia has a SID of 70 cm.

Both the systems utilize an anti-scatter grid for scatter rejection. As mentioned in Chapter 2 that due to the introduction of the air gap between the object and the detector in the inline phase sensitive imaging technique, the need for an anti-scatter grid is avoided which potentially reduces the radiation dose delivered to the object. For both systems, the

phantom images were acquired using an automatic exposure control (AEC) mode that is associated with each system.

(a) **(b)**

Figure 5.2. Attenuation-based images were acquired using commercial breast imaging systems (a)Senographe DS, General Electric (b) Selenia Dimensions, Hologic.

With the AEC mode, the system automatically selects a suitable tube voltage (kV), anode/filter combination, and mAs value depending on the compressed thickness of the breast and its attenuation to x-ray, as determined by a pre-pulse x-ray exposure. In addition to the AEC mode, an automatic contrast mode (CNT) was also used for the image acquisition with Senographe. The CNT mode applies a lower kV and higher mAs values which result in dose values that are more than double as compared to its standard AEC mode acquisition. The acquisition parameters used for imaging in this investigation are summarized in Table 5.1.

Table 5.1: Parameters used for the acquisition of the phantom images.

Density	GE Senographe (AEC)	Hologic Selenia (AEC)	GE Senographe (CNT)	Phase Sensitive System
50G-50A	29kV,46mAs, 1.03mGy	29kV,116mAs, 1.42mGy	27kV,146mAs, 2.46mGy	120kV,4.5mAs, 1.33mGy
70G-30A	29kV,55mAs, 1.14mGy	29kV,142mAs, 1.57mGy	28kV,129mAs, 2.3mGy	120kV,4.5mAs, 1.3mGy

5.3 Analyses and Comparison of the Images

5.3.1 Observer Study

Performing an observer study using contrast-detail (C-D) analysis is a widely accepted as a simple and efficient method for comparison of medical imaging systems and techniques including mammography applications [117-120]. All images were randomly presented to 10 independent observers for analysis. The analysis involved each observer identifying the minimum perceptible hole/disk for each diameter in the image. All the images were displayed on a high-resolution monitor in a dark room. The monitor was calibrated using the DICOM grayscale standard display function. The reading time was unlimited for each user. C-D curves were generated for each image according to the averaged observers scores to compare the relative performance of the phase retrieved and conventional clinical images. The C-D curve relates the threshold contrast necessary to perceive an object as a function of the object's diameter. Curves for different systems or techniques can easily be compared, as a system exhibiting higher performance produces a C-D curve located closer to the x-y axis. A student *t* confidence interval was constructed around each data point for determining the variance among the observers for that disk. The corresponding confidence interval is calculated as

$$\bar{Y} \pm t_{\frac{\alpha}{2},n-1} \cdot \frac{S}{\sqrt{n}} \quad (4.1)$$

where n represents the number of samples, $\bar{Y}$ is the average value, S is the standard deviation in the scores reported by the observers for each disk and $t_{\frac{\alpha}{2},n-1}$ is the student t value corresponding to the selected confidence interval with n – 1 degrees of freedom. This study utilized a 95 % confidence interval with n − 1 degrees of freedom.

5.3.2 Contrast-to-noise ratio (CNR)

The use of C-D analyses unites the concepts of spatial resolution and contrast resolution on the same graph. It is excellent in providing the relationships visually, but it is not quantitative. For the quantitative comparison of the three different imaging systems, the signal-to-noise ratios (SNRs) of the disk targets in each phantom were calculated. The SNR of a disk target is defined according to the Rose model as follows [52, 121-123]

$$SNR = \frac{S_A - S_B}{\sqrt{\frac{(\sigma_A^2 + \sigma_B^2)}{2}}} \times \sqrt{a_D / a_p} \quad (4.2)$$

where S_A denotes the mean pixel value of the disc target averaged over a region of interest (ROI), S_B is the mean pixel value of the background averaged over an ROI of the same size, σ_A^2 and σ_B^2 are the corresponding pixel value variances, and a_D and a_p are the areas of a disk target and a pixel, respectively. The ROI size for the target disks varied with its diameter. Four ROIs of equal sizes, as of ROI of the target disks, were positioned in the background regions around each disk.

5.3.3 Figure of Merit (FOM) evaluations

The achieved CNR for any given disk also depends on the mean glandular dose (D_g). Since the three imaging systems utilized different D_g values, we define a figure of merit (FOM) for target disk imaging performances. FOM is a quantity that is used to characterize the performance of a device, system or method, relative to its alternatives and it is given as

$$FOM = {CNR^2}/{Dose} \tag{4.3}$$

The CNR for x-ray quantum limited detectors is related to the number of x-ray photons (N) as $N^{1/2}$. Since D_g is proportional to N, by squaring CNR the influence of N is eliminated in the above FOM ($(N^{1/2})^2$ / N = 1). It conveniently eliminates the parameter of exposure level from the comparative analyses [124]. Hence, the defined FOM reflects the influence that photon energy has in terms of dose efficiency. We measured the CNR and the FOM values for four target discs in the phantom which were 4.25 and 3 mm in diameter with drilled depths of 1 and 0.8 mm. The phase retrieved and clinical images acquired under the AEC modes with the two clinical units were utilized in the computation of CNR and FOM.

5.4 Results

5.4.1 Observer Study

Figure 5.3 provides the contrast-detail test pattern images of the phantoms simulating the 50% glandular (G) - 50% adipose (A) density acquired with the GE Senographe, Hologic Selenia and inline phase sensitive prototype imaging systems.

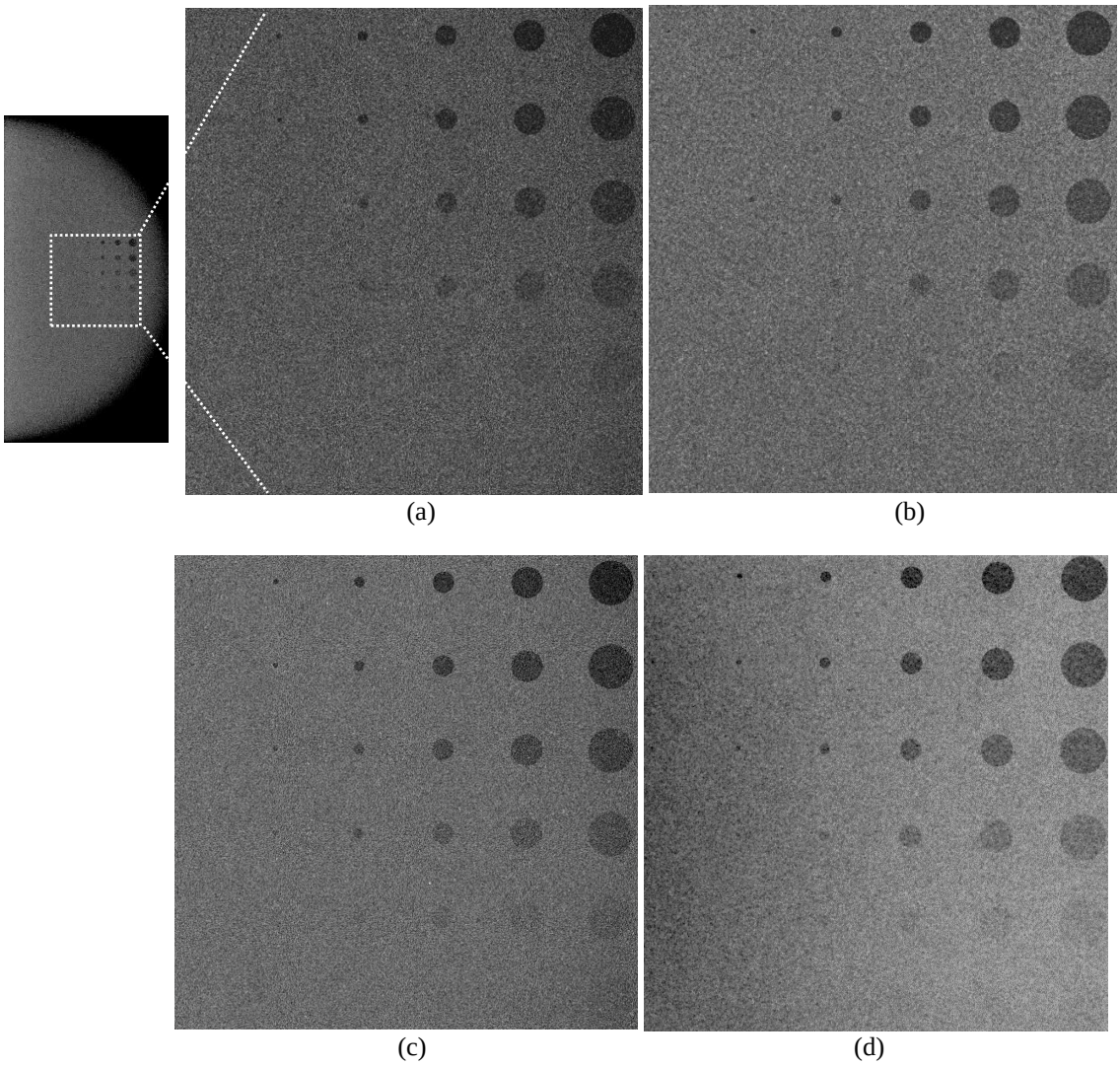

Figure 5.3. CD phantom images of the 50G-50A phantom set acquired by (a) GE Senographe at 29 kV, 46 mAs, 1.03 mGy; (b) Hologic Selenia at 29 kV, 116 mAs, 1.42 mGy; (c) GE Senographe at 27 kV, 146 mAs, 2.46 mGy; (d) Phase retrieved imaged acquired at 120 kV, 500 µA, 9s (4.5 mAs), 1.33 mGy.

Figure 5.3(a) is the AEC mode acquired image with the GE Senographe, 5.3 (b) is the AEC mode acquired image with Hologic Selenia system, 3(c) is the CNT (double dose) mode image acquired with the GE Senographe system, and 3(d) is the phase retrieved image of the phantom. Except for window/leveling, flat field correction and dark current correction, no image processing methods were applied to the images. Similarly, figure 5.4 provides the CD images of the phantoms simulating the 70% G- 30% A density acquired in the same sequence of (a)-(d) as of figure 5.3. From visual inspection, one can see that the hardest disks to perceive are in the lower left (smaller with less contrast), and the easiest disks to view are the in the upper right (larger with higher contrast) on these phantom images. From a quick visual inspection, the phase retrieved image is offering a noticeable improvement in disc detection as compared to the images acquired at similar dose levels with the clinical mammography systems. Selenia acquired AEC images have improved disc detection capability as compared to the Senographe acquired AEC images.

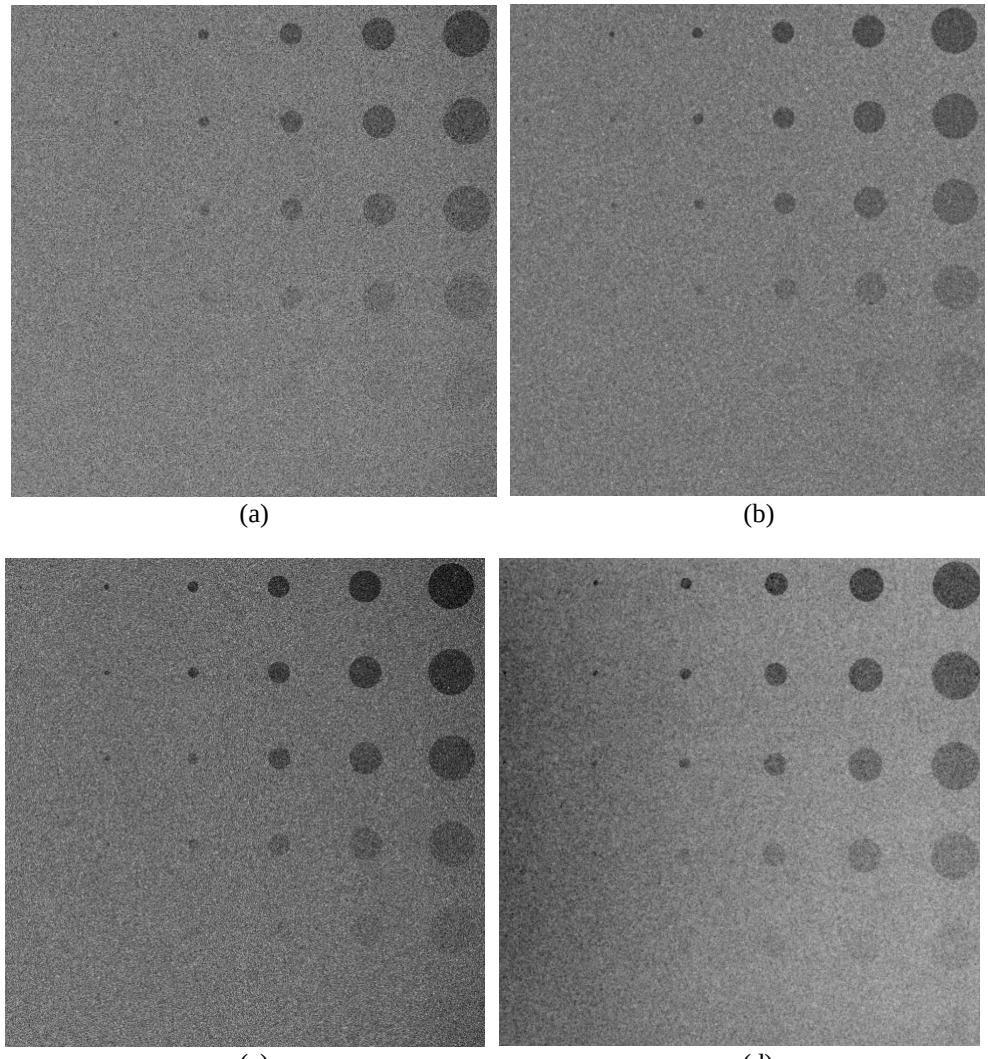

Figure 5.4. CD phantom images of the 70G-30A phantom set acquired by (a) GE Senographe at 29 kV, 55 mAs, 1.14 mGy; (b) Hologic Selenia at 29 kV, 142 mAs, 1.57 mGy; (c) GE Senographe at 28 kV, 129 mAs, 2.3 mGy; (d) Phase retrieved image acquired at 120 kV, 500 µA, 9s (4.5 mAs), 1.3 mGy.

Figure 5.5 compares the threshold contrast detection performance of the phase retrieved image with the conventional clinical mode images for the phantoms simulating the 50% glandular/ 50% adipose breast tissue. At similar dose levels, the phase retrieved image is superior to the images acquired with the two mammography systems under their AEC modes. One can see clearly on the C-D curve that the observers perceived more discs for all the disc diameters. It is worth to note that the AEC image of the Selenia yields

improved detection as compared to the AEC mode of the Senographe system. When the radiation dose was increased more than twice, the contrast resolution of the image acquired with Senographe improved and it outperformed the Selenia AEC mode image for all the discs diameters. In comparison to the phase retrieved image, the CNT mode of the Senographe yields in better detection for the discs with 2 mm and 1 mm diameters. As CNT mode applies higher dose settings—the relative noise in the image is less, and the C-D curve shows that it has better contrast resolution.

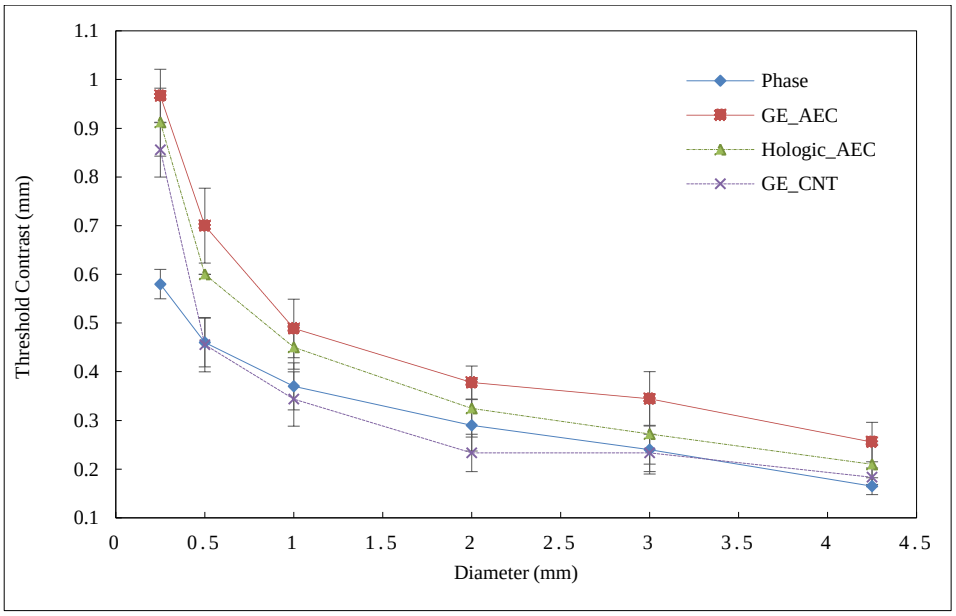

Figure 5.5. Contrast detail curve comparison of the phase retrieved image with the clinical mammography systems under various imaging protocols for the 50% glandular- 50% adipose phantom.

Figure 5.6 provides the threshold contrast detection performance of the phase retrieved image with the conventional clinical mode images for the phantom simulating the 70G-30A breast tissue. It is important to mention that with the clinical systems, the exposure and dose values both increased for this phantom, as the pre-pulse x-ray beam sensed a different attenuation due to the higher density while traversing the phantom. While

acquiring the phase-sensitive images of this phantom, the exposure values were kept at 4.5 mAs to be consistent with the first set of images. Contrary to the clinical systems, the glandular dose for imaging the 70G-30A set phantom with phase sensitive system was less as compared to the 50G-50A set. One can see from the C-D curves that the phase retrieved image is superior in detection of all the discs as compared to the clinical images acquired under the AEC mode with similar dose levels. The detection of the large discs is almost the same as the phase retrieved and Selenia acquired images. As the disc diameter decreases, the Selenia acquired image contrast reduces, which results in reduced detection of those discs. The Selenia acquired image outperforms the Senographe acquired image under the AEC mode. With double dose, the CNT mode of the Senographe exhibits improved detection of discs, as it exceeds the phase retrieved image in providing better contrast resolution for the 3 mm and 0.5 mm disks. The noise reduction provided at double dose levels with the CNT mode was still not enough to completely offset the phase retrieved image acquired at a low dose.

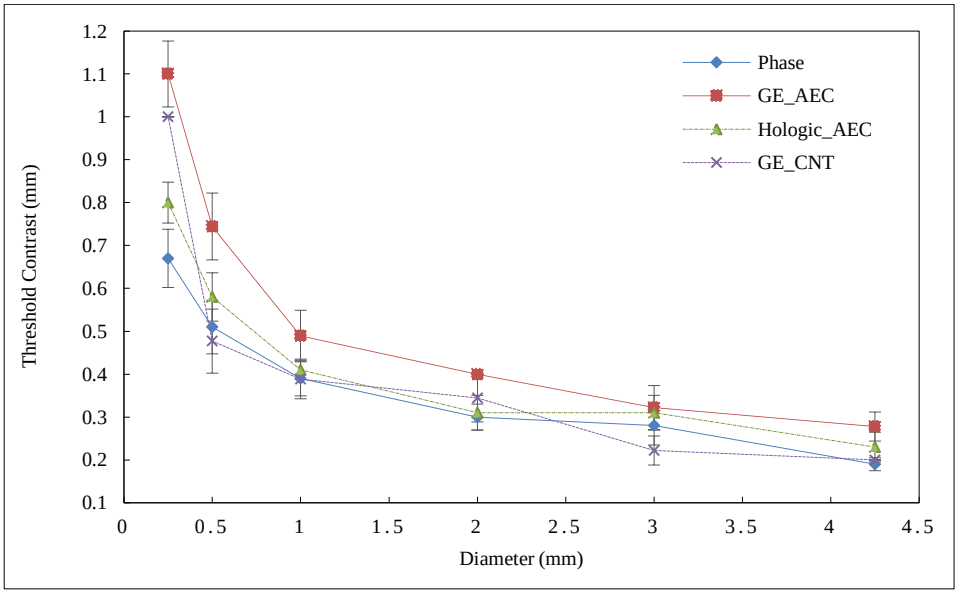

Figure 5.6. Contrast detail curve comparison of the phase retrieved image with the clinical mammography systems under various imaging protocols for the 70% G- 30% A phantom.

5.4.2 CNR and FOM Analyses

The superiority of the phase sensitive imaging prototype as seen in the observer study is further endorsed by its CNR and FOM values. The results provided in Table 5.2 for the 50G - 50A phantom set demonstrates that the ratios of CNR with the phase image to that of the Selenia acquired image ranges from 4.62 – 5.16. For example, the CNR values corresponding to 4.25 mm diameter disk with 0.8 mm depth are 6.57 and 1.34 for phase retrieved and Selenia images. The FOM values calculated for the phase images range from a factor of 22.9 – 28.53 greater than the FOM values for the Selenia acquired image. Similarly, the ratios of CNR with phase image to that of the GE acquired image ranges from 4.53 – 5.28 while the ratio of FOM values ranges from 15.9 – 21.6. For example, the CNR values corresponding to 3 mm diameter disk with 1 mm depth are 8.37 and 1.67 for phase retrieved and Selenia images that produce the FOM value for the phase retrieved image as 19.5 times greater than the Senographe acquired image.

Table 5.2. Comparison of the CNR and FOM ratios of the phase retrieved image with conventional mammography systems, Selenia Hologic (H) and Senographe GE (GE), for the 50% Glandular- 50% Adipose phantom set.

	CNR (P)	CNR (H)	CNR (GE)	FOM(P)/FOM(H)	FOM(P)/FOM(GE)
4.25mm×1mm	8.75	1.72	1.76	27.62	19.18
4.25mm×0.8mm	6.57	1.34	1.45	25.75	15.90
3mm×1mm	8.37	1.81	1.67	22.90	19.5
3mm×0.8mm	6.97	1.35	1.32	28.53	21.6

It is evident that the phase retrieved image has approximately five times the CNR of both the clinical system's images which validate the image quality improvements offered by the phase sensitive imaging system. For example, the disk with 3 mm diameter and 0.8

mm drilled depth provided the CNR values of 6.97, 1.35 and 1.32 with the phase retrieved, Selenia and Senographe images. The improvement of CNR with the phase sensitive imaging system directly impacts the FOM ratios with the two clinical systems. As compared to the Selenia system, the dose with the Senographe system was less which resulted in higher FOM values which in return yielded a smaller of FOM ratios. For the same disk, the FOM values for the Selenia and Senographe acquired images were 2.30 and 2.70 which resulted in FOM ratios of 22.9 and 19.5 respectively.

Both the clinical systems applied higher dose for adequate image quality for the denser phantom. With our inline phase sensitive imaging prototype, we were able to maintain the image quality enhancement without increasing the exposure and dose to the denser phantom. Table 5.3 provides the CNR and FOM values for the 70G - 30A phantom set. The ratios of CNR with the phase image to that of the Selenia acquired image ranges from 4 – 4.95. The FOM values calculated for the phase images range from a factor of 19.32 – 29.64 greater than the FOM values for the Selenia acquired image. Similarly, the ratios of CNR with phase image to that of the Senographe acquired image ranges from 4.41 – 5.12 while the ratio of FOM values ranges from 17.1 – 23.06. This comparison has significance since the phase images were acquired at a reduced dose as opposed to the clinical images, yet still, provide a noticeable image quality enhancement in terms of CNR and FOM values. Taking the same disc of 3 mm diameter and 1 mm depth, the FOM ratios of phase retrieved to Selenia and Senographe acquired images are 29.64 and 23.06 which are slightly higher to the FOM values of the 50G - 50A phantom set due to an acquisition with less dose. Higher CNR values warrant a good contrast resolution, less relative noise and thus better image quality. Increasing the mean number of photons (N)

incident upon a detector and reducing the scatter by employing an anti-scatter grid reduces the relative noise and improves the contrast resolution. One can see from figure 5.3 and 5.4 that the disks offer a much stronger signal with the phase retrieved image as compared to the two opposing images. It is worth to mention that the boundaries of the disks are sharper with the phase retrieved image. It is a well-known fact that with the employment of geometric magnification in clinical radiology, the boundaries of tissues are obscured due to the blurring caused by the finite focal spot size of the x-ray tubes. Phase contrast imaging technique demonstrates the edge enhancement effect at the interfaces of different tissues or materials while providing additional CNR for the diagnostic purposes.

Table 5.3. Comparison of the CNR and FOM ratios of the phase retrieved image with conventional mammography systems, Selenia Hologic (H) and Senographe GE (GE), for the 70% Glandular- 30% Adipose phantom set.

	CNR (P)	CNR (H)	CNR(GE)	FOM(P)/FOM(H)	FOM(P)/FOM(GE)
4.25mm×1mm	8.30	1.76	1.76	26.85	19.50
4.25mm×0.8mm	6.87	1.52	1.50	24.67	18.39
3mm×1mm	8.77	1.77	1.71	29.64	23.06
3mm×0.8mm	6.36	1.59	1.44	19.32	17.10

5.5. Discussion

With this investigation, we demonstrated the potential benefits of using high energy x-rays for phase sensitive breast imaging. Two state of the art commercial clinical imaging systems were utilized that are routinely used for breast cancer screening in the U.S. Since, both the clinical systems had different x-ray tube targets and filter settings; hence we cannot apply the same tube current (mA) and exposure time (s) settings. For a fair comparison, we allowed both systems to apply their own optimized techniques, determined by their automatic exposure control (AEC) settings. With increasing breast density, the AEC modes of the two commercial systems selected higher mAs values, based on the attenuation to x-ray determined by the pre-pulse x-ray exposure. This increase in mAs resulted in higher dose levels, which in response ensures adequate image quality to facilitate diagnosis and interpretation. It is important to mention that the detector quantum efficiency (DQE) decreases itself with an increase in the x-ray energy, as do the attenuation and phase coefficients of tissue. Consequently, the use of a high energy x-ray beam is inherently disadvantageous for phase imaging in a comparison study with low energy attenuation-based clinical images. However, due to the limited output power of the micro focus x-ray tubes, a high energy x-ray beam is required for phase imaging in order to reduce the exposure times to clinically acceptable values.

For the 50% G – 50% A density phantom, the observer study, contrast-to-noise ratio (CNR) and figure of merit (FOM) comparisons all indicated a large CNR improvement with the phase retrieved image as compared to the two commercial imaging systems acquired under their AEC modes at similar dose levels. The CNR improvement in the

phase retrieved image was sufficient to detect the smallest discs that were undetectable by both commercial systems. With a double dose, the detectability of the discs improved due to the noise reduction provided by the system under its CNT mode. As compared to the phase-sensitive image, double dose provided improved contrast resolution for the 2 mm and 1 mm disks. The clinical systems had to increase the dose to provide adequate image quality for the denser phantom. With our system, we were able to maintain the image quality enhancement without increasing the dose to the denser phantom. Thus, the comparison of 70G-30A phantom is more significant, since the phase images were acquired at a reduced relative dose as compared to the AEC mode clinical images, yet still provide a noticeable image quality enhancement regarding the disks perception, CNR and FOM values. At double dose, the contrast resolution of the GE system for the 3 mm and 0.5 mm disks improved as compared to the phase sensitive image. For detectors with small components of additive noise, where most of noise is a result of x-ray quantum fluctuations, the ratio of squared CNR to exposure is essentially independent of the exposure level; thus, FOM would be expected to be a measure of performance that would not change with incident exposure.

Under the AEC acquisition mode of Senographe, the small disc diameters (0.5 and 0.25 mm) for the 50G-50A image were slightly better perceived by the observers than that of the 70G-30A image. With the CNT, the observer study indicated that the discs with a diameter of 2, 1, 0.5 and 0.25 mm of the 50G-50A image were more distinguishable as compared to the 70G-30A image. For example, the 2 mm diameter disks produced an average score of 0.233 and 0.344 with the 50G-50A and 70G-30A images. With the phase sensitive system, the 50G-50A images produced slightly higher scores for all the discs as

compared to the 70G-30A image. Furthermore, the observer study indicates that the AEC mode images acquired with the Hologic system had higher disk perceptibility and detection as compared to AEC mode images of the GE system. The pixel pitch of the GE system is larger that results in reduced noise levels and less standard deviation among the pixel values of an ROI since it can capture more incident number of photons. Thus, the GE system produced similar CNR values and thus high FOM as that of the Hologic system at low radiation dose levels.

The results of this chapter are published in reference 116.

Chapter 6. Heterogenous Dense Breast Phantom Imaging using the High-energy In-line Phase Contrast and Conventional Imaging Systems

6.1 Introduction

With the optimal imaging parameters, the high energy in-line phase sensitive x-ray imaging of homogenous background dense phantom showed superiority in terms of contrast resolution, spatial resolution and contrast to noise ratios. In this chapter, we are utilizing a heterogenous background phantom in which glandular and adipose equivalent materials are non-uniformly blended. A heterogenous phantom was used to mimic the real breast backgrounds and the detectability of simulated tumors within that background was compared using the high energy inline phase sensitive and conventional imaging systems at similar radiation dose levels. For conventional imaging systems, a commercial mammography system and a benchtop prototype was utilized. As mentioned in the previous chapter, high mammographic breast density has been identified as an independent risk factor for developing breast cancer, with estimates of relative lifetime risk ranging from two to six-fold as compared to non-dense breasts. With this study, we aim to compare the sensitivity of the conventional and phase sensitive imaging systems using the heterogenous background phantom mimicking a dense breast.

6.2 Methods and Materials

6.2.1 Heterogenous Dense Breast Phantom

A modular phantom was employed that comprised of multiple slabs mimicking the adipose and glandular composition of a breast tissue. The slabs were made of epoxy resins with x-ray attenuation properties like 70-30 adipose-glandular percentage density. The adipose and glandular equivalent material were homogenously blended for uniform background slabs, while heterogeneous blending was used for non-uniform background slabs. Three slabs were sandwiched together to create a 5-cm thick phantom with the middle slab having a thickness of 1 cm and the outer slabs each having a thickness of 2 cm as shown in Figure 6.1.

Figure 6.1. Heterogenous phantom mimicking the 70% glandular- 30% adipose breast density. A contrast detail test pattern was embedded to simulate different tumor sizes.

The front slab facing the x-ray tube had non-uniform background while the middle and the back slabs had uniform backgrounds. To simulate different sizes of the tumors, the middle slab was machined to include a contrast detail (CD) test pattern. This pattern

consisted of a 6×6 matrix of circular discs having diameters of 0.25, 0.5, 1, 2, 3 and 4.25 mm with drilled depths of 0.1, 0.2, 0.4, 0.6, 0.8 and 1 mm.

6.2.2 Operating Parameters for Phase Contrast and Conventional Imaging Systems

The benchtop inline phase sensitive prototype was used for the acquisition of phase sensitive imaging at geometric magnification (M) of 2.5, with source to object distance (SOD) = 68 cm and source to image detector distance (SIDD) = 170 cm. The phantom images were acquired at 120 kV, 500 µA, 4.5 mAs under mean glandular dose (D_g) level of 1.3 mGy with a 2.5 mm thick aluminum (Al) filter for beam hardening. After the acquisition, phase retrieval process was performed using the phase-attenuation duality (PAD) algorithm.

The same commercial system, Selenia Dimensions 3D, (Hologic, Marlborough, USA) as discussed in detail in Chapter 5 was used for the acquisition of the low energy attenuation-based images. The phantom image was acquired at a focal spot size of 300 µm using the automatic exposure control (AEC) mode of the system at 30 kV, 142 mAs with W/Rh target/filter settings that resulted in a mean glandular dose (D_g) of 1.36 mGy, respectively. The HVL thickness corresponding to these settings was 0.533 mm Al. The acquisition parameters that were utilized for imaging in this study are summarized in Table 6.1.

Table 6.1. Parameters used for the acquisition of the phantom images with the phase sensitive and clinical mammography system.

Phase Sensitive Image (P1)	Attenuation Image (Hologic)
120kV,4.5mAs,239mR,1.3mGy	30kV,142mAs, 596mR, 1.36mGy

After the acquisition, the images were presented to observers for contrast detail analysis as detailed in section 5.3.2. Furthermore, contrast to noise ratio and figure of merit (FOM) were measured as detailed in section 5.3.3 and 5.3.4.

6.3 Results

6.3.1 Observer Study Analysis

Figure 6.2 provides the attenuation-based image of contrast-detail test pattern embedded in the 70% glandular (G) - 30% adipose (A) density phantom. This image was acquired with the Selenia Dimensions 3D imaging system. Excluding window/leveling, no image processing methods were applied to the image. From a quick visual inspection, it is noted that with the heterogenous background, the perception and contrast of the disks have been reduced.

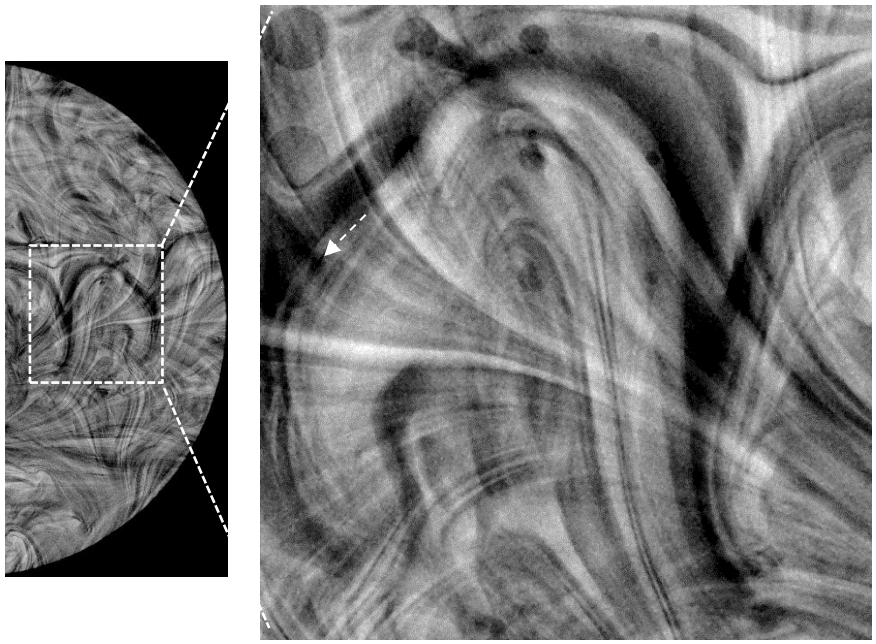

Figure 6.2. Attenuation-based image of the contrast detail test pattern embedded in the 70%G-30%A phantom set acquired by Hologic Selenia Dimension 3D at 30 kV, 142 mAs, 1.36 mGy.

Figure 6.3 provides the phase retrieved image of the contrast-detail test pattern embedded in the phantom simulating the 70% glandular (G) - 30% adipose (A) density. The phase retrieval process was performed on the phase sensitive image which was acquired with the inline phase sensitive imaging prototype. From a quick visual inspection, it is noted that with the phase retrieved image has better contrast and perception of the disks (simulated tumors) as compared to the attenuation-based image.

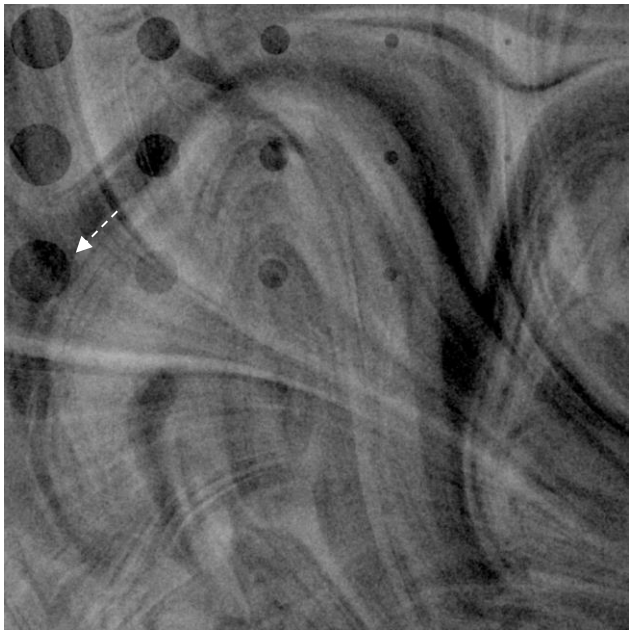

Figure 6.3. Phase retrieved image of the contrast detail test pattern embedded in the 70%G-30%A phantom set acquired by the inline phase sensitive prototype at 120 kV, 4.5 mAs, 1.3 mGy.

Figure 6.4 compares the threshold contrast detection performance of the phase retrieved image with the clinical attenuation-based image for the heterogenous phantoms simulating the 70% glandular/ 30% adipose breast tissue. Under the similar dose levels, the phase retrieved image is superior in terms of target discs detection and their perception in the heterogenous background. On the C-D curve, it is noticeable that the observers perceived more discs with less drilled depths. The contrast resolution improvements of

the phase retrieved image are visible with the large disc diameters. For example, for the 4.25 mm diameter discs, the observers reported the threshold contrast of 0.37 for the phase retrieved image which is about 51% less than the threshold contrast of 0.56 for the attenuation-based image. Therefore, a lower threshold contrast was sufficient to detect the discs with small drilled depths.

The superimposition of the glandular and adipose equivalent materials has a strong influence on the detectability of the simulated tumors. For example, the 4.25 mm diameter disc with 0.6 mm drilled depth, highlighted by white arrow on figure 6.2, is hardly visible on the attenuation-based image. The same disk, highlighted by white arrow on figure 6.3, has been perceived by all the observers successfully with the phase retrieved image. Therefore, the inline phase sensitive imaging prototype distinguished both the larger and smaller diameter discs in the heterogenous background in comparison to the attenuation-based clinical system.

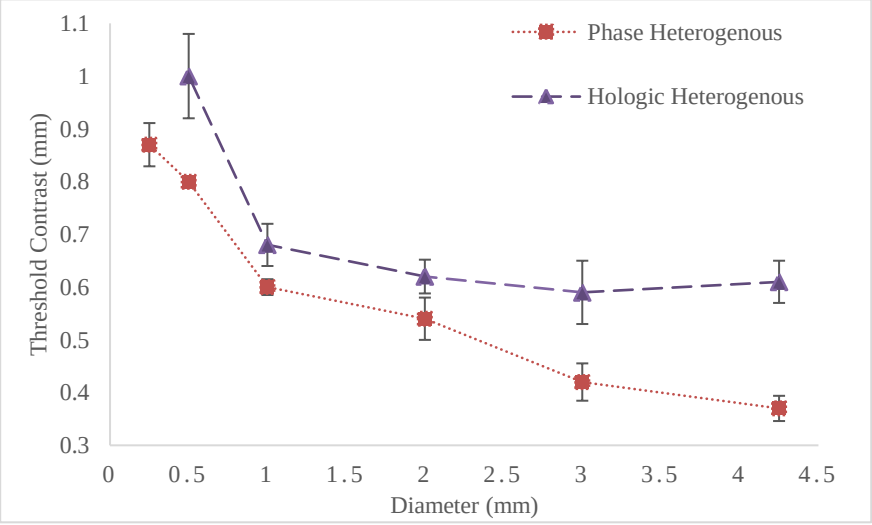

Figure 6.4: Contrast detail curves generated with the heterogenous background 70G-30A phantom for comparisons of the inline phase sensitive prototype with the clinical mammography system under similar radiation dose levels.

Figure 6.5 compares the threshold contrast detection performances of the phase retrieved image with the clinical attenuation-based image for both the homogenous and heterogenous phantoms that are simulating the 70% glandular/ 30% adipose breast tissue. In this comparison, it is evident that with the heterogenous background, the perception of the discs reduces to a significant extent. This is an intrinsic problem associated with mammography that it provides a 2D image of a 3D object. This superimposition of the soft tissue on the discs (simulated tumors) results in a reduced detection.

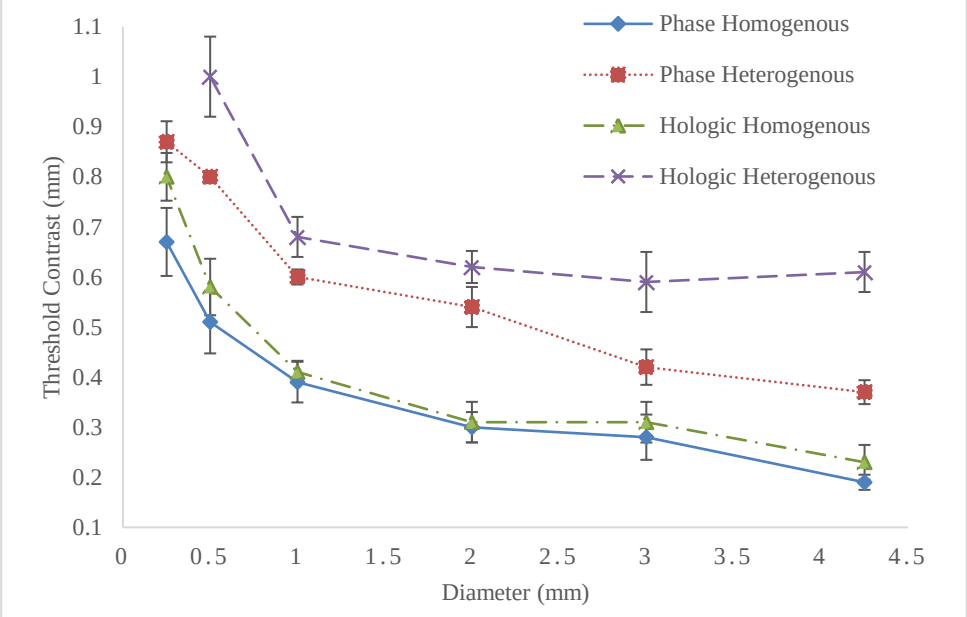

Figure 6.5: Comparisons of the contrast detail curves generated with homogenous and heterogenous backgrounds 70G-30A phantoms for the comparisons of inline phase sensitive prototype with the clinical mammography system.

6.3.2 CNR and FOM Analyses

The superiority of the phase sensitive imaging prototype as noticed in the observer study is further endorsed by its CNR and FOM values. The results provided in Table 6.2 demonstrates that CNRs calculated for the disks with the phase sensitive image is at least

3.5 times greater than of the Selenia acquired image for the heterogenous background phantom. For example, the CNR value for the 3-mm diameter disk with 1-mm depth was 2.93 and it was 0.75 for the similar disk in phase retrieved and Selenia images. The FOM values calculated for the phase sensitive image is at least 13 times higher than the FOM values for the Selenia acquired image. The higher CNR and FOM values signify that we can further reduce the glandular dose for the image acquisition with the inline phase sensitive imaging prototype which is significant in-patient imaging.

Table 6.2. Comparison of the CNR and FOM ratios of the phase retrieved image with conventional Selenia Hologic (H).

	CNR (P)	CNR (H)	FOM(P)/FOM(H)
4.25mm×1mm	4.25	1.19	13.34
4.25mm×0.8mm	2.55	0.71	13.49
3mm×1mm	2.93	0.75	15.95
3mm×0.8mm	2.17	0.607	13.36

6.4 Discussion

This study demonstrated the efficacy of the inline phase sensitive imaging system in imaging breast equivalent phantoms with heterogenous backgrounds. The system had already shown its effectiveness in imaging the standard homogenous breast phantoms that are routinely used for quality assurance purposes in the clinical world. For the dense breast phantom, the observer study and contrast-to-noise ratio (CNR) analyses all indicated a large SNR improvement by the phase contrast images as compared to the conventional image acquired at similar dose levels. The CNR improvement in the phase contrast images was enough to detect the smaller discs which were undetectable by the conventional systems. The simulated tumors were more perceptible on the phase contrast

image in the superimposed underlying tissues. The superimposition of the glandular and adipose equivalent materials had a severe influence on the detectability of the simulated tumors, particularly with the attenuation-based imaging system. This is an intrinsic problem associated with mammography systems as it provides a 2D image of a 3D object. To tackle this issue, digital breast tomosynthesis (DBT) technique has been developed to provide a set of DBT slices that are reconstructed from low dose limited angle projections to provide better visibility and discrimination of breast tumors by reducing the structured noise caused by the overlapping and superimposition of the breast tissues.

The results of this study are published in reference 125.

Chapter 7. Development of Digital Breast Tomosynthesis using the High-Energy X-ray Inline Phase Sensitive Prototype

7.1 Digital Breast Tomosynthesis

Digital radiology provides post acquisition processing capabilities that are not possible with conventional analog imaging systems. One of the key problem that is associated with the 2D projection imaging is that overlying and underlying anatomy are superimposed on the tumor, often concealing the detection of the cancer and other abnormality. Digital breast tomosynthesis (DBT) has become an important quasi 3D breast imaging method to overcome the breast tissue superposition issues intrinsic to the conventional 2D mammography [126-132]. A typical DBT system is like a digital mammography system; there is an x-ray source and a digital detector whose centers are aligned to each other and the breast is exposed on a support stage near the detector. A device that transforms the mammography system to a tomosynthesis system is the supporting arm that can rotate the x-ray tube around a pivot point over a limited angle in acquiring several low dose angular projection images. Each projection image projects the content in the breast volume with different shits depending on the geometry of the system. In laboratory prototypes and settings, this rotation mechanism is sometimes achieved by employing a rotational stage that can move the imaging phantom to simplify those studies. By employing a limited angle reconstruction algorithm, a set of tomogram slices are reconstructed. Those slices representing the incremental depth within the breast eliminates the superimposed anatomy which can help in the correct diagnosis.

Three widely-used geometries of the DBT image acquisitions are shown in Figure 7.1 [133]. In the isocentric mode, both x-ray source and detector rotate synchronously around a fixed pivot point. In the partial isocentric mode, x-ray source rotates around a pivot point near or on the center of the object under detection, and the detector is stationary and in the parallel path mode, the detector moves in one plane and the x-ray source rotates about a pivotal point.

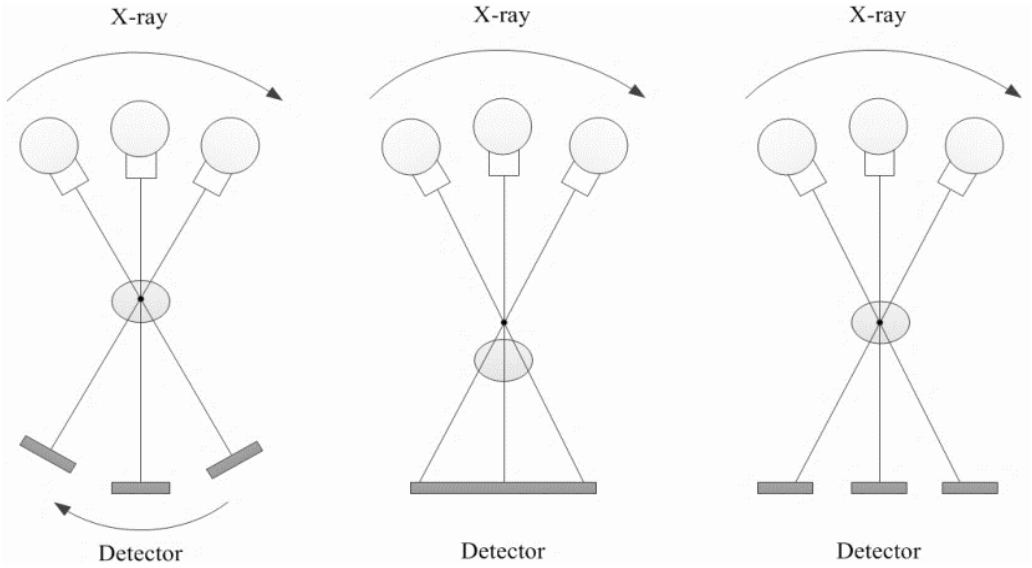

Figure 7.1. Digital breast tomosynthesis geometries: (a) Isocentric mode, (b) Partial Isocentric mode, and (c) Parallel path mode.

The detector that is used in a DBT system must perform the data read-out quickly, produce minimized ghosting, and provide sufficient detective quantum efficiency (DQE) at relatively low dose levels. Many projection images, typically 11 to 51, are acquired over a limited angular range, typically ±7.5 to ±25, in a scan time that ranges from 4 to 20 sec. One of the commercial system, Hologic Selenia Dimensions system, utilizes an amorphous selenium (a-Se) based direct detector that potentially meets the requirement

sufficient DQE at low exposures and acquires 15 images over a range of 15 degrees. Furthermore, that system acquires the projection images in a short period of 4 sec due to the continuous movement of the x-ray source for the acquisition of the projection images. However, the expense in obtaining short image acquisition period is the loss of system spatial resolution, which results from the application of the continuous gantry motion and the pixel binning in the detection process and has a direct negative impact on the detection of the microcalcifications. The recently FDA-approved GE SenoClaire tomosynthesis system employs step-and-shoot tube motion mode without binning, which facilitates the detection of microcalcifications, but the acquisition time for scan is higher as compared to the continuous arm motion.

Several reconstruction techniques [134,135] can be employed (a) shift and add method; (b) filtered back projection; (c) simultaneous algebraic reconstruction techniques; and (d) maximum likelihood algorithms. More sophisticated iterative methods require longer reconstruction times but they provide enhancement by further reducing out-of-plane signals.

7.2 In-line Phase Sensitive Tomosynthesis Prototype Development

The phase sensitive DBT prototype utilizes a micro focus x-ray source, a detector and a rotational stage that provides a tomosynthesis mechanism. The micro focus x-ray source used was Model L8121-01, Hamamatsu Photonics, Japan and the details of the tube are listed in section 3.1.1. In laboratory prototypes and settings, instead of utilizing an amorphous-selenium (a-Se) based direct detectors, CCD-based and CMOS-based indirect flat-panel detectors have been widely used for system characterizations and imaging

studies using small animals, tissues and phantoms [136-137]. They use a scintillator to convert the incident x-ray energy to light photons, which are then converted to electronic signal and read out with a large area integrated circuit with an amorphous silicon (a-Si) photodiode and a thin film transistor (TFT) at each pixel. The thickness of the scintillator may cause additional scattering and, therefore, decrease the imaging spatial resolution, but CCD-based and CMOS-based flat-panel detectors are both able to produce relatively low electronic noise. This research is going to employ the same CMOS flat panel detector (C7942SK-25, Hamamatsu Photonics, Japan) as discussed in Chapter 3 whose scintillating screen is made of structured cesium iodide (CsI) to convert the x-ray photons to light photons. It provides a pixel pitch of 50 μm with an active area of 12 cm × 12 cm and 12-bit digital output.

A device that transforms the mammography system to a tomosynthesis system is the supporting arm that can rotate the x-ray tube around a pivot point over a limited angle in acquiring the angular projections. In laboratory prototypes and settings, this rotation mechanism is sometimes achieved by employing a rotational stage that can move the imaging phantom to simplify those studies. The prototype utilized a motorized rotation stage (Model SGSP-160YAW, OptoSigma) to provide the tomosynthesis mechanism and is shown in Figure 7.2. This rotation stage provides 0.0025°/pulse angular resolution. This means that it takes 400 pulses for the motorized rotation stage to provide 1° of rotation.

Figure 7.2: Motorized rotation stage (Model SGSP-160YAW, OptoSigma).

Once the prototype acquires a number of phase sensitive projections over a limited angular range at a low dose, the reconstruction algorithms reconstructs the DBT slices. The reconstruction algorithm employed in this dissertation research is a modified Feldkamp–Davis–Kress (FDK) back projection algorithm [138-142]. This reconstruction method is a proven powerful reconstruction method for digital tomosynthesis imaging tasks. Several studies have employed a modified FDK reconstruction algorithm for laboratory tomosynthesis prototype characterizations and have demonstrated that this algorithm is able to provide a reconstructed image with high spatial resolution and

contrast, as well as minimal artifacts resulting from the incomplete sampling characteristics due to the nature of tomosynthesis.

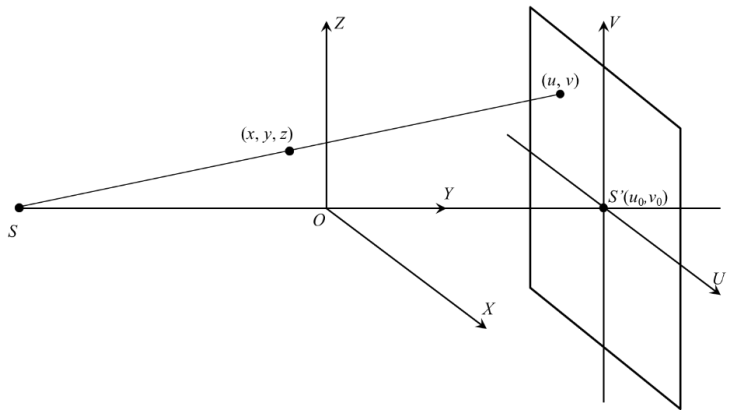

Figure 7.3. Schematic illustrating the geometry of the object space and the detector plane. S, S′ and O represent the x-ray focal spot, the x-ray focal spot mapped on the detector plane and the isocenter of the system.

As illustrated by the tomosynthesis geometry in Figure 7.3, the following formula expresses the algorithm reconstructing a certain slice at depth, y_0, from a set of 2D angular projections, $P(u, v, \theta)$.

$$f(x, y_0, z) = \int_{\min\theta}^{\max\theta} \frac{C(x,y_0,z)\cdot D^2}{(D-s)^2} \int_{-\infty}^{\infty} \frac{D}{\sqrt{D^2+u^2+v^2}} \times P(u, v, \theta) \cdot H\left(\frac{D\cdot t}{D-s} - u\right) du d\theta \qquad (7.1)$$

where $f(x, y_0, z)$ represents the reconstructed image at the given slice with y_0, D is the source-to-isocenter distance or source-to-object distance (SOD, R_1) in the experiments, $H(\cdot)$ represents the one-dimensional Ramp filter along the tube-swept orientation on the detection plane aiming to invert the blurring caused by the sampling and the back projection, $P(u, v, \theta)$ is the projection value of the projection coordinate (u, v) from a projection view θ, and $\mathrm{C}(x, y_0, z)$ is the compensation weighted factor which is experimentally and optimally determined by the following [143]

$$C(x, y_0, z) = 1/\cos[\frac{1.3z}{D-\sqrt{x^2+{y_0}^2+z^2}}) \quad (7.2)$$

7.3 Efficacy of Digital Breast Tomosynthesis

To intrinsically and directly investigate the ability to avoid superimposition of the tissues, a phantom consists of two superimposed fan shape resolution patterns at different depths were utilized. The tomosynthesis slices will be compared with the superimposed bar pattern images. The bench-top prototype consists of the x-ray tube, detector and a digital rotational stage. Two resolution test patterns (Model 02-539, Fluke Corporation, WA, USA) were used for imaging. The two patterns were fixed on the two sides of an 8-mm thick acrylic piece. We intend to investigate the effect of superimposition in the projection and digital tomosynthesis, the two resolution patterns are not precisely aligned with each other. The schematics of the phantom shown in Figure 7.4.

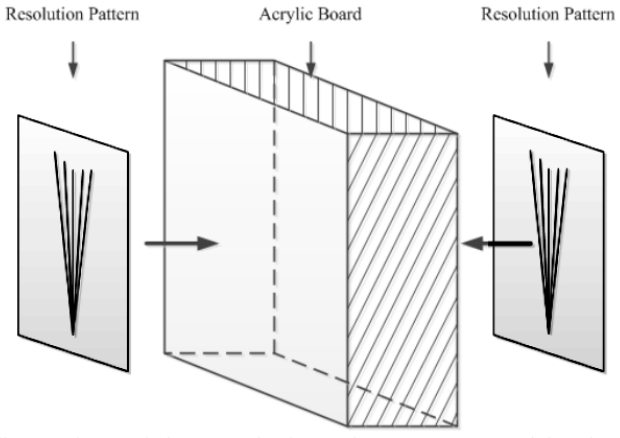

Figure 7.4. Configuration of the phantom where two resolution patterns are imposed with other.

The source-to-object distance (SOD) and the source-to-image distance (SID) were set as 68 cm and 136 cm respectively which makes the geometric magnification (M) to be 2. The phantom is rotated with respect to the rotation center from -8° to +8° with an angle interval of 1°. Thus, a total of 17 projections were acquired over a 16° angular range. Each projection image was acquired using 120 kV, 0.6 mAs. After image acquisition, the tomosynthesis slices are reconstructed using the modified FDK algorithm as mentioned in section 7.2.

7.4 Results and Analysis

The standard projection image of the phantom acquired at 120 kV, 2.7 mAs is shown in figure 7.5. This is the image a radiologist would expect from the phantom in mammography. It is quite clear that the bar lines, and the text on the resolution pattern are superimposed on each other which blur the bar lines heavily, particularly the highresolution bar lines. In particular, for the 1 lp/mm to 2 lp/mm range and 3 lp/mm to 20 lp/mm, the superimposition has a heavy blur in the differentiation of the bar lines as highlighted by the arrows.

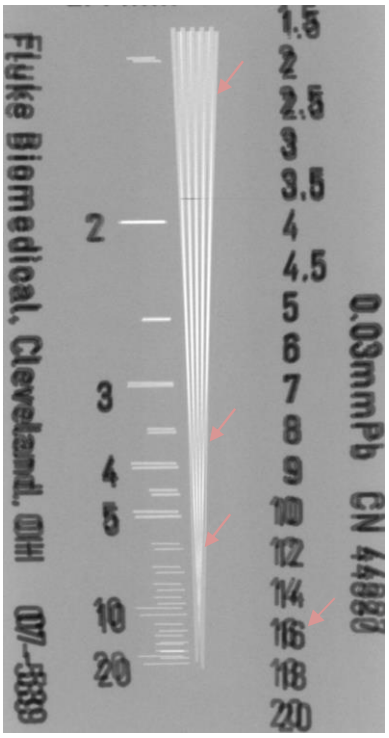

Figure 7.5: Projection image of the phantom of the two superimposed patterns.

Figure 7.6 provides the in-plane reconstructed DT slices of the two superimposed resolution patterns respectively. Figure 7.6 (a) is the front side resolution pattern slice and 7.6 (b) is the back-side resolution pattern slice. From the two reconstructed slices, one can clearly distinguish those bar lines which were heavily blurred in the projection images. From the DT slices, the bar lines from 1-lp/mm to 10-lp/mm are clearly distinguished and resolved. Note that the subtle vertical lines in both the slices are the off-plane artifacts caused by the high contrast bars of the test patterns separated by the thin acrylic plate. Various strategies can be employed to get rid of these off-plane artifacts and the discussion on those strategies is beyond the scope of this study.

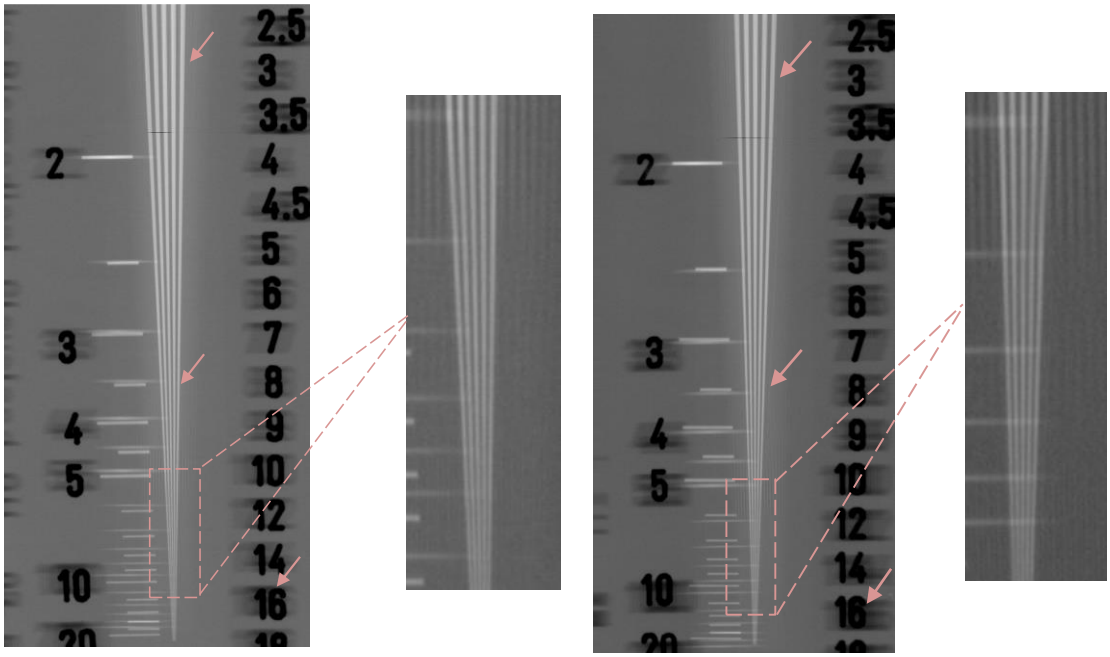

(a) (b)

Figure 7.6. Reconstructed digital tomosynthesis slices of the phantom. (a) Slice showing the front side pattern (b) Slice showing the back-side pattern.

Figure 7.7 shows the contrast profiles corresponding to 3.5 lp/mm bar lines for the projection and DT slices. It is evident that the bar lines in this range are barely resolved in the projection imaging mode due to the super imposition of the two phantoms. The contrast is less than 5%, which clearly is not enough to resolve those bar lines. On the other hand, the contrast for both the front and back slits are greater than 35% in the DT slices and all the bar lines for this resolution are successfully resolved.

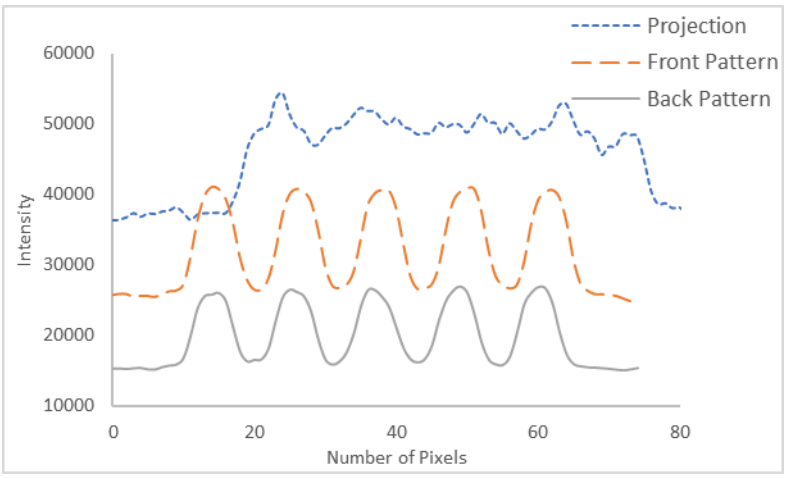

Figure 7.7. Contrast profiles corresponding to 3.5 lp/mm bar lines for the projection image and digital tomosynthesis (DT) slices.

It is important to mention that the spatial resolution in digital tomosynthesis is lower as compared to the projection imaging. In a study conducted on the same prototype [145], multiple low dose projections of an edge phantom were acquired at 40 kV, 500 µA with an angular range of -7.5º to +7.5º and 1.5º step. The source-to-isocenter distance (SOD) and source-to-image distance (SID) were 77 cm and 87 cm. The modulation transfer (MTF) curves from that study as shown in Figure 7.8. It was shown that the cutoff frequencies (10% MTF) was 6 lp/mm in the projection imaging. In the digital tomosynthesis mode, the cutoff frequency was 4.95 lp/mm. This is a drop of approximately 17% in the spatial resolution in digital tomosynthesis. This reduction in the spatial resolution is attributed to the reconstruction algorithm, the limited angular range of the tomographic scan and the z-axis offset.

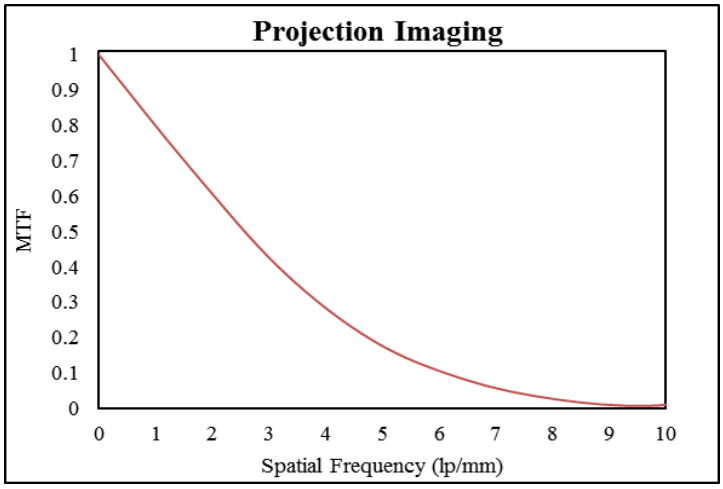

(a)

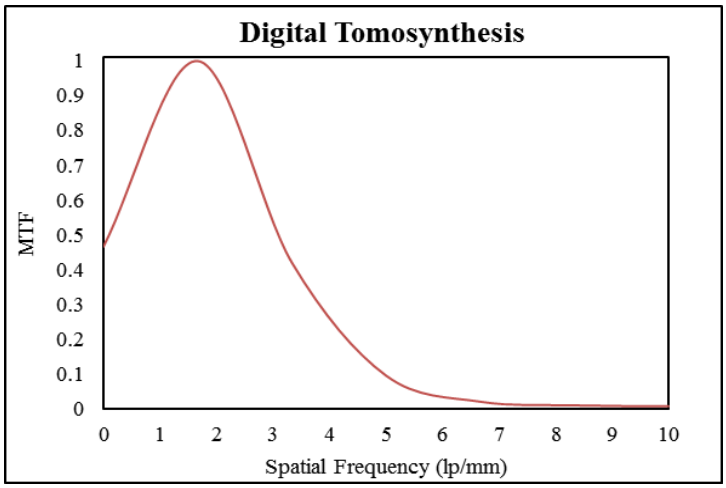

(b)

Figure.7.8. The pre-sampled MTF curves calculated for the (a) Projection imaging mode (b) Digital tomosynthesis mode.

7.5 Discussion

DBT has become an important quasi 3D breast imaging method to overcome the breast tissue superposition issues which is intrinsic to the conventional 2D mammography. To directly investigate the ability to avoid superimposition of the tissues, a phantom consists of two superimposed fan shape resolution patterns at different depths were utilized. It was

quantitatively shown that due to the superimposition, the 2D projection imaging is influenced by blurring heavily which particularly affects the high resolution details. The spatial resolution in tomosynthesis imaging system effectively solve the issue of superimposed structures with relatively low penalties on spatial resolution. This result is critically important in the breast imaging as there is also the superimposition of glandular and adipose tissues on potential tumors which adversely affects the correct diagnosis. In the next chapter, we are going to compare the phase sensitive and attenuation-based DBTs in imaging a heterogenous phantom for the detection of simulated tumors.

This study has been published as references 144 and 145.

Chapter 8. Detectability Comparison of Simulated Tumors in Digital Breast Tomosynthesis using High-Energy X-ray Inline Phase Sensitive and Commercial Imaging Systems

8.1 Introduction

In the previous chapters, it was shown that the 2D mammography has the problem of superimposition of the tissues that limits the detection capability of a system for correctly identifying the disease. Digital tomosynthesis can provide better visibility and discrimination of breast masses by reducing the structured noise caused by the overlapping breast tissues. Just like 2D digital mammography, DBT projection views are sensitive to the attenuation coefficients of breast tissues. For the diagnostic x-ray energy range of 10–100 keV, the contrast difference between a tumor and fibro-glandular tissue is less than 10% because their respective attenuation coefficients are similar. It has been reported that for breast elements such as soft tissue, phase shift coefficients are at least 2-3 orders of magnitude larger than their attenuation coefficients for the diagnostic energy range. Therefore, the variations in soft tissue density give rise to much stronger phase shift induced contrast compared to the attenuation-based contrast.

The objective of this investigation was to compare the detectability of simulated tumors using a high-energy x-ray inline phase sensitive digital breast tomosynthesis prototype and a commercial attenuation-based DBT system. A 5-cm thick modular phantom simulating the appearance of a human breast with 50-50 adipose-glandular percentage density containing contrast-detail (CD) test objects to simulate different tumor sizes was

imaged by each modality. A commercial DBT system that acquired 15 projection views over 15 degrees (15d-15p) was used to acquire the attenuation-based projection views and to reconstruct the conventional tomographic slices. For acquiring phase sensitive projection views, the phase sensitive prototype utilized two acquisition geometries: 11 projection views were acquired over 15 degrees (15d-11p), and 17 projection views were acquired over 16 degrees (16d-17p). A phase retrieval algorithm based on the phase-attenuation duality (PAD) was applied to each projection view, and a modified Feldkamp-Davis-Kress (FDK) algorithm was used to reconstruct the phase sensitive tomographic slices. The overall exposure time utilized to acquire the inline phase sensitive projection views falls within the range of exposure times used by different commercial systems. To the best of our knowledge, a comparison of relative detectability between a clinical DBT system and high-energy phase sensitive DBT imaging has not been presented previously. Furthermore, this comparative study is a step forward for the potential application of phase sensitive imaging to breast tumor detection and diagnosis.

8.2 Methods and Materials

8.2.1 Breast Phantom

We employed a modular phantom comprised of multiple slabs mimicking adipose and glandular breast tissues. The slabs were made of epoxy resins with x-ray attenuation properties similar to 50% adipose-50% glandular density. The adipose and glandular equivalent materials were homogenously blended for uniform background slabs, while heterogeneous blending was used for non-uniform background slabs. Three slabs were sandwiched together to create a 5-cm thick phantom with the middle slab having a thickness of 1 cm and the outer slabs each having a thickness of 2 cm. The front slab facing the x-ray tube had non-uniform background while the middle and the back slabs had uniform backgrounds. To simulate different tumor sizes and densities, the middle slab was machined to include a contrast detail (CD) test pattern. This pattern consisted of a 6×6 matrix of circular discs having diameters of 0.25, 0.5, 1, 2, 3 and 4.25 mm with drilled depths of 0.1, 0.2, 0.4, 0.6, 0.8 and 1 mm.

8.2.2 Phase Sensitive Tomosynthesis Prototype

As shown in Figure 8.1, the system incorporates a micro-focus x-ray source (Model L8121-03, Hamamatsu Photonics, Japan) and a CMOS flat panel detector (C7942SK-25, Hamamatsu Photonics, Japan) with a pixel pitch of 50 μm. The geometric magnification of 2 with SOD = 68 cm and SID = 136 cm was used in this study. A motorized rotational stage (Model SGSP-160YAW, Opto Sigma, USA) was utilized to provide the tomosynthesis mechanism.

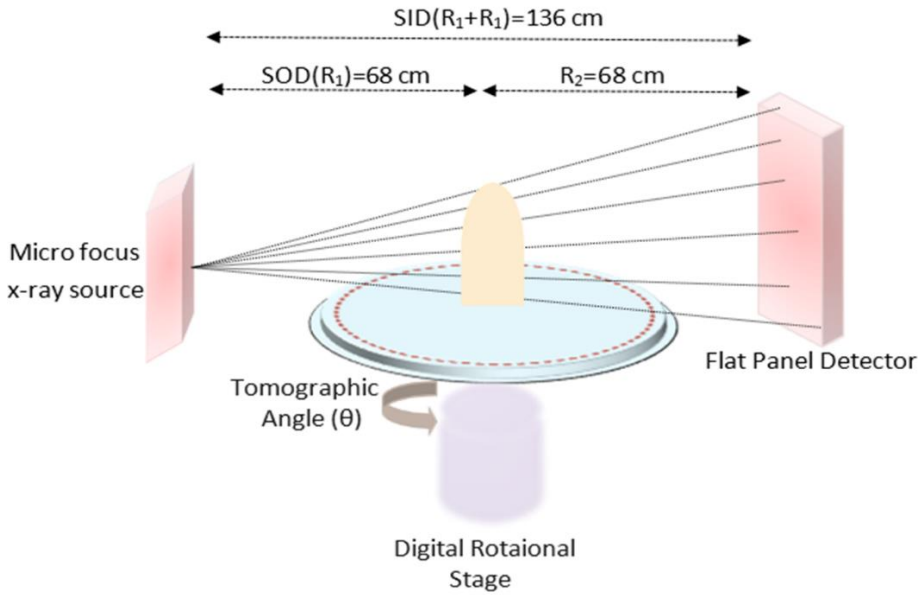

Figure.8.1. Schematic of the inline phase sensitive x-ray imaging prototype used to acquire high-energy phase sensitive projection images.

For experimental imaging, the phantom was placed at the rotational center of the stage, equivalent to the traditional isocentric motion mode, in which both the x-ray source and detector rotate around a fixed pivot point synchronously. The two acquisition geometries utilized in this study are summarized in Table. 8.1. This prototype has been characterized and the details can be found in reference [53].

Table 8.1. Two combinations of tomosynthesis angle and angular increments used to acquire phase sensitive projections for DBT comparisons.

Protocol	Scan Angle (Degrees)	Range (Degrees)	Number of Views	Angular Increments (Degree)	Exposure time per Projection (sec)	Dose (mGy)
15d-11p	15	-7.5, +7.5	11	1.5	0.95	1.5
16d-17p	16	-8, +8	17	1	0.62	1.5

For both angular geometries used to acquire DBT images with the prototype system, the acquisition of angular projection at 0 degrees was possible. All phase sensitive projection views were acquired using a tube voltage of 120 kV, tube current of 500 μA and with a

total exposure time of 10.54 sec (5.27 mAs). A 2.5 mm aluminum (Al) filter was utilized to harden the beam and exclude low-energy photons. The half value layer (HVL) corresponding to these acquisition settings was 4.3 mm Al. All projection views were acquired in a step-and-shoot manner, whereby the rotational stage was stationary during the acquisition of each projection view. The corresponding mean glandular dose (D_g) values utilizing the specified acquisition parameters for the 50-50 phantom imaging was 1.5 mGy with a total entrance exposure (X_E) of 279.8 mR. Phase retrieval process was applied to each projection view. Finally, DBT slices were reconstructed using the modified FDK algorithm that results in an in-plane pixel size of approximately 0.025 mm.

8.2.3 Attenuation-based Tomosynthesis System

A commercial system (Selenia Dimensions 3D, Hologic, Marlborough, USA) was used to acquire the attenuation-based projection images and to reconstruct the conventional tomographic slices. The details of the system can be found in section 5.2.3. The projection views were recorded with an amorphous-selenium (a-Se) flat-panel detector with a matrix array of 4096 × 3328 pixels and a pixel size of 70 μm. The source to image-detector distance (SID) was 70 cm. As shown in Figure 8.2, the system operates with continuous x-ray tube motion, taking 15 projection views over a 15-degree angular span (15d-15p). The distance between detector and center of rotation was 0 mm. All projection views were acquired using an automatic exposure control (AEC) setting at 32 kV, 46 mAs, and 0.7 mm Al filter with X_E = 578 mR, corresponding to a mean glandular dose of 1.6 mGy. The conventional slices reconstructed by the system using a proprietary filtered back projection method, resulting in an in-plane pixel size of approximately 0.1 mm with slice separation of about 1 mm.

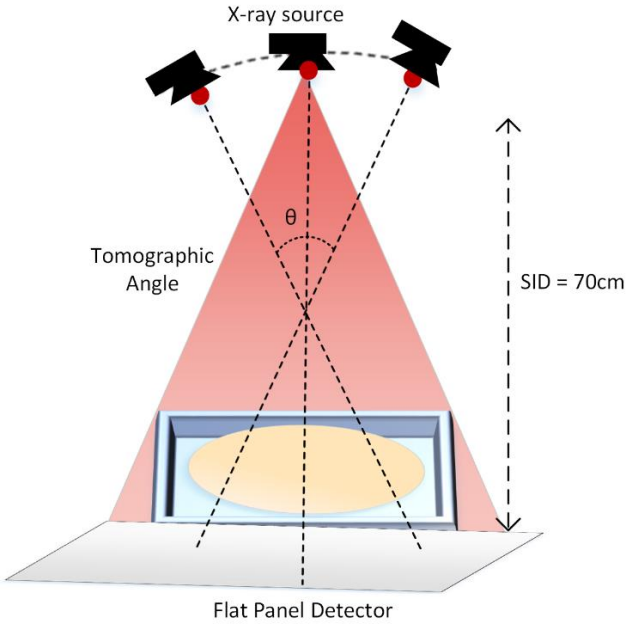

Figure 8.2. Schematic of the commercial DBT system used for the acquisition of low-energy attenuation-based projection images.

The inline phase sensitive acquisition geometry of 15d-11p is similar in angular range, while the 16d-17p geometry is similar in number of projection views to the commercial system's acquisition geometry (15d-15p).

Finally, the simulated x-ray spectra were generated for the two x-ray tubes utilizing the tungsten (W) target as shown in figure 8.3. The spectra were generated according to the method specified in the literature [146]. In the simulations, the input filter was 2.5 mm aluminum (Al) for the 120-kV beam spectrum while it was 0.7 mm Al for 32 kV beam spectrum.

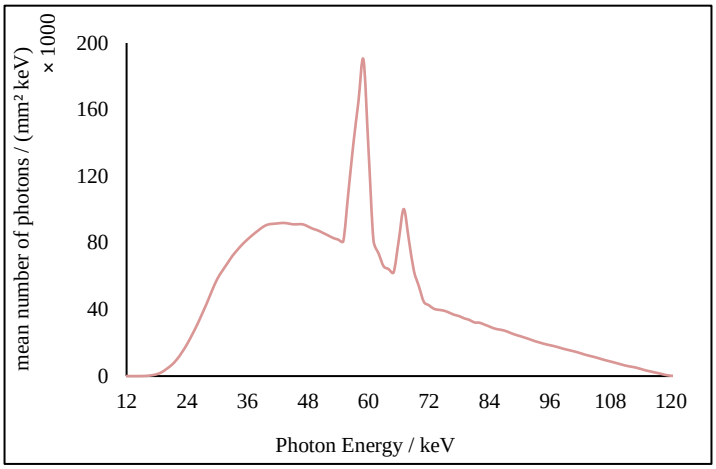

(a)

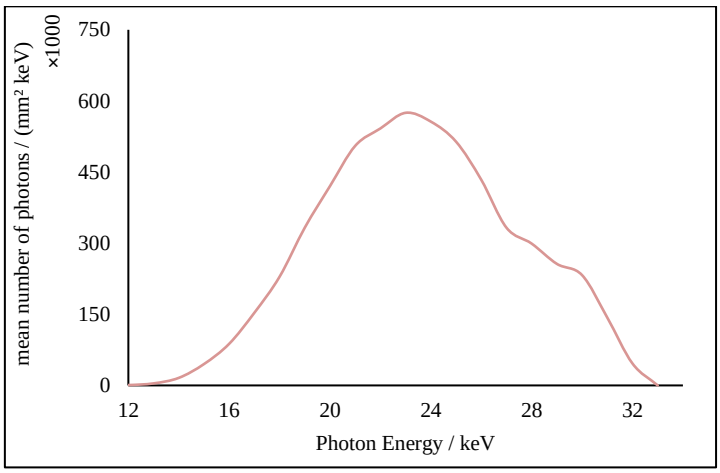

(b)

Figure 8.3. Simulated x-ray spectra for the two x-ray tubes with tungsten target (a) 120 kV, 2.5 mm Al filter as used by the phase sensitive prototype (b) 32 kV, 0.7 mm Al filter as used by the clinical DBT system.

8.2.3 Analyses Methods

The reconstructed in-plane slices containing the CD pattern were cropped to include only rectangular regions of identical size containing the simulated tumors/discs. All images were displayed on a 5 Megapixel LCD monitor (EIZO SMD 21500D, 2048 × 2560, 800:1 contrast ratio, 1024 gray levels, 750 Cd m^{-2} maximum luminance) in a dark room. The monitor was calibrated using the DICOM grayscale standard display function. During the observer study, images were randomly presented to 9 independent observers, each with greater than 5 years of experience in evaluating and grading medical images. The readers were instructed to grade each perceptible disc on 4-point (0 to 3) scale: 3 = disc is completely perceived, including its margins; 2 = disc is perceptible, but without conspicuous margins/circular shape; 1 = greater than half, but not the full disc is perceptible; and, 0 = disc is either not perceptible or less than half is seen. Reading and scoring times were not limited. Threshold contrast and contrast-detail (C-D) curves were generated for each acquisition technique from pooled readers' scores. Contrast-to-noise ratios (CNRs) of the disk targets in each phantom image were calculated to quantitatively compare the imaging systems. Because the CNR for any given disk is influenced by the radiation dose and since the two imaging systems utilized different radiation dose levels, we defined a figure of merit (FOM) to characterize the imaging performance of the conventional DBT and phase contrast modalities.

8.3Results

8.3.1 Observer Study

The projection views of the phantom acquired at 0° angle with low dose using the two imaging systems are given in figure 8.4. The high energy phase sensitive projection views, 8.4(b) and 8.4(c), yield an improved perception of the simulated tumors as compared to the attenuation-based projection view, 8.4(a). In comparison to the phase contrast projection view, 8.4(b), the phase retrieved projection view, 8.4(c), has enhanced bulk contrast for the simulated tumors. Thus, the phase retrieved projection views were used for the DBT slice reconstruction.

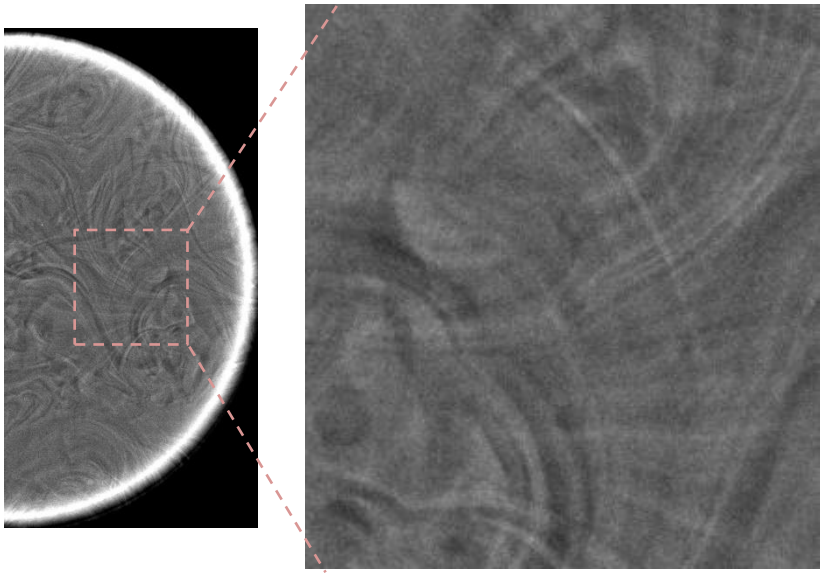

(a)

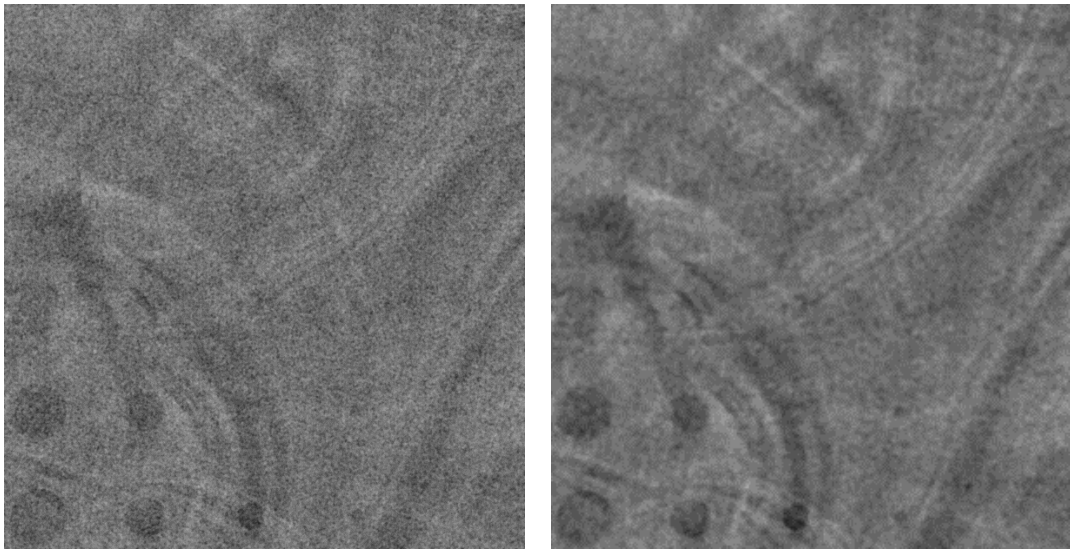

(b) (c)

Figure 8.4: (a) Attenuation-based projection view acquired at 0° with the commercial DBT system at 32 kV, 3.06 mAs and 0.106 mGy (b) Phase contrast projection view acquired at 0° with the phase sensitive prototype at 120 kV, 0.31 mAs and 0.09 mGy (c) Phase retrieved image using PAD algorithm.

Figure 8.5 illustrates a reconstructed DBT in-plane slice depicting the simulated tumor pattern embedded in the modular 50-50 adipose-glandular density phantom acquired with the conventional DBT system using the AEC mode. Of 60 reconstructed tomographic slices, this slice represented the best imaging quality regarding the disc clarity and conspicuity and was cropped to include only the rectangular regions of identical size surrounding the simulated tumors/discs. Apart from window/leveling, no image processing method was applied to this slice used for the observer study.

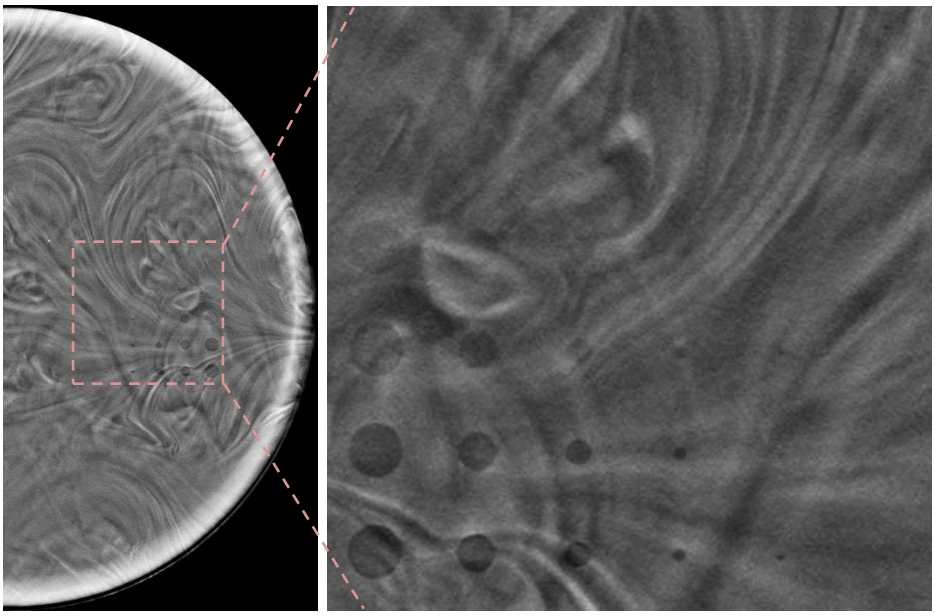

Figure 8.5. In-plane slice containing the simulated tumors, reconstructed from attenuation-based projection images of the phantom acquired with the commercial DBT system at 32 kV, 46 mAs, 1.6 mGy over 15° angular span with 15 projections.

Figure 4 provides the in-plane phase sensitive tomographic slices of the simulated tumors reconstructed from two different angular geometries. Figure 8.6 (a) is the in-plane slice reconstructed from15d-11p geometry and 8.6 (b) is the in-plane slice reconstructed from16d-17p geometry. Due to the limited size of the CMOS detector and the magnification factor utilized, only the CD pattern of the phantom was captured on the image. On these phantom images, the most difficult disks to perceive (smaller with lower contrast) are in the upper right and the easiest disks to perceive (larger with higher contrast) are in the lower left.

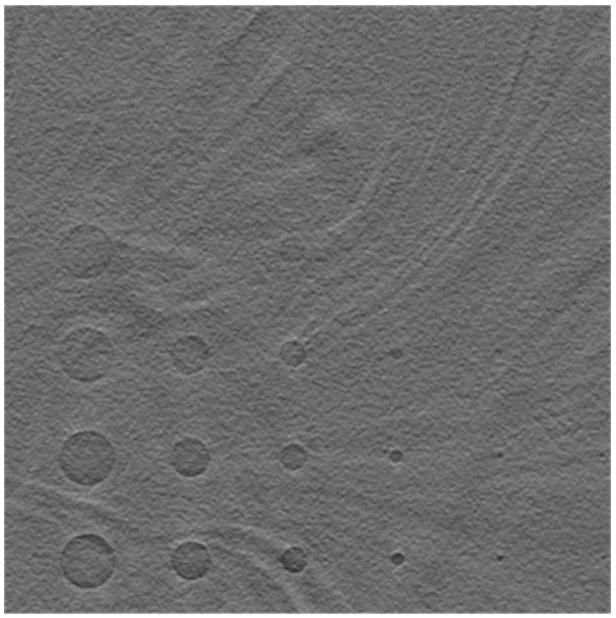

(a)

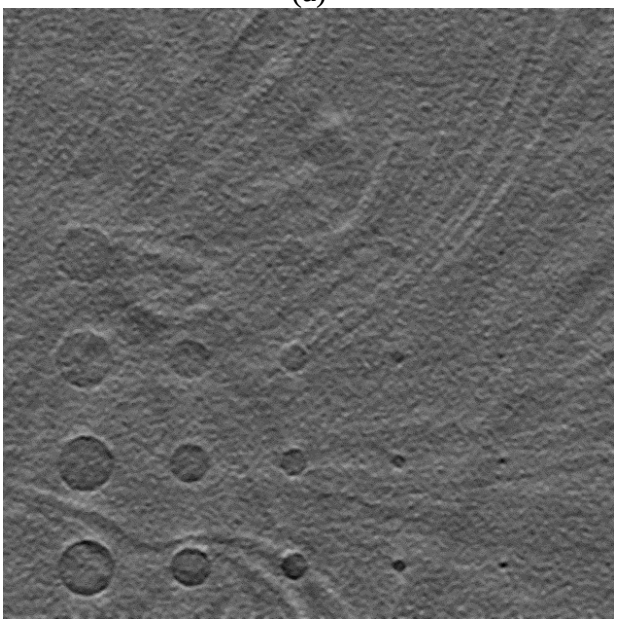

(b)

Figure 8.6. In-plane slices reconstructed from phase sensitive projections of the phantom containing the simulated tumors acquired with the phase sensitive prototype at (a) 120 kV, 500 µA, 5.27 mAs, 1.5 mGy over 15° angular span with 11 projections; (b) 120 kV, 500 µA, 5.27 mAs, 1.5 mGy over 16° angular span with 17 projections.

Figure 8.7 compares the threshold contrast detection performances of the phase sensitive and attenuation-based DBT systems. At similar dose levels, the reconstructed phase sensitive DBT images exhibit superior target perception compared to the attenuation-based DBT image. The C-D curve indicates that observers perceived more simulated 4.25, 2, 0.5 and 0.25 mm diameter tumors on the phase sensitive tomographic slices. Thus, the threshold contrast required for tumor perception for the phase sensitive slices is lower than that of the attenuation-based slice for those diameters. For the two modalities, observers reported similar detection scores for simulated tumors of 3 and 1 mm diameter and thus, the threshold contrasts were identical.

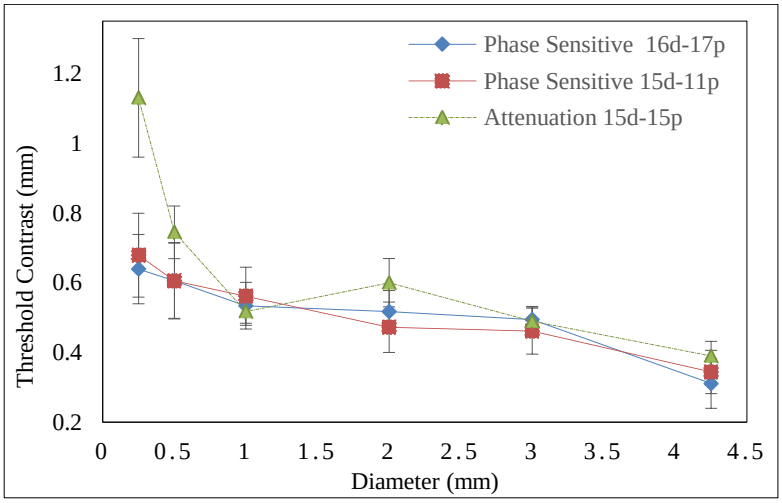

Figure 8.7. Contrast-detail curves for the phase sensitive and attenuation-based tomographic slices for the 50% glandular- 50% adipose phantom.

Figure 8.8 compares the phase contrast (15d-11p) and attenuation-based DBT images and observer scores for 4 tumor discs with different diameters and drilled depths. Our results demonstrated better conspicuity of simulated tumors on phase contrast tomographic slices. For example, for the 2mm, 0.6mm depth tumor disk (Figure 5b), 2 observers reported a score of 3 (fully perceptible round shape with conspicuous margins), 5

observers reported a score of 2 (fully perceptible but not in a circular shape/less conspicuous margins) and 2 observers reported a score of 1 (greater than 50%, but not fully perceptible) with the attenuation-based DBT image; while 6 observers gave a score of 3 and 3 observers gave a score of 2 for the same tumor disk with phase sensitive DBT image.

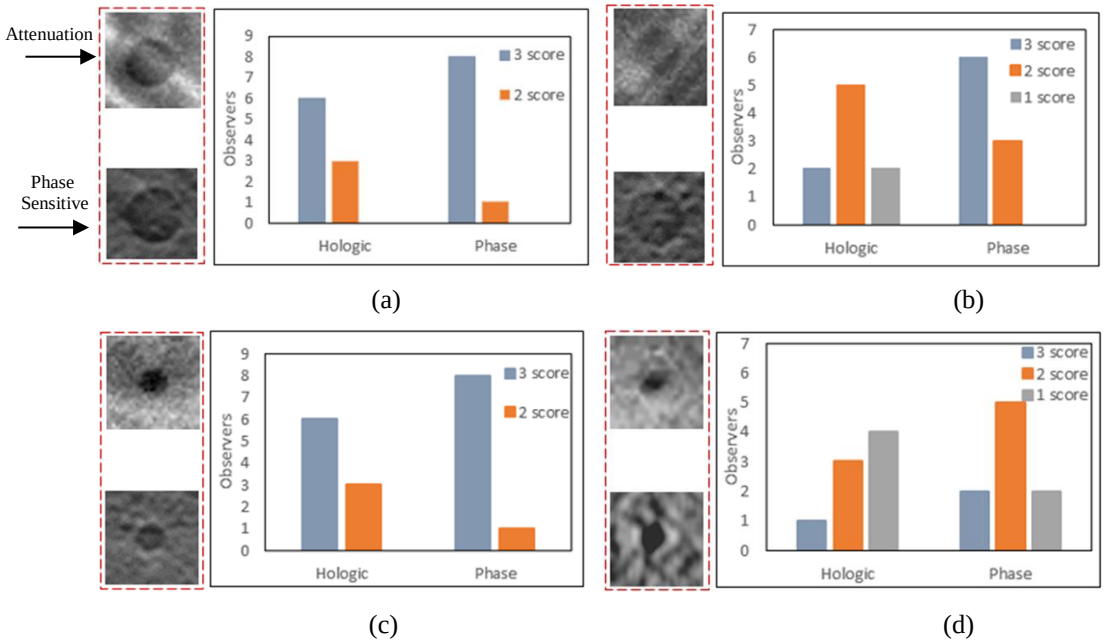

Figure 8.8. Comparison of the observer scores for the simulated tumors extracted from the attenuation-based and the phase sensitive tomographic slices having (a) 2mm diameter, 1mm drilled depth; (b) 2mm diameter, 0.6mm drilled depth; (c) 1mm diameter, 0.8mm drilled depth; and, (d) 0.5mm diameter, 0.6mm drilled depth.

8.3.2 CNR and FOM

The superior performance of the phase sensitive imaging system in our observer study is further supported by the calculated CNR and FOM values. Figure 8.9 provides a graphical comparison of CNR ratios calculated for simulated tumors in the phase sensitive and attenuation-based tomographic slices for several diameters with 1 mm drilled depth. The

phase sensitive slice (16d-17p configuration) has 1.53-3.06 times the CNR as that of the attenuation-based slice. Similarly, for the phase sensitive slice with 15d-11p configuration, the improvement in CNR is 0.71-2.34 times the CNR of the attenuation-based slice.

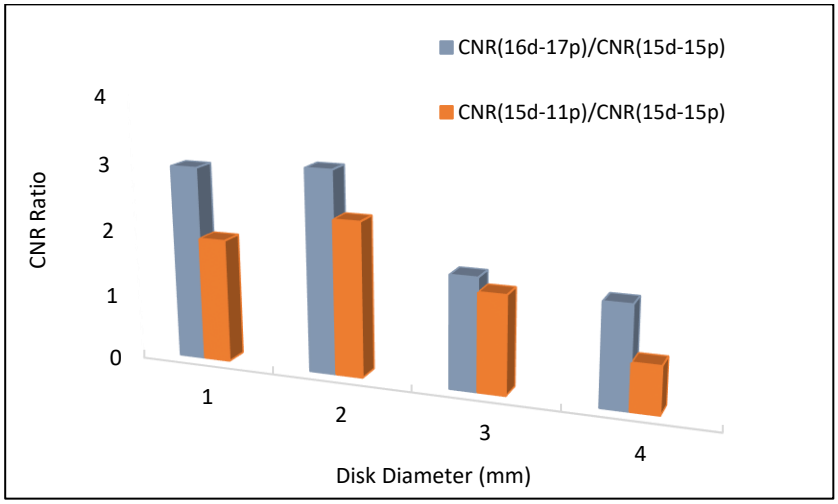

Figure 8.9. Graphical comparison of CNR values for the simulated tumors calculated with phase sensitive and attenuation-based tomographic slices.

The improvement of CNR with the phase sensitive imaging system directly impacts the FOM ratios with the commercial system. From table 8.2, the FOM values of the phase sensitive slice (16d-17p) range from a factor of 2.5-9.97 greater than the FOM values of the attenuation-based slice. Similarly, FOM values for the phase sensitive slice (15d-11p) are 0.54-5.84 greater than the FOM of the attenuation-based slice. Of all the simulated tumor disks, the attenuation-based DBT system had better CNR and FOM values for only the 4.25 mm diameter tumor disk when compared with the phase sensitive system (15d-11p configuration).

Table 8.2. Comparison of the FOM ratios calculated for various disk diameters with 1 mm drilled depth with the phase sensitive and attenuation-based tomographic slices.

	1 mm	2 mm	3 mm	4.25 mm
FOM_{Phase} (16d-17p) / FOM_{Attn} (15d-15p)	9.18	9.97	3.05	2.50
FOM_{Phase} (15d-11p) / FOM_{Attn} (15d-15p)	3.71	5.84	2.33	0.54

8.4. Discussion

This study demonstrates the potential benefits of utilizing a high-energy x-ray phase sensitive system for breast imaging applications. The commercial attenuation-based imaging system operates at low tube voltage (kV) with different filter thickness and SID; hence we cannot apply the same tube current (mA) and exposure time (s) settings as of our phase sensitive prototype. For a fair comparison, we allowed the commercial system to apply its optimized techniques, as determined by its AEC settings. The AEC mode settings resulted in a mean glandular dose value which was slightly higher than the phase sensitive prototype.

From the projection views of the phantom acquired at 0°, it was evident that the high energy phase retrieved images provided better discrimination of the simulated tumors as compared to the low energy attenuation-based projection image. It is widely known that for soft tissue ($Z<10$) and its equivalent materials, attenuation-based imaging at 120 kV would be of inferior contrast due to their attenuation properties. Phase sensitive imaging allows the opportunity to utilize high energy x-rays for imaging soft tissue equivalent materials at low dose levels. With phantom imaging analyses, the phase sensitive DBT imaging prototype demonstrated improved observer ratings, contrast-to-noise ratio

(CNR) and figure of merit (FOM) compared to the commercial system. The SNR improvement provided by the phase sensitive slices was sufficient to detect the smallest discs that were undetectable with the attenuation-based slices, and the C-D curves indicated that the phase sensitive images provided better contrast resolution and spatial resolution. For example, with 4.25 mm tumor disk diameter, the reported threshold contrast was 0.31 versus 0.38 for the phase sensitive (16d-17p) and attenuation-based tomographic slices, indicating improved contrast resolution. Similarly, for smaller disk diameter of 0.25 mm, the reported threshold contrasts of 0.63 and 1.13 for phase sensitive and attenuation-based tomographic slices, respectively, clearly show an improvement in the spatial resolution. With the employment of geometric magnification in clinical radiology, it is well-known that the boundaries of tissues are obscured due to the blurring caused by the finite focal spot size of the x-ray tubes. As a part of its requirement, in-line phase sensitive imaging effectively utilized the geometric magnification with no blurring. The observer rating study indicated better conspicuity of simulated lesion shape and margins with phase-sensitive tomographic slices. For instance, for the tumor disk with 0.25 mm diameter and 0.6 mm drilled depth, 1 observer reported a score of 3, 3 observers reported a score of 2 and 4 observers reported a score of 1 with the attenuation-based slice; while 2 observers reported a score of 3, 5 observers reported a score of 2 and 2 observers reported a score of 1 for the same tumor disk with the phase sensitive slice. It is our general observation that by employing a wider tomosynthesis angle (32d-17p) with phase sensitive imaging, the conspicuity and perception of the shape of the disks improve while the spatial resolution (smaller discs and micro-calcifications) decreases.

While the phase sensitive tomographic slices produced CNR values that were significantly greater than the CNR values as of attenuation-based slices, it was interesting to note that the CNR values decreased as the disk diameter increased. There are several reasons for this result including (a) with the heterogeneous background of the phantom, the variation of pixel values within an ROI increases as the size of an ROI increased, resulting in a large standard deviation value that results in a lower CNR value; (b) the ramp filter accentuates the high-frequency noise, and in the case of limited view tomography, also excessively suppresses the low frequency content, whose impact is clearly distinguishable for large area objects. For detectors with small components of additive noise, where most of the noise results from x-ray quantum fluctuations, the ratio of squared CNR to exposure is essentially independent of the exposure level; thus, the FOM would be expected to be a measure of performance that would not change with the incident exposure. The FOM values calculated for the phase sensitive slices, (16d-17p) and (15d-11p), are 2.5-9.97 and 0.54-5.84 times the FOM of the attenuation-based slice.

The two-phase sensitive DBT geometries that we evaluated utilized about the same tomosynthesis angle but with different numbers of equally spaced projections. Our observers preferred the slices reconstructed with a larger number of projections, 16d-17p. For a fixed tomosynthesis angle, one may utilize a greater number of projections for refined angular sampling, but there are few limiting factors: (a) for a fixed mean glandular dose, each additional low dose projection introduces additional electronic noise from the detector, which increases the overall noise of the reconstructed volume and (b) the total scan time generally increases with the number of projections, particularly in a step-and-shoot configuration, which may increase motion artifacts.

We plan to use complex breast imaging phantoms with various testing objects in different planes of the phantom to further highlight the benefits of utilizing inline phase sensitive DBT imaging as it provides improved depth resolution in comparison to the attenuation-based DBT imaging [60]. To our best knowledge, 10.5 sec is the shortest reported exposure time for successful inline phase sensitive DBT imaging outperforming a commercial DBT system regarding target detection and CNRs. Furthermore, this exposure time falls within the range of exposure times used by commercial systems.

The results of this study are published in reference [147].

Chapter 9. Conclusions

9.1 Summary

The research presented in this dissertation demonstrates the feasibility of a high-energy in-line phase contrast x-ray imaging system for potential clinical applications. The ability of the inline phase contrast x-ray imaging system has been shown for digital mammography and digital breast tomosynthesis applications in comparison to the attenuation-based clinical imaging systems at similar or reduced glandular dose (D_g) levels. We assessed the glandular dose levels for the absorbed dose to breast tissue, the stochastic health risk such as cancer of high energy x-ray photons can be further assessed by using the equivalent dose (H_T). It is defined by the International Commission on Radiological Protection (ICRP) as the product of the absorbed tissue dose (D_T) and a weighting factor (W_R) which is related to the radiation quality. For the photon radiation like x-rays and gamma rays, the weighting factor has the value 1 independent of the energy of the radiation. Hence, the high-energy phase contrast technique does not present any higher stochastic health risk than conventional low-energy mammography technique, as compared on equal glandular dose basis.

Chapter 2 introduced the theory behind the inline phase contrast imaging. To obtain phase information, a propagation distance between the object and the detector is needed to allow the development of interferences of the sub waves. The overall image intensity contrast comes from both phase and attenuation. With the theory and guidelines established, a numerical method for retrieving the quantitative phase map from the phase contrast images was introduced. This phase retrieval method was based on the phase-attenuation

duality and requires only one phase sensitive projection image with some special requirements that were discussed. From the extracted phase map, one can derive a map of the object's projected electron densities. The electron density is an intrinsic attribute of the object, and hence the electron density map yields a quantitative image of the object's structure.

In Chapter 3, the optimal in-line phase-sensitive geometry and high energy settings under the experimental conditions were investigated and compared with the computer simulations. As compared to the other geometric magnifications (M), the image quality and target discrimination are highest for M = 2.5 under the same glandular dose (D_g). The computer simulations based on the modulus of relative phase-contrast factor $|RPF\ (u)|$ also validated the experimental results. The phase retrieved images had improved performance and detectability as compared to the phase contrast images. Both the 100 kV and 120 kV resulted in similar results and image performances in terms of the image contrast and observer scores.

In Chapter 4, the characterization of an innovative hybrid micro focus x-ray tube was performed. Micro focus x-ray source is an important component of the inline phase sensitive imaging prototype and it was necessary to characterize the performance of this hybrid tube in both continuous and pulsed emission modes. The measured focal spot sizes vary linearly with respect to the output power and match the manufacturer provided data. The focal spot sizes in the vertical direction were smaller than the horizontal direction, which was visible when comparing the spatial resolution of the MTF curves. For both the continuous emission and pulsed emission modes, the characteristic peaks of the anode

target in the spectrum were easily differentiated. The unfiltered x-ray beam in both emission modes contained a large amount of low energy photons which were readily blocked by an aluminum (Al) filter of small thickness. This implied that these low energy photons didn't contribute in the image formation and will instead be readily absorbed by the tissue/organ, adding unnecessary radiation dose. Therefore, for all the kV values, it was recommended to use a certain amount of filtration to block those unwanted low energy photons.

After identifying the optimal geometric and operating conditions for the high energy inline phase sensitive imaging prototype in Chapter 3, its comparison with the clinical imaging units in imaging homogenous breast phantoms with varying glandular-adipose tissue ratios was the next step in Chapter 5. Two state of the art commercial clinical imaging systems were utilized that are routinely used for breast cancer screening in the U.S. For the 50% G – 50% A density phantom, the observer study, contrast-to-noise ratio (CNR) and figure of merit (FOM) comparisons all indicated a large CNR improvement with the phase retrieved image as compared to the two commercial imaging systems acquired under their AEC modes at similar dose levels. The clinical systems had to increase the dose to provide adequate image quality for the denser phantom. With our prototype, we were able to maintain the image quality enhancement without increasing the dose to the denser 70% G – 30% A density phantom. Therefore, the comparison of 70G-30A phantom was more significant, since the phase sensitive images were acquired at a reduced relative dose as compared to the attenuation-based images acquired by clinical images, yet still provided a noticeable image quality enhancement regarding the disks perception, CNR and FOM values.

Having shown in its effectiveness in imaging the standard homogenous breast phantoms that are routinely used for quality assurance purposes in the clinical world, Chapter 6 demonstrated the efficacy of the inline phase sensitive imaging prototype in imaging breast equivalent phantoms with heterogenous backgrounds. The CNR improvement of the phase sensitive images was enough to detect the smaller discs simulated tumors that were undetectable by the commercial imaging system. The simulated tumors were more perceptible on the phase sensitive image in the superimposed underlying tissues. The superimposition of the glandular and adipose equivalent materials had a severe influence on the detectability of the simulated tumors, particularly with the attenuation-based imaging system.

Having seen the superimposition of tissues which limits the detectability of potential tumors in the 2D digital mammography, the feasibility of a digital tomosynthesis was introduced in Chapter 7. With the phantom study, it was quantitatively shown that the 2D imaging is heavily influenced by blurring due to the superimposition of the bar patterns. That blurring particularly affected the high resolution details. The spatial resolution in tomosynthesis imaging system effectively solve the issue of superimposed structures with relatively low penalties on spatial resolution. This result is critically important in the breast imaging as there is also the superimposition of glandular and adipose tissues on potential tumors which adversly affects the correct diagnosis.

Finally, the investigation presented in Chapter 8 extended the research of Chapter 6, in which the detectability of simulated tumors in a heterogenous phantom was compared using the high-energy x-ray inline phase sensitive digital breast tomosynthesis (DBT)

prototype and a commercial state of the art attenuation-based DBT system. From the projection views of the phantom acquired at 0°, it was evident that the high energy phase sensitive images provided better discrimination of the simulated tumors as compared to the low energy attenuation-based projection image. Phase sensitive DBT slices reconstructed in two acquisition geometries demonstrated improved observer ratings, contrast-to-noise ratio (CNR) and figure of merit (FOM) compared to the commercial system. The SNR improvement provided by the phase sensitive slices was sufficient to detect the smallest discs that were undetectable with the attenuation-based slices, and the C-D curves indicated that the phase sensitive images provided better contrast resolution and spatial resolution. With the employment of geometric magnification in clinical radiology, it is well-known that the boundaries of tissues are obscured due to the blurring caused by the finite focal spot size of the x-ray tubes. As a part of its requirement, in-line phase sensitive imaging effectively utilized the geometric magnification with no blurring. The observer rating study indicated better conspicuity of simulated lesion shape and margins with phase-sensitive tomographic slices.

9.2 Future Research Direction

The investigation presented in this dissertation further encourage and warrants future research not towards the further development and optimization of the innovative high energy inline phase sensitive prototype in improving x-ray image detectability and specificity.

An existing challenge for the current micro focus x-ray tubes is their limited output which consequently limits the short acquisition time. One key reason is that the anode target of

these tubes is solid that generates x-ray output at tens to several hundred micro amperes current. The surface temperature of the anode target must be well below its melting point to avoid its damage and maintain its life time. Therefore, the range of current is much lower than the operating tube current for commercial imaging systems. Future studies on the feasibility of the inline phase sensitive imaging with liquid metal jet x-ray tubes and carbon nanotubes (CNT) are needed to further shorten the exposure time needed for a scan. In liquid metal jet x-ray tubes, the anode target is itself molten and regenerative in nature. Thus, the limitation to maintain the target well below its melting point is removed and it achieve high brightness at micron spot sizes. In traditional thermionic based x-ray technology, a tube with an electron emitter, typically made of tungsten filament, at one end and a metal anode at the other end. When the filament is heated to a very temperature, it emits electrons that are accelerated towards the anode target to create x-rays. Instead of utilizing a single emitter, CNT tubes utilize an array of nanotubes which serve as hundreds of tiny electron guns and the nanotubes emit electrons efficiently without heating and thus enabling many closely spaced nanotubes to generate x-rays in a single tube.

It is important to mention that the detector quantum efficiency (DQE) itself decreases as the x-ray energy increase, as do the attenuation and phase coefficients of tissue. Subsequently, the use of a high energy x-ray beam is inherently disadvantageous for phase sensitive imaging in a comparison study with low energy attenuation-based clinical images. However, due to the limited output power of the micro focus x-ray tubes, a high energy x-ray beam is required for phase imaging to reduce the exposure times to clinically acceptable values. Therefore, an investigation on the employment of detectors that have

high quantum efficiency at higher x-ray energies would further benefit future studies in high energy phase sensitive imaging.

The reconstruction algorithm used for phase sensitive DBT slices was not fully optimized and suffers from imperfections like streaking and other noise-like artifacts which may obscure anatomical features. By employing optimization filters, such as spectrum apodization and slice thickness filters, the sensitivity of phase sensitive DBT imaging technique will further increase just like in the phase sensitive projection imaging.

References

1. Siegel RL, Miller KD, Jemal A. Cancer statistics, 2016. CA: a cancer journal for clinicians. 2016 Jan 1;66(1):7-30.
2. DeSantis CE, Fedewa SA, Goding Sauer A, Kramer JL, Smith RA, Jemal A. Breast cancer statistics, 2015: Convergence of incidence rates between black and white women. CA: a cancer journal for clinicians. 2016 Jan 1;66(1):31-42.
3. http://www.breastcancer.org/symptoms/understand_bc/statistics
4. Early Breast Cancer Trialists' Collaborative Group. Effects of chemotherapy and hormonal therapy for early breast cancer on recurrence and 15-year survival: an overview of the randomised trials. The Lancet. 2005 May 20;365(9472):1687-717.
5. Lyman GH, Giuliano AE, Somerfield MR, Benson III AB, Bodurka DC, Burstein HJ, Cochran AJ, Cody III HS, Edge SB, Galper S, Hayman JA. American Society of Clinical Oncology guideline recommendations for sentinel lymph node biopsy in early-stage breast cancer. Journal of clinical oncology. 2005 Oct 20;23(30):7703-20.
6. Gnant M, Mlineritsch B, Stoeger H, Luschin-Ebengreuth G, Heck D, Menzel C, Jakesz R, Seifert M, Hubalek M, Pristauz G, Bauernhofer T. Adjuvant endocrine therapy plus zoledronic acid in premenopausal women with early-stage breast cancer: 62-month follow-up from the ABCSG-12 randomised trial. The lancet oncology. 2011 Jul 31;12(7):631-41.
7. Houssami N, Macaskill P, Marinovich ML, Dixon JM, Irwig L, Brennan ME, Solin LJ. Meta-analysis of the impact of surgical margins on local recurrence in

women with early-stage invasive breast cancer treated with breast-conserving therapy. European Journal of Cancer. 2010 Dec 31;46(18):3219-32.

8. Heath M, Bowyer K, Kopans D, Kegelmeyer Jr P, Moore R, Chang K, Munishkumaran S. Current status of the digital database for screening mammography. InDigital mammography 1998 (pp. 457-460). Springer Netherlands.
9. Dromain C, Balleyguier C. Contrast-enhanced digital mammography. InDigital mammography 2010 (pp. 187-198). Springer Berlin Heidelberg.
10. Pisano ED, Hendrick RE, Yaffe MJ, Baum JK, Acharyya S, Cormack JB, Hanna LA, Conant EF, Fajardo LL, Bassett LW, D'Orsi CJ. Diagnostic accuracy of digital versus film mammography: exploratory analysis of selected population subgroups in DMIST. Radiology. 2008 Feb;246(2):376-83.
11. Lewin JM, D'Orsi CJ, Hendrick RE, Moss LJ, Isaacs PK, Karellas A, Cutter GR. Clinical comparison of full-field digital mammography and screen-film mammography for detection of breast cancer. American Journal of Roentgenology. 2002 Sep;179(3):671-7.
12. Jong RA, Yaffe MJ, Skarpathiotakis M, Shumak RS, Danjoux NM, Gunesekara A, Plewes DB. Contrast-enhanced digital mammography: initial clinical experience. Radiology. 2003 Sep;228(3):842-50.
13. US Preventive Services Task Force. Screening for breast cancer: US Preventive Services Task Force recommendation statement. Annals of internal medicine. 2009 Nov 17;151(10):716.

14. Pisano ED, Yaffe MJ, Hemminger BM, Hendrick RE, Niklason LT, Maidment AD, Kimme-Smith CM, Feig SA, Sickles EA, Braeuning MP. Current status of full-field digital mammography. Academic radiology. 2000 Apr 1;7(4):266-80.
15. Dershaw DD. Status of mammography after the digital mammography imaging screening trial: digital versus film. The breast journal. 2006 Mar 1;12(2):99-102.
16. Dobbins III JT, Godfrey DJ. Digital x-ray tomosynthesis: current state of the art and clinical potential. Physics in medicine and biology. 2003 Sep 16;48(19):R65.
17. Niklason LT, Christian BT, Niklason LE, Kopans DB, Castleberry DE, Opsahl-Ong BH, Landberg CE, Slanetz PJ, Giardino AA, Moore R, Albagli D. Digital tomosynthesis in breast imaging. Radiology. 1997 Nov;205(2):399-406.
18. Skaane P, Bandos AI, Gullien R, Eben EB, Ekseth U, Haakenaasen U, Izadi M, Jebsen IN, Jahr G, Krager M, Niklason LT. Comparison of digital mammography alone and digital mammography plus tomosynthesis in a population-based screening program. Radiology. 2013 Apr;267(1):47-56.
19. Friedewald SM, Rafferty EA, Rose SL, Durand MA, Plecha DM, Greenberg JS, Hayes MK, Copit DS, Carlson KL, Cink TM, Barke LD. Breast cancer screening using tomosynthesis in combination with digital mammography. Jama. 2014 Jun 25;311(24):2499-507.
20. Sechopoulos I, Ghetti C. Optimization of the acquisition geometry in digital tomosynthesis of the breast. Medical physics. 2009 Apr 1;36(4):1199-207.
21. Alakhras M, Bourne R, Rickard M, Ng KH, Pietrzyk M, Brennan PC. Digital tomosynthesis: a new future for breast imaging?. Clinical radiology. 2013 May 31;68(5):e225-36.

22. Bushberg JT, Boone JM. The essential physics of medical imaging. Lippincott Williams & Wilkins; 2011 Dec 20.
23. Kotre CJ, Birch IP. Phase contrast enhancement of x-ray mammography: a design study. Physics in medicine and biology. 1999 Nov;44(11):2853.
24. Law J. The development of mammography. Physics in medicine and biology. 2006 Jun 20;51(13):R155.
25. Wilkins SW, Gureyev TE, Gao D, Pogany A, Stevenson AW. Phase-contrast imaging using polychromatic hard X-rays. Nature. 1996 Nov 28;384(6607):335.
26. Snigirev A, Snigireva I, Kohn V, Kuznetsov S, Schelokov I. On the possibilities of x-ray phase contrast microimaging by coherent high-energy synchrotron radiation. Review of scientific instruments. 1995 Dec;66(12):5486-92.
27. Arfelli F, Assante M, Bonvicini V, Bravin A, Cantatore G, Castelli E, Dalla Palma L, Di Michiel M, Longo R, Olivo A, Pani S. Low-dose phase contrast x-ray medical imaging. Physics in medicine and biology. 1998 Oct;43(10):2845.
28. Pogany A, Gao D, Wilkins SW. Contrast and resolution in imaging with a microfocus x-ray source. Review of Scientific Instruments. 1997 Jul;68(7):2774-82.
29. Gureyev TE, Wilkins SW. On x-ray phase imaging with a point source. JOSA A. 1998 Mar 1;15(3):579-85.
30. Momose A, Fukuda J. Phase-contrast radiographs of nonstained rat cerebellar specimen. Medical physics. 1995 Apr 1;22(4):375-9.
31. Lewis RA. Medical phase contrast x-ray imaging: current status and future prospects. Physics in medicine and biology. 2004 Aug 2;49(16):3573.

32. X. Wu, A. Dean, and H. Liu, ‘‘X-ray diagnostic techniques,’’ in Biomedical Photonics Handbook, edited by T. VoDinh ~CRC, Tampa, FL, (2003), Chap. 26, pp. 26-1–.26-34.
33. Bravin A, Coan P, Suortti P. X-ray phase-contrast imaging: from pre-clinical applications towards clinics. Physics in medicine and biology. 2012 Dec 10;58(1):R1.
34. Wu X, Liu H. Clarification of aspects in in-line phase-sensitive x-ray imaging. Medical Physics. 2007 Feb 1;34(2):737-43.
35. Oliva P, Carpinelli M, Golosio B, Delogu P, Endrizzi M, Park J, Pogorelsky I, Yakimenko V, Williams O, Rosenzweig J. Quantitative evaluation of single-shot inline phase contrast imaging using an inverse compton x-ray source. Applied Physics Letters. 2010 Sep 27;97(13):134104.
36. Gureyev TE, Mayo SC, Myers DE, Nesterets Y, Paganin DM, Pogany A, Stevenson AW, Wilkins SW. Refracting Röntgen’s rays: propagation-based x-ray phase contrast for biomedical imaging. Journal of Applied Physics. 2009 May 15;105(10):102005.
37. Momose A. Recent advances in X-ray phase imaging. Japanese Journal of Applied Physics. 2005 Sep 8;44(9R):6355.
38. Donnelly EF, Price RR, Pickens DR. Quantification of the effect of system and object parameters on edge enhancement in phase-contrast radiography. Medical physics. 2003 Nov 1; 30(11):2888-96.

39. Ren L, Zhou Z, Ghani MU, Li Y, Liu H. Method for determining the modulation transfer function of X-ray fluorescence mapping system. Optics Express. 2014 Sep 8;22(18):21199-213.
40. Castelli E, Tonutti M, Arfelli F, Longo R, Quaia E, Rigon L, Sanabor D, Zanconati F, Dreossi D, Abrami A, Quai E. Mammography with synchrotron radiation: first clinical experience with phase-detection technique. Radiology. 2011 Jun;259(3):684-94.
41. Longo R, Arfelli F, Bellazzini R, Bottigli U, Brez A, Brun F, Brunetti A, Delogu P, Di Lillo F, Dreossi D, Fanti V. Towards breast tomography with synchrotron radiation at Elettra: first images. Physics in medicine and biology. 2016 Feb 2;61(4):1634.
42. Gonzalez-Tendero A, Zhang C, Balicevic V, Cárdenes R, Loncaric S, Butakoff C, Paun B, Bonnin A, Garcia-Cañadilla P, Muñoz-Moreno E, Gratacós E. Whole heart detailed and quantitative anatomy, myofibre structure and vasculature from X-ray phase-contrast synchrotron radiation-based micro computed tomography. European Heart Journal-Cardiovascular Imaging. 2017 Mar 15:jew314.
43. Diemoz PC, Bravin A, Sztrókay-Gaul A, Ruat M, Grandl S, Mayr D, Auweter S, Mittone A, Brun E, Ponchut C, Reiser MF. A method for high-energy, low-dose mammography using edge illumination x-ray phase-contrast imaging. Physics in medicine and biology. 2016 Nov 28;61(24):8750.
44. Quai E, Longo R, Zanconati F, Jaconelli G, Tonutti M, Abrami A, Arfelli F, Dreossi D, Tromba G, Cova MA. First application of computed radiology to

mammography with synchrotron radiation. La radiologia medica. 2013 Feb 1;118(1):89-100.

45. Zhang D, Donovan M, Fajardo LL, Archer A, Wu X, Liu H. Preliminary feasibility study of an in-line phase contrast x-ray imaging prototype. IEEE Transactions on Biomedical Engineering. 2008 Sep;55(9):2249-57.
46. Tapfer A, Bech M, Velroyen A, Meiser J, Mohr J, Walter M, Schulz J, Pauwels B, Bruyndonckx P, Liu X, Sasov A. Experimental results from a preclinical X-ray phase-contrast CT scanner. Proceedings of the National Academy of Sciences. 2012 Sep 25;109(39):15691-6.
47. Donnelly EF, Lewis KG, Wolske KM, Pickens DR, Price RR. Characterization of the phase-contrast radiography edge-enhancement effect in a cabinet x-ray system. Physics in medicine and biology. 2005 Dec 14;51(1):21.
48. Matsuo S, Katafuchi T, Tohyama K, Morishita J, Yamada K, Fujita H. Evaluation of edge effect due to phase contrast imaging for mammography. Medical physics. 2005 Aug 1;32(8):2690-7.
49. Zhao Y, Brun E, Coan P, Huang Z, Sztrókay A, Diemoz PC, Liebhardt S, Mittone A, Gasilov S, Miao J, Bravin A. High-resolution, low-dose phase contrast X-ray tomography for 3D diagnosis of human breast cancers. Proceedings of the National Academy of Sciences. 2012 Nov 6;109(45):18290-4.
50. Zhu P, Zhang K, Wang Z, Liu Y, Liu X, Wu Z, McDonald SA, Marone F, Stampanoni M. Low-dose, simple, and fast grating-based X-ray phase-contrast imaging. Proceedings of the National Academy of Sciences. 2010 Aug 3;107(31):13576-81.

51. Sztrókay A, Diemoz PC, Schlossbauer T, Brun E, Bamberg F, Mayr D, Reiser MF, Bravin A, Coan P. High-resolution breast tomography at high energy: a feasibility study of phase contrast imaging on a whole breast. Physics in medicine and biology. 2012 Apr 20;57(10):2931.
52. Wong MD, Yan A, Ghani M, Li Y, Fajardo L, Wu X, Liu H. Dose and detectability improvements with high energy phase sensitive x-ray imaging in comparison to low energy conventional imaging. Physics in medicine and biology. 2014 Apr 15;59(9):N37.
53. Wu D, Yan A, Li Y, Wong MD, Zheng B, Wu X, Liu H. Characterization of a high-energy in-line phase contrast tomosynthesis prototype. Medical physics. 2015 May 1;42(5):2404-20.
54. Ghani MU, Wong MD, Wu D, Zheng B, Chen W, Fajardo LL, Wu X, Liu H. Detectability comparison of simulated objects within a dense breast phantom using high energy x-ray phase sensitive and conventional imaging systems. In SPIE BiOS 2017 Feb 20 (pp. 100650K-100650K). International Society for Optics and Photonics.
55. Hauser N, Wang Z, Kubik-Huch RA, Trippel M, Singer G, Hohl MK, Roessl E, Köhler T, van Stevendaal U, Wieberneit N, Stampanoni M. A study on mastectomy samples to evaluate breast imaging quality and potential clinical relevance of differential phase contrast mammography. Investigative radiology. 2014 Mar 1;49(3):131-7.

56. Bech M, Tapfer A, Velroyen A, Yaroshenko A, Pauwels B, Hostens J, Bruyndonckx P, Sasov A, Pfeiffer F. In-vivo dark-field and phase-contrast x-ray imaging. Scientific reports. 2013 Nov 13;3:3209.
57. Schleede S, Bech M, Grandl S, Sztrókay A, Herzen J, Mayr D, Stockmar M, Potdevin G, Zanette I, Rack A, Weitkamp T. X-ray phase-contrast tomosynthesis for improved breast tissue discrimination. European journal of radiology. 2014 Mar 31;83(3):531-6.
58. Hammonds JC, Price RR, Donnelly EF, Pickens DR. Phase-contrast digital tomosynthesis. Medical physics. 2011 May 1;38(5):2353-8.
59. Szafraniec MB, Millard TP, Ignatyev K, Speller RD, Olivo A. Proof-of-concept demonstration of edge-illumination x-ray phase contrast imaging combined with tomosynthesis. Physics in medicine and biology. 2014 Feb 20;59(5):N1.
60. Guan H, Xu Q, Garson A, Anastasio MA. Depth resolution properties of in-line X-ray phase-contrast tomosynthesis. InProc SPIE 2014 Mar 19 (Vol. 9033, p. 90330H).
61. Fitzgerald R. Phase-sensitive x-ray imaging. Phys. Today. 2000 Jul 1;53(7):23-6.
62. Ingal VN, Beliaevskaya EA. X-ray plane-wave topography observation of the phase contrast from a non-crystalline object. Journal of Physics D: Applied Physics. 1995 Nov 14;28(11):2314.
63. Momose A. Phase-sensitive imaging and phase tomography using X-ray interferometers. Optics Express. 2003 Sep 22;11(19):2303-14.

64. Momose A, Yashiro W, Takeda Y, Suzuki Y, Hattori T. Phase tomography by X-ray Talbot interferometry for biological imaging. Japanese journal of applied physics. 2006 Jun 8;45(6R):5254.

65. Weitkamp T, Diaz A, David C, Pfeiffer F, Stampanoni M, Cloetens P, Ziegler E. X-ray phase imaging with a grating interferometer. Optics express. 2005 Aug 8;13(16):6296-304.

66. Wu X, Liu H. A general theoretical formalism for X-ray phase contrast imaging. Journal of X-ray Science and Technology. 2003 Jan 1;11(1):33-42.

67. Wu X, Liu H. Clinical implementation of x-ray phase-contrast imaging: Theoretical foundations and design considerations. Medical physics. 2003 Aug 1;30(8):2169-79.

68. Wu X, Liu H. A new theory of phase-contrast x-ray imaging based on Wigner distributions. Medical physics. 2004 Sep 1;31(9):2378-84.

69. Wu X, Liu H. Phase-space formulation for phase-contrast x-ray imaging. Applied optics. 2005 Oct 1;44(28):5847-54.

70. Volkov VV, Zhu Y, De Graef M. A new symmetrized solution for phase retrieval using the transport of intensity equation. Micron. 2002 Dec 31;33(5):411-6

71. Burvall A, Lundström U, Takman PA, Larsson DH, Hertz HM. Phase retrieval in X-ray phase-contrast imaging suitable for tomography. Optics express. 2011 May 23;19(11):10359-76.

72. Guigay JP, Langer M, Boistel R, Cloetens P. Mixed transfer function and transport of intensity approach for phase retrieval in the Fresnel region. Optics letters. 2007 Jun 15;32(12):1617-9.

73. Wu X, Liu H, Yan A. X-ray phase-attenuation duality and phase retrieval. Optics letters. 2005 Feb 15;30(4):379-81.

74. Wu X, Liu H, Yan A. Robustness of a phase-retrieval approach based on phase-attenuation duality. Journal of X-Ray Science and Technology. 2007 Jan 1;15(2):85-95.

75. Langer M, Cloetens P, Peyrin F. Regularization of phase retrieval with phase-attenuation duality prior for 3-D holotomography. IEEE Transactions on Image Processing. 2010 Sep;19(9):2428-36.

76. Wu X, Liu H. X-Ray cone-beam phase tomography formulas based on phase-attenuation duality. Optics express. 2005 Aug 8;13(16):6000-14.

77. Wu X, Yan A. Phase retrieval from one single phase contrast x-ray image. Optics express. 2009 Jun 22;17(13):11187-96.

78. Wu X, Liu H, Yan A. Phase-contrast X-ray tomography: Contrast mechanism and roles of phase retrieval. European journal of radiology. 2008 Dec 31;68(3):S8-12

79. Yan A, Wu X, Liu H. A robust general phase retrieval method for medical applications. Journal of Instrumentation. 2013 May 24;8(05):C05007.

80. Wu X, Liu H. X-Ray cone-beam phase tomography formulas based on phase-attenuation duality. Optics express. 2005 Aug 8;13(16):6000-14.

81. Wu X, Liu H. X-Ray cone-beam phase tomography formulas based on phase-attenuation duality. Optics express. 2005 Aug 8;13(16):6000-14.

82. Burvall A, Lundström U, Takman PA, Larsson DH, Hertz HM. Phase retrieval in X-ray phase-contrast imaging suitable for tomography. Optics express. 2011 May 23;19(11):10359-76.

83. Wu X, Yan A, Liu H. X-ray phase-shifts-based method of volumetric breast density measurement. Medical physics. 2012 Jul 1;39(7):4239-44.
84. Ghani MU, Yan A, Wong MD, Li Y, Ren L, Wu X, Liu H. Low dose high energy x-ray in-line phase sensitive imaging prototype: Investigation of optimal geometric conditions and design parameters. Journal of X-ray science and technology. 2015 Jan 1;23(6):667-82.
85. Wu X, Barnes GT, Tucker DM. Spectral dependence of glandular tissue dose in screen-film mammography. Radiology. 1991 Apr;179(1):143-8.
86. Wu X, Gingold EL, Barnes GT, Tucker DM. Normalized average glandular dose in molybdenum target-rhodium filter and rhodium target-rhodium filter mammography. Radiology. 1994 Oct;193(1):83-9.
87. Sobol WT, Wu X. Parametrization of mammography normalized average glandular dose tables. Medical physics. 1997 Apr 1;24(4):547-54.
88. Boone JM. Normalized glandular dose (DgN) coefficients for arbitrary x-ray spectra in mammography: Computer-fit values of Monte Carlo derived data. Medical physics. 2002 May 1;29(5):869-75.
89. Boone JM, Nelson TR, Lindfors KK, Seibert JA. Dedicated breast CT: radiation dose and image quality evaluation. Radiology. 2001 Dec;221(3):657-67.
90. Luedemann W, Brinker T, Schuhmann MU, Von Brenndorf AI, Samii M. Direct magnification technique for cerebral angiography in the rat. Investigative radiology. 1998 Jul 1;33(7):421-4.

91. Ghani MU, Ren L, Wong M, Li Y, Zheng B, Rong XJ, Yang K, Liu H. Noise Power Characteristics of a Micro–Computed Tomography System. Journal of computer assisted tomography. 2017 Jan 1;41(1):82-9.
92. Wan SY, Kiraly AP, Ritman EL, Higgins WE. Extraction of the hepatic vasculature in rats using 3-D micro-CT images. IEEE Transactions on medical imaging. 2000 Sep;19(9):964-71.
93. Goldfeder S, Davis D, Cullinan J. Breast specimen radiography: can it predict margin status of excised breast carcinoma? Academic radiology. 2006 Dec 31;13(12):1453-9.
94. Ghani MU, Zhou Z, Ren L, Wong M, Li Y, Zheng B, Yang K, Liu H. Investigation of spatial resolution characteristics of an in vivo microcomputed tomography system. Nuclear Instruments and Methods in Physics Research Section A: Accelerators, Spectrometers, Detectors and Associated Equipment. 2016 Jan 21;807:129-36.
95. Ouandji F, Potter E, Chen WR, Li Y, Tang D, Liu H. Characterization of a CCD-based digital x-ray imaging system for small-animal studies: properties of spatial resolution. Applied optics. 2002 May 1;41(13):2420-7.
96. Powles-Glover N, De Schaepdrijver L, French J, Stewart J. Comparison of Faxitron™ versus MicroCT imaging of the skeleton of the suckling rat. Reproductive Toxicology. 2014 Sep 30;48:44-50.
97. Ghani MU, Wong MD, Ren L, Wu D, Zheng B, Rong JX, Wu X, Liu H. Characterization of continuous and pulsed emission modes of a hybrid micro focus x-ray source for medical imaging applications. Nuclear Instruments and

Methods in Physics Research Section A: Accelerators, Spectrometers, Detectors and Associated Equipment. 2017 May 1; 853:70-7.

98. Harvey JA, Bovbjerg VE. Quantitative assessment of mammographic breast density: relationship with breast cancer risk. Radiology. 2004 Jan;230(1):29-41.
99. Boyd NF, Guo H, Martin LJ, Sun L, Stone J, Fishell E, Jong RA, Hislop G, Chiarelli A, Minkin S, Yaffe MJ. Mammographic density and the risk and detection of breast cancer. New England Journal of Medicine. 2007 Jan 18;356(3):227-36.
100. Boyd NF, Byng JW, Jong RA, Fishell EK, Little LE, Miller AB, Lockwood GA, Tritchler DL, Yaffe MJ. Quantitative classification of mammographic densities and breast cancer risk: results from the Canadian National Breast Screening Study. JNCI: Journal of the National Cancer Institute. 1995 May 3;87(9):670-5.
101. Martin LJ, Boyd NF. Mammographic density. Potential mechanisms of breast cancer risk associated with mammographic density: hypotheses based on epidemiological evidence. Breast Cancer Research. 2008 Jan 9;10(1):201.
102. McCormack VA, dos Santos Silva I. Breast density and parenchymal patterns as markers of breast cancer risk: a meta-analysis. Cancer Epidemiology and Prevention Biomarkers. 2006 Jun 1;15(6):1159-69.
103. Li T, Sun L, Miller N, Nicklee T, Woo J, Hulse-Smith L, Tsao MS, Khokha R, Martin L, Boyd N. The association of measured breast tissue characteristics with mammographic density and other risk factors for breast cancer. Cancer Epidemiology and Prevention Biomarkers. 2005 Feb 1;14(2):343-9.

104. D'orsi CJ, Bassett L, Berg WA, Feig SA, Jackson VP, Kopans DB. Breast imaging reporting and data system: ACR BI-RADS-mammography. American College of Radiology. 2003;4.

105. Rosenberg RD, Hunt WC, Williamson MR, Gilliland FD, Wiest PW, Kelsey CA, Key CR, Linver MN. Effects of age, breast density, ethnicity, and estrogen replacement therapy on screening mammographic sensitivity and cancer stage at diagnosis: review of 183,134 screening mammograms in Albuquerque, New Mexico. Radiology. 1998 Nov;209(2):511-8.

106. Kolb TM, Lichy J, Newhouse JH. Comparison of the performance of screening mammography, physical examination, and breast US and evaluation of factors that influence them: an analysis of 27,825 patient evaluations. Radiology. 2002 Oct;225(1):165-75.

107. Berg WA, Zhang Z, Lehrer D, Jong RA, Pisano ED, Barr RG, Böhm-Vélez M, Mahoney MC, Evans WP, Larsen LH, Morton MJ. Detection of breast cancer with addition of annual screening ultrasound or a single screening MRI to mammography in women with elevated breast cancer risk. Jama. 2012 Apr 4;307(13):1394-404.

108. Byrne C, Schairer C, Wolfe J, Parekh N, Salane M, Brinton LA, Hoover R, Haile R. Mammographic features and breast cancer risk: effects with time, age, and menopause status. JNCI: Journal of the National Cancer Institute. 1995 Nov 1;87(21):1622-9.

109. Kriege M, Brekelmans CT, Boetes C, Besnard PE, Zonderland HM, Obdeijn IM, Manoliu RA, Kok T, Peterse H, Tilanus-Linthorst MM, Muller SH. Efficacy of

MRI and mammography for breast-cancer screening in women with a familial or genetic predisposition. New England Journal of Medicine. 2004 Jul 29;351(5):427-37.

110. Lee CH, Dershaw DD, Kopans D, Evans P, Monsees B, Monticciolo D, Brenner RJ, Bassett L, Berg W, Feig S, Hendrick E. Breast cancer screening with imaging: recommendations from the Society of Breast Imaging and the ACR on the use of mammography, breast MRI, breast ultrasound, and other technologies for the detection of clinically occult breast cancer. Journal of the American college of radiology. 2010 Jan 31;7(1):18-27.

111. Brem RF, Tabár L, Duffy SW, Inciardi MF, Guingrich JA, Hashimoto BE, Lander MR, Lapidus RL, Peterson MK, Rapelyea JA, Roux S. Assessing improvement in detection of breast cancer with three-dimensional automated breast US in women with dense breast tissue: the SomoInsight Study. Radiology. 2014 Oct 17;274(3):663-73.

112. Kuhl CK, Schrading S, Leutner CC, Morakkabati-Spitz N, Wardelmann E, Fimmers R, Kuhn W, Schild HH. Mammography, breast ultrasound, and magnetic resonance imaging for surveillance of women at high familial risk for breast cancer. Journal of clinical oncology. 2005 Nov 20;23(33):8469-76.

113. Kelly KM, Dean J, Comulada WS, Lee SJ. Breast cancer detection using automated whole breast ultrasound and mammography in radiographically dense breasts. European radiology. 2010 Mar 1;20(3):734-42.

114. Gordon PB, Goldenberg SL. Malignant breast masses detected only by ultrasound. A retrospective review. Cancer. 1995 Aug 15;76(4):626-30.

115. Giuliano V, Giuliano C. Improved breast cancer detection in asymptomatic women using 3D-automated breast ultrasound in mammographically dense breasts. Clinical imaging. 2013 Jun 30;37(3):480-6.
116. Ghani MU, Wong MD, Wu D, Zheng B, Fajardo LL, Yan A, Fuh J, Wu X, Liu H. Detectability comparison between a high energy x-ray phase sensitive and mammography systems in imaging phantoms with varying glandular-adipose ratios. Physics in Medicine and Biology. 2017 Apr 5;62(9):3523.
117. Smith SW, Wagner RF, Sandrik JM, Lopez H. Low contrast detectability and contrast/detail analysis in medical ultrasound. IEEE Transactions on Sonics and Ultrasonics. 1983 May;30(3):164-73.
118. Liu H, Fajardo LL, Barrett JR, Baxter RA. Contrast-detail detectability analysis: comparison of a digital spot mammography system and an analog screen-film mammography system. Academic Radiology. 1997 Mar 1;4(3):197-203.
119. Goodsitt MM, Chan HP, Schmitz A, Zelakiewicz S, Telang S, Hadjiiski L, Watcharotone K, Helvie MA, Paramagul C, Neal C, Christodoulou E. Digital breast tomosynthesis: studies of the effects of acquisition geometry on contrast-to-noise ratio and observer preference of low-contrast objects in breast phantom images. Physics in medicine and biology. 2014 Sep 12;59(19):5883.
120. Rivetti S, Lanconelli N, Campanini R, Bertolini M, Borasi G, Nitrosi A, Danielli C, Angelini L, Maggi S. Comparison of different commercial FFDM units by means of physical characterization and contrast-detail analysis. Medical physics. 2006 Nov 1;33(11):4198-209.

121. Liu H, Karellas A, Moore SC, Harris LJ, D'Orsi CJ. Lesion detectability considerations for an optically-coupled CCD x-ray imaging system. IEEE transactions on nuclear science. 1994 Aug;41(4):1506-9.

122. Hendee WR. Breast MRI: fundamentals and technical aspects. Medical Physics. 2008 Mar 1;35(3):1163-4.

123. Ghani MU, Wu D, Li Y, Kang M, Chen WR, Wu X, Liu H. Quantitative analysis of contrast to noise ratio using a phase contrast X-ray imaging prototype. InSPIE BiOS 2013 Feb 22 (pp. 85820H-85820H). International Society for Optics and Photonics.

124. Boone JM, Seibert JA. A figure of merit comparison between bremsstrahlung and monoenergetic x-ray sources for angiography. Journal of X-ray Science and Technology. 1994 Dec 1;4(4):334-45.

125. Ghani MU, Wong MD, Wu D, Zheng B, Chen W, Fajardo LL, Wu X, Liu H. Detectability comparison of simulated objects within a dense breast phantom using high energy x-ray phase sensitive and conventional imaging systems. InSPIE BiOS 2017 Feb 20 (pp. 100650K-100650K). International Society for Optics and Photonics.

126. Teertstra HJ, Loo CE, van den Bosch MA, van Tinteren H, Rutgers EJ, Muller SH, Gilhuijs KG. Breast tomosynthesis in clinical practice: initial results. European radiology. 2010 Jan 1;20(1):16-24.

127. Gennaro G, Toledano A, Di Maggio C, Baldan E, Bezzon E, La Grassa M, Pescarini L, Polico I, Proietti A, Toffoli A, Muzzio PC. Digital breast

tomosynthesis versus digital mammography: a clinical performance study. European radiology. 2010 Jul 1;20(7):1545-53.

128. Rafferty EA, Park JM, Philpotts LE, Poplack SP, Sumkin JH, Halpern EF, Niklason LT. Assessing radiologist performance using combined digital mammography and breast tomosynthesis compared with digital mammography alone: results of a multicenter, multireader trial. Radiology. 2013 Jan;266(1):104-13.

129. Skaane P, Bandos AI, Gullien R, Eben EB, Ekseth U, Haakenaasen U, Izadi M, Jebsen IN, Jahr G, Krager M, Niklason LT. Comparison of digital mammography alone and digital mammography plus tomosynthesis in a population-based screening program. Radiology. 2013 Apr;267(1):47-56.

130. Houssami N, Skaane P. Overview of the evidence on digital breast tomosynthesis in breast cancer detection. The Breast. 2013 Apr 30;22(2):101-8.

131. Haas BM, Kalra V, Geisel J, Raghu M, Durand M, Philpotts LE. Comparison of tomosynthesis plus digital mammography and digital mammography alone for breast cancer screening. Radiology. 2013 Dec; 269(3):694-700.

132. Kopans DB. Digital breast tomosynthesis from concept to clinical care. American Journal of Roentgenology. 2014 Feb;202(2):299-308.

133. Sechopoulos I. A review of breast tomosynthesis. Part I. The image acquisition process. Medical physics. 2013 Jan 1;40(1).

134. Sechopoulos I. A review of breast tomosynthesis. Part II. Image reconstruction, processing and analysis, and advanced applications. Medical physics. 2013 Jan 1;40(1).

135. Park JM, Franken Jr EA, Garg M, Fajardo LL, Niklason LT. Breast tomosynthesis: Present considerations and future applications 1. Radiographics. 2007 Oct;27(suppl_1):S231-40.

136. Naday S, Bullard E, Gunn S, Brodrick J, O'Tuairisg E, McArthur A, Amin H, Williams M, Judy P, Konstantinidis A. Optimised breast tomosynthesis with a novel CMOS flat panel detector. Digital Mammography. 2010:428-35.

137. Patel T, Klanian K, Gong Z, Williams MB. Detective quantum efficiency of a CsI-CMOS x-ray detector for breast tomosynthesis operating in high dynamic range and high sensitivity modes. InInternational Workshop on Digital Mammography 2012 Jul 8 (pp. 80-87). Springer, Berlin, Heidelberg.

138. Feldkamp LA, Davis LC, Kress JW. Practical cone-beam algorithm. JOSA A. 1984 Jun 1;1(6):612-9.

139. Rougee A, Picard CL, Trousset YL, Ponchut C. Geometrical calibration for 3D x-ray imaging. InMedical Imaging 1993 1993 Jun 30 (pp. 161-169). International Society for Optics and Photonics.

140. Godfrey DJ, Yin FF, Oldham M, Yoo S, Willett C. Digital tomosynthesis with an on-board kilovoltage imaging device. International Journal of Radiation Oncology* Biology* Physics. 2006 May 1;65(1):8-15.

141. Chen Z, Calhoun VD, Chang S. Compensating the intensity fall-off effect in cone-beam tomography by an empirical weight formula. Applied optics. 2008 Nov 10;47(32):6033-9.

142. Zhang Y, Chan HP, Sahiner B, Wei J, Goodsitt MM, Hadjiiski LM, Ge J, Zhou C. A comparative study of limited-angle cone-beam reconstruction methods for breast tomosynthesis. Medical physics. 2006 Oct 1;33(10):3781-95.

143. Miao H, Wu X, Zhao H, Liu H. A phantom-based calibration method for digital x-ray tomosynthesis. Journal of X-ray science and technology. 2012 Jan 1;20(1):17-29.

144. Wu D, Miao H, Li Y, Wu X, Liu H. In-plane spatial resolution measurements of a phase-contrast tomosynthesis prototype. InSPIE BiOS 2012 Feb 9 (pp. 82240D-82240D). International Society for Optics and Photonics.

145. Ghani MU, Wu D, Wong MD, Ren L, Zheng B, Yang K, Wu X, Liu H. Quantitative comparison of spatial resolution in step-and-shoot and continuous motion digital breast tomosynthesis. InSociety of Photo-Optical Instrumentation Engineers (SPIE) Conference Series 2016 Mar (Vol. 9783).

146. Boone JM, Seibert JA. An accurate method for computer-generating tungsten anode x-ray spectra from 30 to 140 kV. Medical physics. 1997 Nov 1;24(11):1661-70.

147. Ghani MU, Wong MD, Omoumi FH, Zheng B, Fajardo LL, Yan A, Wu X, Liu H. Detectability comparison of simulated tumors in digital breast tomosynthesis using high-energy X-ray inline phase sensitive and commercial imaging systems. Physica Medica. 2018 Mar 31; 47:34-41.